Characterisation and Optimisation of Donor-Acceptor Conjugated Copolymers for Applications in Bulk Heterojunction Organic Solar Cells

Darren Craig Watters

The University Of Sheffield.

Department of Physic and Astronomy
University of Sheffield

Thesis submitted for the degree of
Doctor of Philosophy

June 2014

In loving memory of my brother

Neil Kieren Watters

Acknowledgements

The completion of this thesis would not have been possible without the support of many people. Firstly, I would like to thank my supervisor David Lidzey for providing me with this unique opportunity. Thank you for believing in me and providing me with all the support and guidance I needed throughout my research. I could not have asked for a better supervisor.

I also thank my family for all their support. A big thank you to my parents (Brian and Evelyne) for their continued encouragement to help me achieve my full potential and to my sister (Delphine) for allowing me to continue to be young at heart.

I have had the pleasure of working with some fantastic people throughout my PhD. I would like to say a big thank you to James Kingsley for providing me with my initial training, being a friend and giving me someone to compete against. Special thanks also to Andrew Pearson for all your help and guidance as well as being a great person. Thanks also to Jon Griffin for all the help with metal oxides, Tao Wang for ellipsometry measurements and David Coles for assistance with photoluminescence quantum yield measurements. I would also like to thank Ahmed Iraqi's group of chemists for synthesising materials for me to utilise. Specifically, thanks to Ahmed and Hunan Yi for tolerating my polymer design ideas and for their patience in explaining several chemical aspects.

I would also like to thank all the people who have made my time in Sheffield memorable. To everyone in EPMM past and present: Ash, Al, James, Tao, David Mohammad, David Coles, Francesca, Ben, Andrew Pearson, Andrew Brook, Lee, Kieran, Jon, Nikos, Adam, Ed, Khalid, Nick, Charlotte, Alex, Theo, Chris, Lin, Jose, Mary, Nicola, Abdullah and Rania. A special shout out to Ben and Tabby for the awesome BBQ nights, especially in the snow! Also big thanks to Adam for all of our chats, being supportive when I needed it and being a great guy. Thanks also to all my St Andrews friends, especially Graham Skalley for being a great friend.

Last, but by no means least, to my girlfriend Suzie for being a wonderful person. Your unconditional love and support has provided me with the strength to be the best I can. Thank you.

Abstract

This thesis describes the development of donor-acceptor conjugated copolymer fullerene blends for applications in bulk heterojunction organic solar cells. The characterisation of the optoelectronic properties of the blends as well as the optimisation of such materials into organic photovoltaic (OPV) devices is described. The use of a composite cathode structure (in which a thin layer of calcium is backed by an optically thick layer of aluminium) for OPV application is presented. It is shown that this cathode structure optimise the power conversion efficiencies of PCDTBT based OPVs. The optimisation of the cathode structure was confirmed using a reflectivity model that described the electromagnetic field within the OPV devices.

The solubility of a number of polymers was increased using octyloxy side-chain substituents with device optimisation studies indicating the necessity of a thermal annealing treatment to fully optimise device performance. Selenophene based conjugated polymers were also investigated that had red-shifted absorption characteristics compared to comparable thiophene based materials. Despite a reduction in the optical energy gap, it was found that these polymers exhibited a lower molar absorption coefficient and reduced hole mobility, features that ultimately lead to poorer device performance. One selenophene polymer however was shown to have similar power conversion efficiency compared with its thiophene equivalent. Fluorene based copolymers were also investigated and were shown to result in efficient OPV devices through an increase in the

device open-circuit voltage. Finally, a conjugated polymer containing a fluorene unit together with additional thiophene moieties and octyloxy substituents was characterised. OPV devices were prepared using a simple preparation method with power conversion efficiencies demonstrated exceeding 6%.

Publications

1. H. Yi, S. Al-Faifi, A. Iraqi, D.C. Watters, J. Kingsley, D.G. Lidzey, Carbazole and thienyl benzo[1,2,5]thiadiazole based polymers with improved open circuit voltages and processability for application in solar cells, *Journal of Material Chemistry*, **2011**, *21*, 13649

2. T. Wang, A.J. Pearson, A.D.F. Dunbar, P.A. Staniec, D.C. Watters, H. Yi, A.J. Ryan, R.A.L. Jones, A. Iraqi, D.G. Lidzey, Correlating structure with function in thermally annealed PCDTBT:$PC_{70}BM$ photovoltaic blends, *Advanced Functional Materials*, **2012**, *22*, 1399-1408

3. D.C. Watters, J. Kingsley, H. Yi, T. Wang, A. Iraqi, D. Lidzey, Optimising the efficiency of carbazole co-polymer solar-cells by control over the metal cathode electrode, *Organic Electronics*, **2012**, *13*, 1404-1408

4. T. Wang, A.J. Pearson, A.D.F. Dunbar, P.A. Staniec, D.C. Watters, D. Coles, H. Yi, A. Iraqi, D.G. Lidzey, R.A.L. Jones, Competition between substrate-mediated π-π stacking and surface-mediated Tg depression in ultrathin conjugated polymer films, *The European Physical Journal E*, **2012**, *35*, 129

5. T. Wang, N.W. Scarratt, H. Yi, A.D.F. Dunbar, A.J. Pearson, D.C. Watters, T.S. Glen, A.C. Brook, J. Kingsley, A.R. Buckley, M.W.A. Skoda, A.M. Donald, R.A.L. Jones, A. Iraqi, D.G. Lidzey, Fabricating high performance, donor-acceptor copolymer solar cells by spray-coating in air, *Advanced Energy Materials*, **2013**, *3*, 505-512

6. J. Griffin, D.C. Watters, H. Yi, A. Iraqi, D. Lidzey, A.R. Buckley, The influence of MoO_x anode stoichemometry on the performance of bulk heterojunction polymer solar cells, *Advanced Energy Materials*, **2013**, *3*, 903-908

7. A.A.B. Alghamdi, D.C. Watters, H. Yi, S. Al-Faifi, M.S. Almeataq, D. Coles, J. Kingsley, D.G. Lidzey, A. Iraqi, Selenophene *vs.* thiophene in benzothiadiazole-based low energy gap donor-acceptor polymers for photovoltaic applications, *Journal of Materials Chemistry A*, **2013**, *1*, 5165-5171

8. D.C. Watters, H. Yi, A.J. Pearson, J. Kingsley, A. Iraqi, D. Lidzey, Fluorene based copolymer with high hole mobility and device performance in bulk heterojunction organic solar cells, *Macromolecular Rapid Communications*, **2013**, *34*, 1157-1162

9. A.J. Pearson, T. Wang, A.D.F. Dunbar, H. Yi, D.C. Watters, D. Coles, P.A. Staniec, A. Iraqi, R.A.L. Jones, D.G. Lidzey, Morphology development in amorphous polymer:fullerene photovoltaic blend films during solution casting, *Advanced Energy Materials*, **2013**, doi: 10.1002/adfm.201301922

Conference Presentations

Society for Information Displays (SID) Organic Electronics UK. Imperial College London, UK, September 2011
Poster Presentation – Winner of "Best student poster award sponsored by Merck"

Materials Research Society (MRS) Spring Meeting. San Francisco , USA, April 2012
Poster Presentation

UK Semiconductors Summer Meeting. Sheffield, UK, July 2012
Oral Presentation – Accepted

European Optical Society (EOS). Aberdeen, UK, September 2012
Oral Presentation

Contents

Chapter 1

Introduction

The continued increase in the world population as well as the growth in power consumption has resulted in the annual world power consumption to rise to 16.5 TW in 2012 [1]. This is an increase of 2% over 2011 levels, with the total consumption expected to rise to ~ 24 TW by 2030 if this rate remains constant. Currently, power is primarily provided from fossil fuels as well as nuclear power. Power obtained via renewable sources (including wind, geothermal, solar, biomass and waste but excluding hydro-electricity) account for only ~ 1.9% of global consumption. This value will most likely increase over the next few years in a global attempt to reduce greenhouse emissions (for example carbon dioxide, methane and nitrous oxide), in accordance with the Kyoto protocol [2]. The combined power generated from nuclear energy and renewables (including hydro-electricity) has remained relatively constant at 13% over the last 17 years [3]. However, one report has stated that all new energy could be produced from renewable sources alone by 2030 while replacing pre-existing energy by 2050 [4]. This is an uplifting conclusion as it would permit current pollution levels to be significantly reduced.

Solar power is one such renewable source which has seen rapid expansion and has the potential to have a significant impact on lowering the demand for electricity produced by fossil fuels. After taking into account atmospheric absorption and reflectivity, the surface of the Earth receives a total of ~ 100 PW of power from the sun [5]; approximately 6,000 times that of current world consumption. However, solar energy is relatively diffuse with a substantial area of land required to generate the energy needed by

modern industrial societies. Solar power has advantages on a smaller scale through its ability to be placed on households and/or office spaces, thus reducing the need to transport electricity from power plants. Research is underway to create “building integrated photovoltaics” (BIPV) in which components of the building are replaced by solar cells, with particular interest in combining solar panels with window glass [6]. It is worth noting that although solar power has a large potential, it will take the combination of all forms of renewable to replace current fossil fuel technologies [4,7].

Silicon based photovoltaic devices are a solar energy harvesting technology that has undergone > 60 years of development, with 10% efficiency demonstrated in 1955 [7], increasing to current value of around 25% [8]. Crystalline silicon has a bandgap of 1.1 eV allowing efficient absorption of solar radiation as shown in Figure 1.1. The favourable absorption characteristic of silicon together with the ease of creating free charge carriers upon photoexcitation allows such high device performance to be achieved. However, crystalline silicon has an indirect bandgap leading to the requirement of large active layer thicknesses which, along with the cost of processing high grade silicon, increases the cost of the technology. Furthermore, although silicon absorption is efficient within the 400-800 nm spectral range, it is poor for longer wavelengths where much of the solar flux exists.

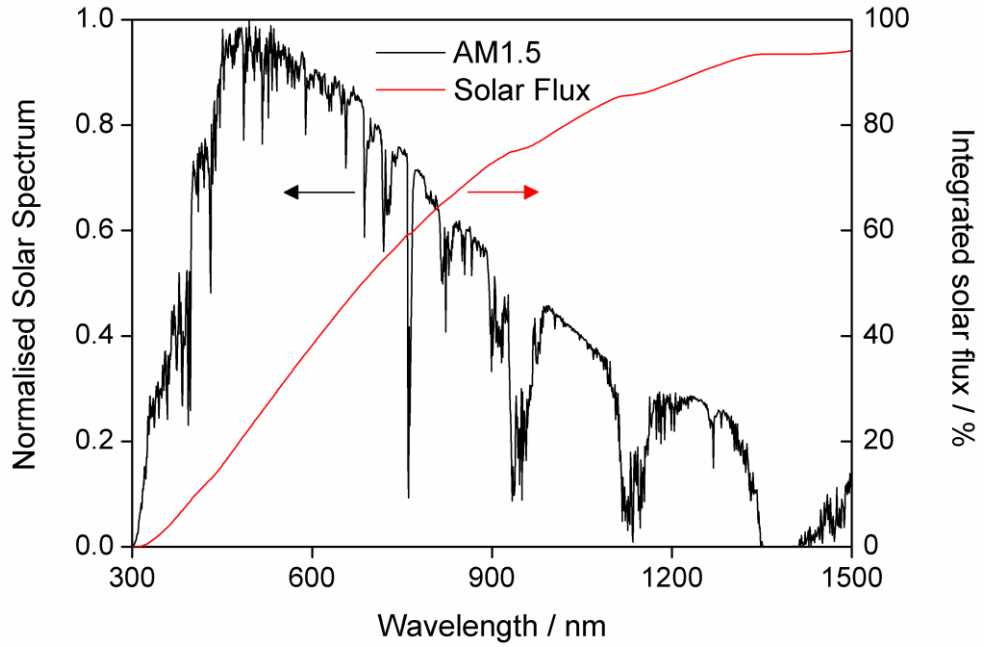

Figure 1.1 Normalised solar spectrum incident on the surface of Earth. The total solar flux is also plotted.

An alternative inorganic PV material is gallium arsenide (GaAs). This has been shown to be the most efficient material from which to construct a single junction solar cell, with a maximum efficiency of 28.8% recorded by Alta Device [8]. Despite advantages over silicon, including being a direct bandgap semiconductor with high absorptivity, such devices are expensive with impurities having a significant affect on performance. This consequently leads to this technology being used primarily for applications in space [9].

One thin film technology that addresses device cost is organic photovoltaics devices (OPVs). This technology has the potential to create cheap, flexible and lightweight devices. Here, costs can be reduced as the active semiconductor is primarily composed of carbon. Additionally, the active

layer can be cast from solution, allowing cheap, large area devices to be created. Devices containing such films have optimal efficiency when the active layer is very thin (~ 60 nm) due to the semiconductor possessing a high absorption coefficient. However, poor mobilities restrict the thickness of the active layers being increased above 100 nm. Furthermore, the generation of free charge carriers upon photoexcitation remains a critical issue for this technology due to the high binding energies between the charges. As such, device efficiency is currently limited to ~ 12% [10] and device stability remains an important issue that must be solved prior to commercialisation. Large scale production techniques have also not yet been fully realised although work is in progress [11]. The common usage of the metal oxide indium tin oxide ITO (a material often used in research labs as the device anode contact) is also problematic due to the limited supply of indium, with ITO being in heavy demand from its use in flat screen displays and mobile phones.

Another organic thin film technology under current research is dye-sensitized solar cells (DSSCs), which have demonstrated highly efficient devices with performances of 12% being realised [8]. Due to their architecture, DSSCs do not suffer greatly from recombination thus leading to efficient charge extraction. However, the use of hazardous materials is the major disadvantage of this system. Recently, solid state DSSC solar cells have been demonstrated with efficiencies of 15% realised [12]. Here, a perovskite film (i.e. a material with a similar structure as carbon titanium oxide $CaTiO_3$, in this case methylammonium lead iodide $CH_3NH_3PbI_3$) was

obtained by sequential deposition allowing a greater degree of control over the resultant film morphology.

Alternative inorganic thin film technologies are also being explored. These include amorphous-silicon (a-Si), copper indium gallium selenide (CIGS), cadmium telluride (CdTe, which has also been demonstrated via electrodeposition [13]), and copper zinc tin sulphide (CZTS). All of these systems possess a direct bandgap which allows the device to use less material, although active layer thicknesses remain greater than those used in organic semiconductor based devices. Other concerns for these technologies include the availability of precious metals (like tellurium) and the toxicity of materials like cadmium. The current maximum efficiency for such devices is 20.4% from a CIGS solar cell, 19.6% from CdTe and 8.5% from CZTS [14].

It is also worth noting that solar energy may be alternatively harvested via thermal processes. There are many technologies using this process such as those which are utilised for heating air/water in a residential or commercial environment. There are also larger systems which allow high temperature collection to enable efficient operation of steam or gas turbines for the generation of electricity. Many examples of such installations worldwide incorporating a variety of designs exist, for example parabolic troughs, towers or Fresnel reflectors. Note that these latter technologies are competitive with photovoltaic systems and have the ability to store thermal energy over many hours.

1.1 – Thesis summary and motivation

The aim of this thesis is to explore the characterisation and optimisation of conjugated donor polymers for applications in organic photovoltaic devices. Modifications to the chemical structure of the polymers include the addition of sidegroups to enhance polymer solubility, the replacement of particular heteroatoms with heavy atoms to red-shift the absorption, and the inclusion of additional spacer moieties to improve charge carrier mobility. The structure of this thesis is as follows.

Chapter 2 provides a background theory discussing the physics of organic semiconductors and their application in organic photovoltaic devices. A summary of all polymers presented throughout the remainder of the thesis is also provided. The experimental techniques utilised, including the solution and device preparation, are described in Chapter 3.

Chapter 4 discusses the optimisation of device structure of organic photovoltaic devices utilising the polycarbazole copolymer PCDTBT. Optimised device performance was achieved by varying the anode buffer layer (hole extraction layer) and the metal cathode. An optical model was used to probe the electromagnetic field within devices for the various metal cathodes, with results of the model compared with measurements made on OPV devices.

Chapter 5 addresses the development of donor-acceptor polymers with improved solubility without sacrificing device efficiency. The introduction

of solubilising sidegroups on PCDTBT resulted in the polymer:fullerene film requiring the use of a thermal annealing step to achieve high device performances. Comparing the polymer packing of PCDTBT and its substituted analogue demonstrated an increase in chain separation upon addition of the sidegroups. Charge carrier mobilities were also explored and it was found that substituted polymers were capable of mobilities up to 2.7 x 10^{-3} $cm^2V^{-1}s^{-1}$; a result likely to be due to a greater degree of backbone rigidity upon inclusion of the additional spacer moieties.

Chapter 6 looks at an optimisation study of polymers incorporating either sulphur or the heavy atom selenium. Utilising selenium heteroatoms resulted in a red-shift in the polymer absorption. Device performance was however generally lower for Se-based polymers due to a combination of low molar absorptivity and reduced hole mobility leading to lower device photocurrent. However, one Se-polymer demonstrated promising efficiency compared to its sulphur containing analogue.

Chapter 7 presents a new high performing polymer PFDT2BT-8. Device optimisation resulted in the development of a simple casting procedure with a maximum device efficiency exceeding 6% demonstrated. Good polymer solubility and a high charge carrier mobility are identified as being important in achieving such good device performance.

References

1. BP Statistical Review of World Energy. June 2013.
2. United Nations Framework Convention on Climate Change. http://unfccc.int/essential_background/kyoto_protocol/items/1678.php. Accessed: November 2013
3. J.M. Korhonen. (2013) *The stagnation of clean energy, with more detail.* http://jmkorhonen.files.wordpress.com/2013/07/130712_share_of_clean_energy_from_total_primary_energy_supply_1965-2012_from_bp_statistical_review.png. Accessed: November 2013
4. M.Z. Jacobson, M.A. Delucchi, Providing all global energy with wind, water, and solar power, Part I: Technologies, energy resources, quantities and areas of infrastructure, and materials, *Energ. Policy*, **2011**, *39*, 1154-1169
5. A. Cho, Energy's tricky tradeoffs, *Science*, **2010**, *329*, 786-787
6. Heliatek GmbH. Press release 2013. http://www.heliatek.com/wp-content/uploads/2013/09/Heliatek_AGC_FINAL_26_09_2013.pdf. Accessed: December 2013
7. M.A. Green, The path to 25% silicon solar cell efficiency: history of silicon cell evolution, *Prog. Photovolt: Res. Appl.*, **2009**, *17*, 183-189
8. P.K. Nayak, D. Cahen, Updated assessment of possibilities and limits for solar cells, *Adv. Mater.*, **2013**, doi: 10.1002/adma.201304620
9. R.W. Miles, G. Zoppi, I. Forbes, Inorganic photovoltaic cells, *Mater. Today*, **2007**, *10*, 20-27

10. Heliatek GmbH. Press release 2013. http://www.heliatek.com/wp-content/uploads/2013/01/130116_PR_Heliatek_achieves_record_cell_efficiency_for_OPV.pdf. Accessed: November 2013
11. D. Angmo, S.A. Gevorgyan, T.T. Larsen-Olsen, R.R. Søndergaard, M. Hösel, M. Jørgensen, R. Gupta, G.U. Kulkarni, F.C. Krebs, Scalability and stability of very thin, roll-to-roll processed, large area, indium-tin-oxide free polymer solar cell modules, *Org. Electron.*, **2013**, *14*, 984-994
12. J. Burschka, N. Pellet, S.-J. Moon, R. Humphry-Baker, P. Gao, M.K. Nazeeruddin, Michael Grätzel, Sequential deposition as a route to high-performance perovskite-sensitized solar cells, *Nature*, **2013**, *499*, 316-319
13. O.K. Echendu, F. Fauzi, A.R. Weerasinghe, I.M. Dharmadasa, High short-circuit current density CdTe solar cells using all-electrodeposited semiconductors, *Thin Solid Films*, **2014**, *556*, 529-534
14. M.A. Green, K. Emery, Y. Hishikawa, W. Warta, E.D. Dunlop, Solar cell efficiency tables (version 42), *Prog. Photovolt: Res. Appl.*, **2013**, *21*, 827-837

Chapter 2

Background theory

2.1 – Introduction

This chapter focuses on the various physical properties exhibited by organic semiconducting materials, and in particular conjugated polymers. Here, the discussion includes polymer structure, semiconducting properties and energy level manipulation. Section 2.4 then examines criteria for polymer solubility. Section 2.5 details the photophysical properties of these polymers before addressing the physics of organic photovoltaic (OPV) devices in Section 2.6. A brief review of the architecture of OPV devices is then provided with a discussion of the use of organic semiconductor materials in OPV devices presented in Section 2.8 and 2.9. Finally, a summary of all the conjugated polymers explored within this thesis is presented in Section 2.10.

2.2 – Hybridisation

Certain types of polymers (organic materials in which a monomer is covalently bound into a linear macromolecule) have been observed to exhibit semiconducting properties [1]. An examination into the formation of molecular orbitals in carbon-based molecules provides an insight into this property.

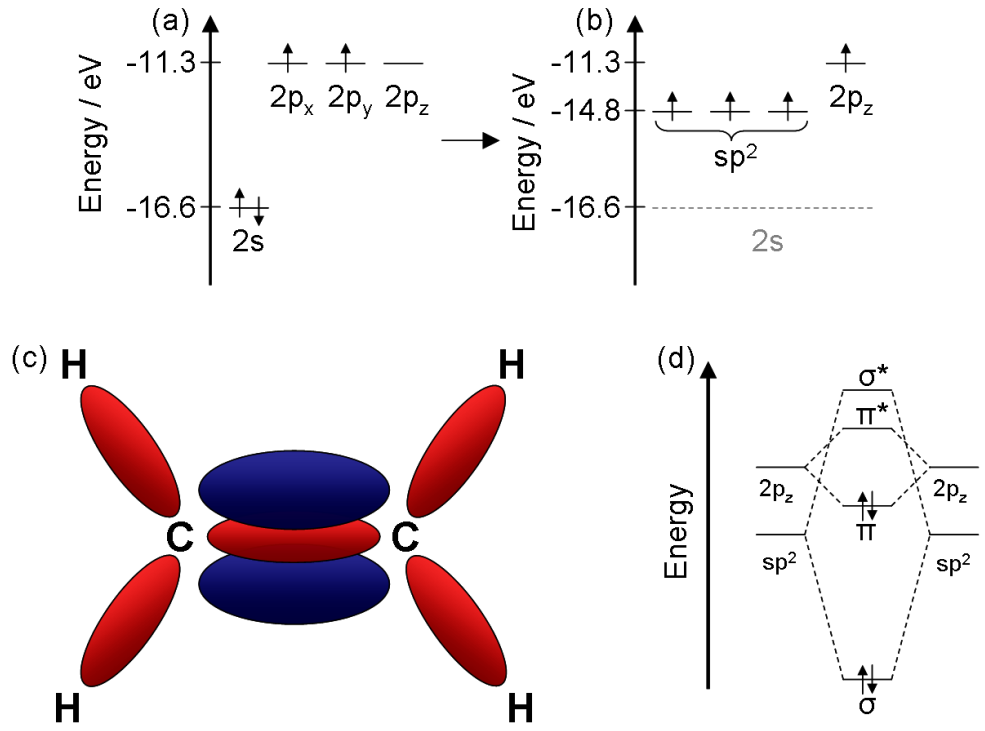

Figure 2.1 (a) Energy level and population of ground state carbon and (b) after sp^2 hybridisation. Note that at room temperature kT ≈ 0.026 eV; a value much lower than the energy required for bond dissociation. (c) Chemical structure of an ethene molecule where the σ-orbitals are represented by red and π-orbitals are blue. (d) A simplified molecular orbital diagram for the ethene molecule.

Carbon has a ground state electronic structure of $1s^2 2s^2 2p_x^1 2p_y^1$ which results in 4 valence electrons. As carbon is in the 2nd period, the formation of 4 bonds is possible to complete the octet rule (i.e. the outer electron shell can have a maximum of eight electrons). Figure 2.1(a) displays the energy levels and population of the ground state electronic structure with the co-ordinate system for the 2p-orbitals chosen arbitrarily. For simplicity, the filled inner electron shell (i.e. $1s^2$) will be omitted from further discussions. In its current state, and due to the Pauli exclusion principle, only electrons in

the $2p_x$ and $2p_y$ orbitals are available for bonding since the 2s shell is full. The formation of 4 equivalent bonds thus requires a process called hybridisation. Here, one of the 2s electrons is promoted to an empty 2p-orbital (the $2p_z$ in this case). This results in an electronic structure of $2s^1 2p_x^1 2p_y^1 2p_z^1$ which results in four unpaired electrons. Note that the energy required to create this excited state is accounted for during bond formation. Although three different kinds of hybridisation (sp, sp^2 and sp^3) are possible, it is the sp^2 hybridisation which is of principle importance in explaining the electronic structure of polymers with semiconducting properties.

In sp^2 hybridisation, the 2s-orbital and two of the 2p-orbitals undergo hybridisation to form three new orbitals, namely sp^2 hybrid orbitals, whereas the remaining 2p-orbital remains unhybridised. Figure 2.1(b) shows how the hybrid orbitals differ in energy from their ground state shown in part (a) while maintaining the conservation of energy. The sp^2 hybrid orbitals are responsible for the covalent bonds (σ-bonds) with other atoms while an overlap of the remaining 2p-orbitals can lead to the formation of π-bonds that exist parallel to the plane created by the σ-bonds. This leads to a trigonal arrangement for the σ-bonds, as shown in Figure 2.1(c) which highlights the chemical structure of an ethene molecule (consisting of 2 carbon atoms and 4 hydrogen atoms). In common parlance, σ-bonds are referred to as single bonds while the combination of a σ-bond and a π-bond is referred to as a double bond. It is worth noting that the σ-bond is more localised than the weaker π-bond, as will be explained later. Conjugated

polymers require the presence of alternating single and double bonds with the delocalisation of the π-electrons between neighbouring carbon molecules providing conjugated polymers with their semiconducting properties. Figure 2.2 displays the difference in chemical structure between (a) non-conjugated polyethylene and (b) conjugated polyacetylene.

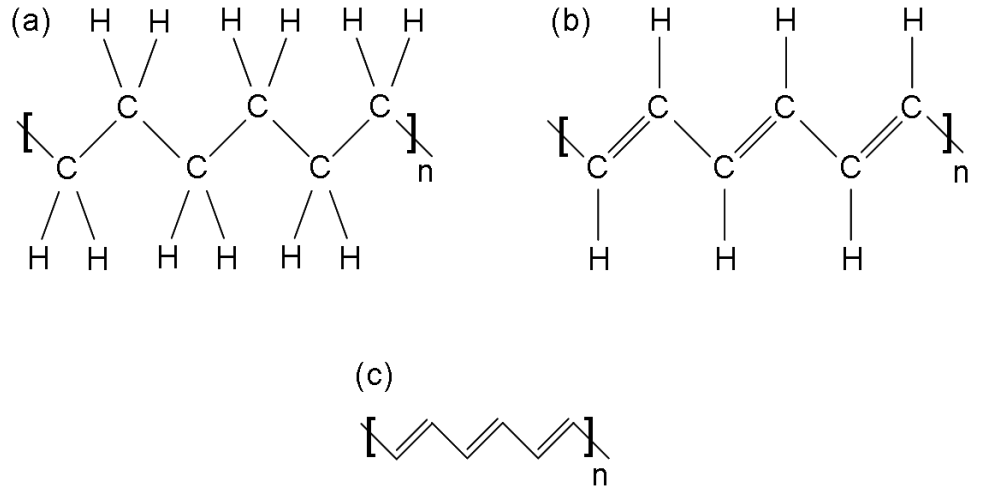

Figure 2.2 Graphical representations of (a) polyethylene and (b) polyacetylene. Short-hand notation of polyacetylene is displayed in (c) in which the carbon and hydrogen atoms are not plotted.

π-bonds are formed from unhybridised 2p-orbitals which, as shown in Figure 2.1(b), have a higher energy than the sp^2 hybrid orbitals. Figure 2.1(d) displays a simplified molecular orbital diagram for the bonds between the carbon atoms on an ethene molecule. It can be seen that the Highest Occupied Molecular Orbital (HOMO) corresponds to the π-bonding (or more specifically the π-electron cloud). The Lowest Unoccupied Molecular Orbital (LUMO) corresponds to the unoccupied π*-antibonding orbital. The difference in energy between these energy levels is defined as the materials

energy gap. The HOMO and LUMO levels can be thought as being similar to the valence and conduction bands respectively found in a conventional inorganic semiconductor. Bonding occurs when two orbitals are in phase, leading to the lowest possible resultant energy, whereas anti-bonding occurs from orbitals that are out-of-phase and consequently have a higher energy. These are summarised in Figure 2.3.

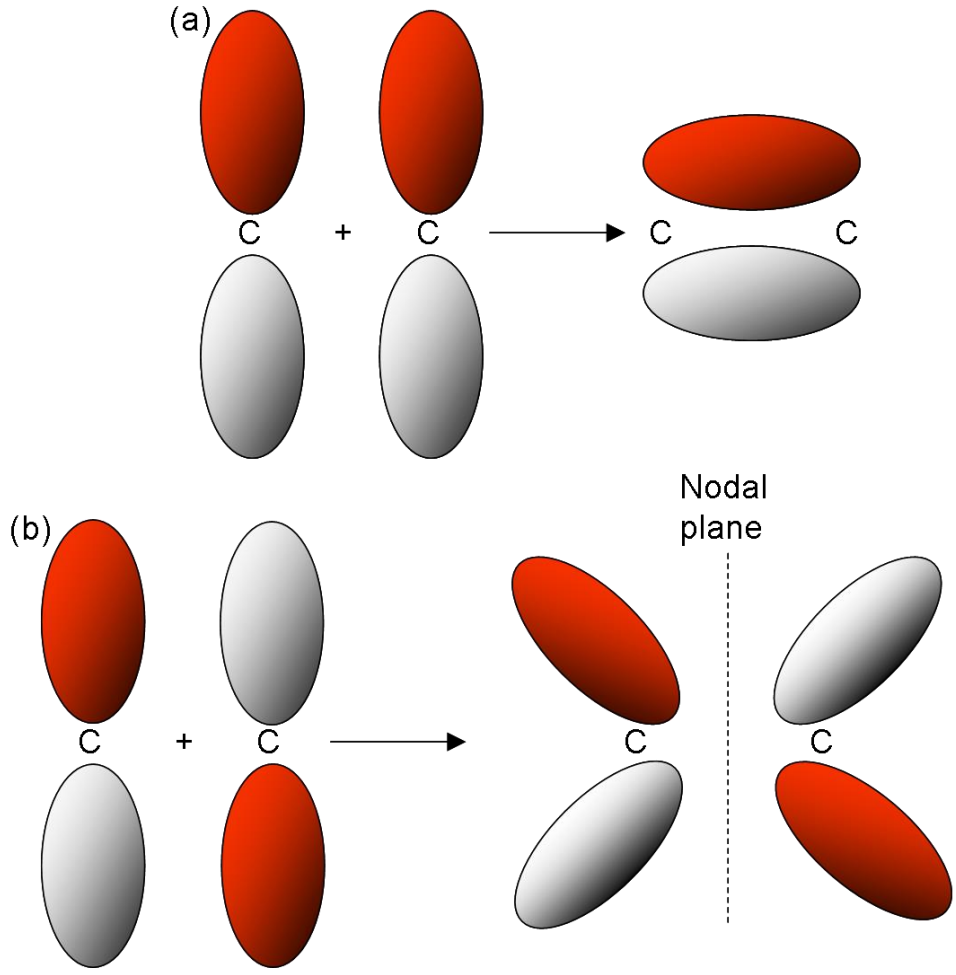

Figure 2.3 π-orbital overlap for (a) bonding and (b) anti-bonding orbitals. Note that the in-phase overlap (or bonding orbital) is of lower energy and corresponds to the HOMO energy level, whereas the anti-bonding orbital is associated with the LUMO energy level.

Promoting an electron from the HOMO level to the LUMO level changes the structure from bonding (π) to anti-bonding (π^*). If, hypothetically, in the case of polyacetylene (Figure 2.2(b)) each carbon atom were equidistant from one another then the π-electrons would be delocalised along the polymer chain. The π and π^* states would therefore be equivalent (with no way of distinguishing between the two states), consequently leading to the absence of an energy gap. This infinite chain would thus result in the polymer being metallic. However, this is not the case due to Peierls instability; here it was shown that a one-dimensional metal is unstable to lattice distortions [2]. Polyacetylene undergoes a lattice distortion which is referred to as bond length alternation (BLA). Here, the single and double bonds are not equidistant but instead exhibit different distances between neighbouring atoms, as shown in Figure 2.4. Indeed it was shown experimentally that the distances for single and double bonds in polyacetylene were 1.36 and 1.44Å respectively [3]. This bond length alternation results in an energy gap with the bonding state being energetically more stable. The electron density is also affected and is no longer extended over the entire polymer chain, but is instead delocalised over a few repeat units. As a consequence, polyacetylene is a semiconductor (rather than a metal) with an energy gap of 1.4 eV [4].

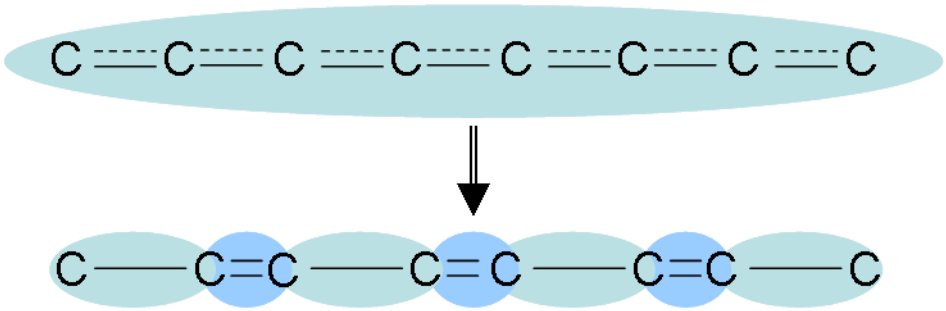

Figure 2.4 Peierls instability for a conjugated chain of carbon atoms. Note that the π-electron cloud is depicted by ellipses, with the double bonds leading to a higher density.

A popular aromatic hydrocarbon is the benzene ring, which frequently appears within conjugated polymers such as those presented throughout this thesis. Note that the most favourable arrangement for sp^2 hybrid orbitals is a trigonal arrangement with bond angles of 120˚. This therefore allows σ-bonding six sp^2 carbon atoms in a regular hexagonal configuration. Here, the resultant benzene ring, shown in Figure 2.5, leads to a complete delocalisation of the π-electron throughout its structure. This is an important property for conjugated polymers as discussed above.

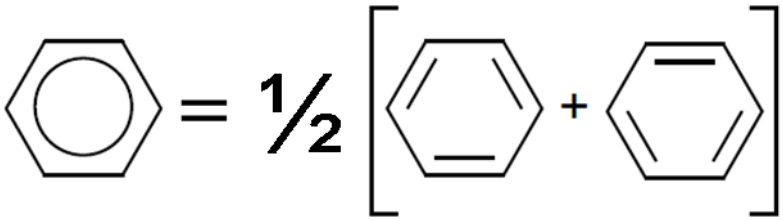

Figure 2.5 Chemical structure of the benzene ring. The delocalised π-electron is represented by a ring within the structure, a superposition of the two single-double bond structures displayed on the right hand side.

2.3 – Energy gap engineering

Conjugation (via bond length alternation) can have a significant affect on the energy gap of a material. Indeed, the difference between the energy gaps of the saturated polyethylene and the conjugated polyacetylene (structures shown in Figure 2.2(a) and (b) respectively) reveals that the latter has a much lower energy gap [5]. Increasing the electronic delocalisation also affects the energy gap. Although electronic delocalisation is restricted to several repeat units, other factors can also affect conjugation thereby influencing the energy gap; the remainder of this section details various other approaches in which polymer design can be used to tune this property and thereby create OPV materials suitable to harvest an increased spectral range.

Polymers in their ground π-bonding state are referred to as "aromatic" whereas their excited π* anti-bonding state is "quinoidal". It is possible to modify the energy gap by designing components where the quinoidal structure is more energetically favourable, for example polyisothianaphthene PITN [6], the poly(thienothiophene benzodithiophene) PTB family [7-9], or the similarly structured PBDTTT family [10-12]. This leads to a lowering of the energy gap by reducing the bond length alternation. A detrimental effect is however seen from this manipulation through the reduction in the HOMO energy level (which consequently affects the performance of an OPV device via a reduction in open circuit voltage V_{oc}). An alternative approach is to introduce either electron-donating or electron-withdrawing substituents along a polymer

backbone, for example replacing hydrogen atom(s) with fluorine [13-16]. Polymers with a donor-acceptor architecture (in which the "donor" component is electron-rich and the "acceptor" is electron-poor) can be used to fine-tune the HOMO and LUMO energy levels through the choice of each component [17-18]. This therefore allows an optimisation of the energy gap without any reduction in device efficiency. Similarly, replacing a heteroatom (a non-carbon atom within a conjugated ring) with another atom can affect a structure's electron-richness (or electron-deficiency), aromaticity (the tendency for a unit to localise an electron) or quinoidal structure resulting in modified energy levels [19-24], see Chapter 6 for additional details. Side chains (such as those discussed in further detail in Chapter 5) may also have an influence depending on their selection as well as their positioning [25-26].

2.4 – Polymer solubility

An attractive feature for conjugated polymer photovoltaic devices is the ease in which the active layer may be created. For example, the polymer may be dissolved in a solvent and then spin or spray coated onto a substrate. Polymer solubility is therefore a key parameter for device fabrication as well as understanding consequences from the polymer alterations described in the previous section. A polymer dissolves in a solvent if the interactions between polymer and solvent molecules satisfy the following requirements.

The Gibbs free energy upon mixing the two components is:

$$\Delta G_m = \Delta H_m - T\Delta S_m \qquad \{2.1\}$$

where ΔH_m (ΔS_m) is the enthalpy (entropy) change upon mixing and T is the absolute temperature. The enthalpy and entropy of the mixing may be broken down to expressions involving the interactions between polymer and solvent molecules. This leads to:

$$\Delta H_m = kT\chi N_1\varphi_2 \qquad \& \qquad \Delta S_m = -k(N_1 \ln \varphi_1 + N_2 \ln \varphi_2) \qquad \{2.2\}$$

where k is the Boltzmann's constant, χ is the interaction parameter, N_1 (N_2) is the number of solvent (polymer) molecules and φ are the lattice volume fractions. Note that the polymer is divided into x segments such that each segment has a comparable size as the solvent molecule. This results in the lattice volume fractions being defined as $\varphi_1 = N_1/N$ and $\varphi_2 = xN_2/N$, with N being the total number of molecules. Inputting the expressions from equation 2.2 into 2.1 results in:

$$\Delta G_m = kT(\chi N_1\varphi_2 + N_1 \ln \varphi_1 + N_2 \ln \varphi_2) \qquad \{2.3\}$$

In order for the polymer to dissolve in the solvent, ΔG_m must be negative which requires $\chi N_1\varphi_2 < N_1\ln\varphi_1 + N_2\ln\varphi_2$ (since $\ln\varphi < 0$). The interaction parameter χ is inversely dependent on temperature. Therefore, increasing T allows a reduction in χ and thus an increased polymer solubility. Polymer

solubility may also be improved by the inclusion of soluble sidegroups. These groups cause an increase in the solution entropy therefore allowing greater solubility. This technique is explored in Chapters 5 and 6.

2.5 – Photophysics of conjugated polymers

One of the key properties of many conjugated polymers is their ability to efficiently absorb photons in the visible region of the solar spectrum. Energy gap engineering therefore becomes a critical part in conjugated polymer design for OPV applications as such energy gaps define the polymer's possible absorption wavelength range; see Figure 2.6 for an example of polymers with differing energy gaps.

Figure 2.6 An optical image of 11 different polymers having differing absorption characteristics. Chemical name and structure of each polymer is provided in the Appendix.

Figure 2.7 displays an energy level diagram based on the Frank-Condon principle. Here, the S_0 and S_1 singlet states are the ground and excited states respectively. Each state also contains a variety of quantised vibrational levels (n) forming a ladder of states. Such energy levels can thus be labelled as $S_{0,n}$.

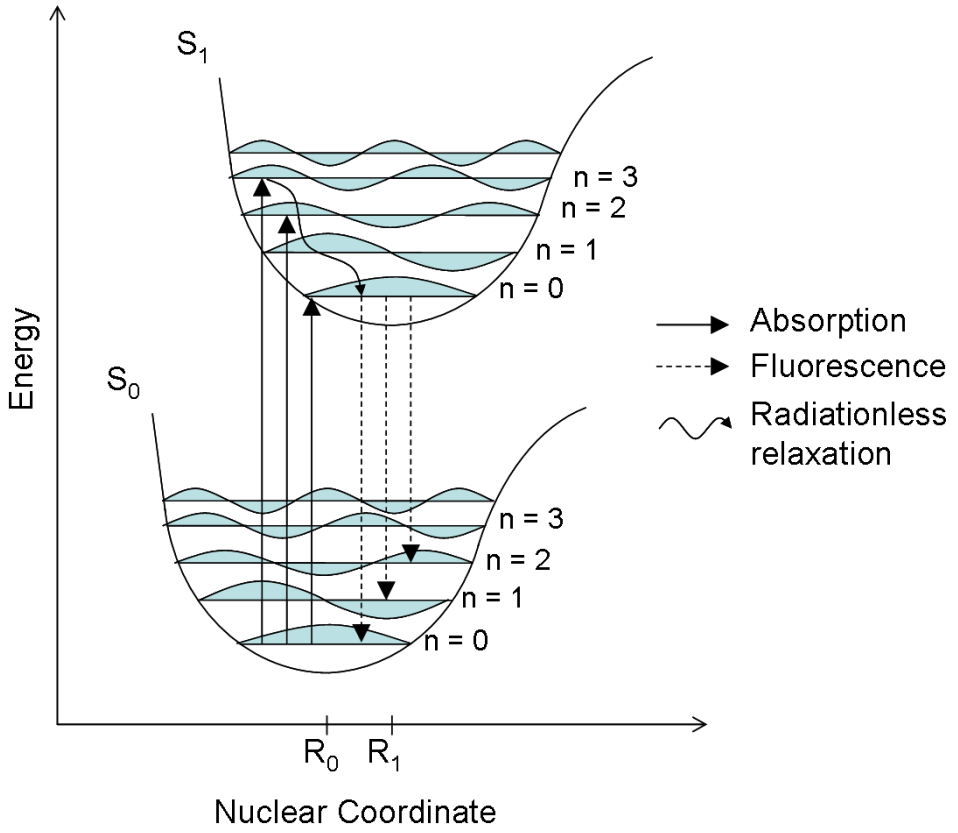

Figure 2.7 Energy level diagram of the ground state S_0 and the first excited state S_1 including vibrational states and electronic transitions.

A ground state electronic transition occurs when a photon with energy greater than, or equal to, the energy gap is absorbed by an electron in the S_0 state. This transition occurs in a shorter time than nuclear motions (i.e. before spatial alterations of the nuclei) and is therefore depicted by a

straight line (Frank-Condon transition) in the energy level diagram. If the photon possesses an energy slightly greater than the energy gap, the electron is initially promoted to a higher vibrational mode which then undergoes fast radiationless relaxation to its equilibrium configuration (i.e. n = 0), over timescales of ~ 0.1 ps [27]. An excitation from $S_{0,0}$ to $S_{1,n}$, (or HOMO → LUMO) will also cause the bonding structure along the backbone to reorder from aromatic to quinoidal.

Upon photoexcitation, an electron is located in an excited state leaving behind a hole in the ground state. This electron-hole pair is referred to as an exciton which has a neutral charge and is bound coulombically. Figure 2.8 displays the different bond structure of the polymer p-(phenylene vinylene) upon photoexcitation. Exciton recombination may occur over timescales between 100 ps and 1 ns [28]. This is however longer than the timescale for radiationless relaxation of excited electrons to the n = 0 vibronic energy level, and thus fluorescence emission to the S_0 ground state occurs once the equilibrium configuration of the excited state has been reached. At this point, a photon of equal or lower energy than that for absorption can be emitted (as can be seen from the energy difference from $S_{1,0} \rightarrow S_{0,n}$ in Figure 2.7).

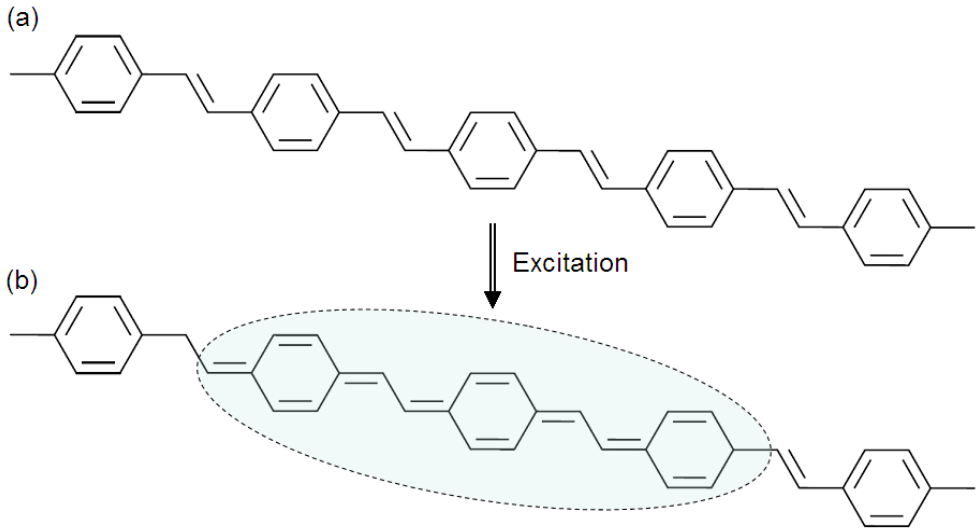

Figure 2.8 Chemical structure of p-(phenylene vinylene) in (a) its ground state and (b) after photoexcitation. The delocalisation of the exciton in part (b) is depicted by the ellipse. Note that bond length alternation has not been included in either part.

A key difference between the excitons created in organic materials compared to those in an inorganic semiconductor is the exciton binding energy of the electron-hole pair. Organic materials possess a relatively low dielectric constant, ε_r, with typical values of 3-4 [29-30]. This therefore results in a high Coulombic attraction between the electron-hole pair, with such excitons referred to as Frenkel excitons. Conversely, inorganic semiconductors have higher dielectric constants, smaller exciton binding energies ($<< k_BT$) and are less localised thus enabling the generation of free charge carriers at room temperature. Further details are provided in Section 2.6 regarding the processes for OPV materials.

An alternative method of recombination to the singlet ground state $S_{0,0}$ is phosphorescence in which an electron relaxes from an excited triplet state (T_1), rather than from the excited single state $S_{1,0}$. The T_1 state can be populated from intersystem crossing from the S_1 manifold.

We can describe an exciton through the description of its wavefunction. These wavefunctions can be separated into two components of angular momentum; orbital and intrinsic (i.e. spin). The Pauli exclusion principle states that the overall wavefunction must be antisymmetric. This results in no two electrons with the same spin occupying the same orbital, therefore limiting the number of electrons that can populate any given energy level. Electrons have a spin value of s = ½, and thus electron-electron or electron-hole coupling is permitted provided the total spin, S, of the system is S = 0 (antisymmetric, singlet) or S = 1 (symmetric, triplet).

The excited singlet state has an overall spin S = 0 and can be expressed by the following spin wavefunction:

$$\psi_{S_1} = \frac{1}{\sqrt{2}}\left(|\uparrow\downarrow\rangle - |\downarrow\uparrow\rangle\right) \qquad \{2.4\}$$

Here, the two electrons occupy the same orbital (the S_1). The Pauli exclusion principle is therefore satisfied (i.e. the total wavefunction is antisymmetric upon particle exchange) as the spin is antisymmetric. There

are three combinations in which the spin part of the wavefunction may be symmetric (i.e. a total spin S = 1):

$$\psi_{T_1} = \frac{1}{\sqrt{2}}\left(|\uparrow\downarrow\rangle + |\downarrow\uparrow\rangle\right), \quad \psi_{T_1} = |\uparrow\uparrow\rangle, \quad \psi_{T_1} = |\downarrow\downarrow\rangle \qquad \{2.5\}$$

These are the triplet states which have a symmetric spin and an antisymmetric orbital wavefunction. As electrons experience a reduced repulsion from one another as they occupy different orbitals, electrons in a triplet wavefunction have a lower energy than those in the excited singlet energy level.

The singlet ground state S_0 is described by:

$$\psi_{S_0} = |\uparrow\downarrow\rangle \qquad \{2.6\}$$

It is important to note that for an optical transition to be allowed, the change in the intrinsic angular momentum quantum number (S) must equal 0, i.e. $\Delta S = 0$, however the change in the orbital angular momentum quantum number (L) must not be zero, e.g. $\Delta L = 1$. This, for example, is satisfied by the absorption transition from $S_0 \rightarrow S_1$ as these states have an orbital angular momentum of L = 0 and 1 respectively. Here, the angular momentum possessed by the absorbed photon provides this change. Both states also have a total spin of S = 0 which satisfies the $\Delta S = 0$ selection rule. Similarly, the inverse transition (fluorescence) is possible, again due to

the fulfilment of the selection rules. It can be seen however that this is not the case for the $S_0 \rightarrow T_1$ transition as $\Delta S \neq 0$, making the transition dipole forbidden. It is however possible for triplet transitions to occur due to spin-orbit coupling; an interaction between the particle's spin and its orbital angular momentum. $S_0 \rightarrow T_1$ transitions are therefore possible providing the spin of the electron "flips". Populating the triplet state is most likely via intersystem crossing, i.e. $S_0 \rightarrow S_1 \rightarrow T_1$. Relaxation to the ground state from the triplet state by emission of a photon is called phosphorescence and has a longer lifetime than fluorescence as the $T_1 \rightarrow S_0$ transition requires spin-orbit coupling. There are therefore several processes in which an excited electron may relax to the ground state. Figure 2.9 summarises such processes using a Jablonski diagram.

Note that the spin-orbit coupling process is more likely for atoms with a high orbital quantum number. Here, heavy atoms increase the spin-orbit interactions thus leading to enhanced intersystem crossing transitions [27].

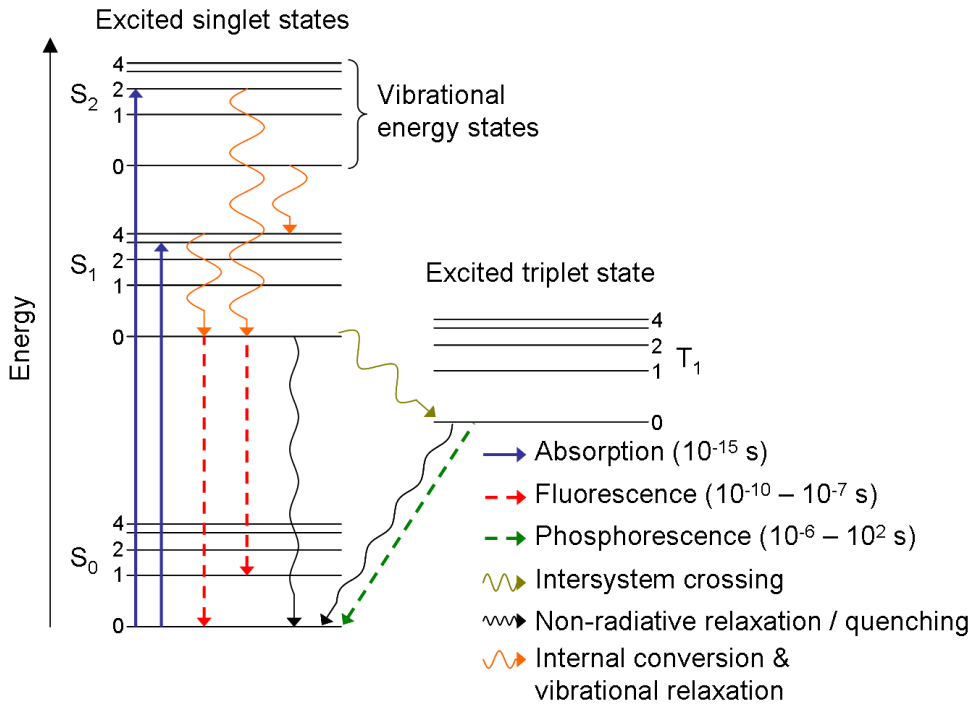

Figure 2.9 Possible electronic transitions as illustrated by a Jablonski energy diagram. Radiative and non-radiative transitions are indicated by straight and curved lines respectively.

2.6 – Device physics of organic photovoltaic devices

2.6.1 – Exciton diffusion

Upon photoexcitation an exciton is created which is strongly bound due to Coulombic attraction. To separate the electron and hole pair in a Frenkel exciton prior to recombination, the exciton must reach an interface with favourable energy to allow its dissociation into free charge carriers [31]. The exciton may diffuse (via a hopping process) either along a polymer chain (intrachain) or between chains (interchain). The efficiency of exciton diffusion is described by its diffusion coefficient, *D*. The distance an exciton can travel prior to recombination can be quantified by the exciton diffusion length (L_D) which is given by [32]:

$$L_D = \sqrt{D\tau} \qquad \{2.7\}$$

in which τ is the photoluminescence decay lifetime. If the average distance between donor-acceptor interfaces is smaller or comparable to the exciton diffusion length, then it is likely that it will be separated into free charge carriers.

Exciton diffusion results from two energy transfer mechanisms; namely Förster resonance energy transfer (FRET) and Dexter energy transfer, with both processes summarised in Figure 2.10(a) and (b) respectively. In the case of FRET, an excited donor molecule transfers energy to the ground state acceptor molecule via non-radiative dipole-dipole coupling [33]. This process is inversely dependent on the donor-acceptor separation distance (r^{-6}) and the overlap between the donor emission and the acceptor absorption spectra, as well as the relative orientation of their dipole moments. Dexter energy transfer, on the other hand, involves electrons being directly transferred from the donor to the acceptor [34]. This process is dependent on the donor-acceptor separation distance and the wavefunction overlap, i.e. the overlap of the electron cloud. This restricts the donor-acceptor separation to distances of < 2 nm, instead of ~ 3-6 nm for FRET [34]. From the previous discussion regarding spin-orbit coupling, it can be seen that triplet diffusion by FRET has a low probability. This is because the excited donor triplet state would require its spin to "flip" as well as the acceptors ground state transition to an excited state (shown in Figure 2.10(c)). In the Dexter energy transfer, however, the exchange of electrons

from donor to acceptor conserves the spin of the transferring excited triplet state and ground state, as shown in Figure 2.10(d). Therefore, Dexter energy transfer is capable of diffusing triplet states as well as singlet states.

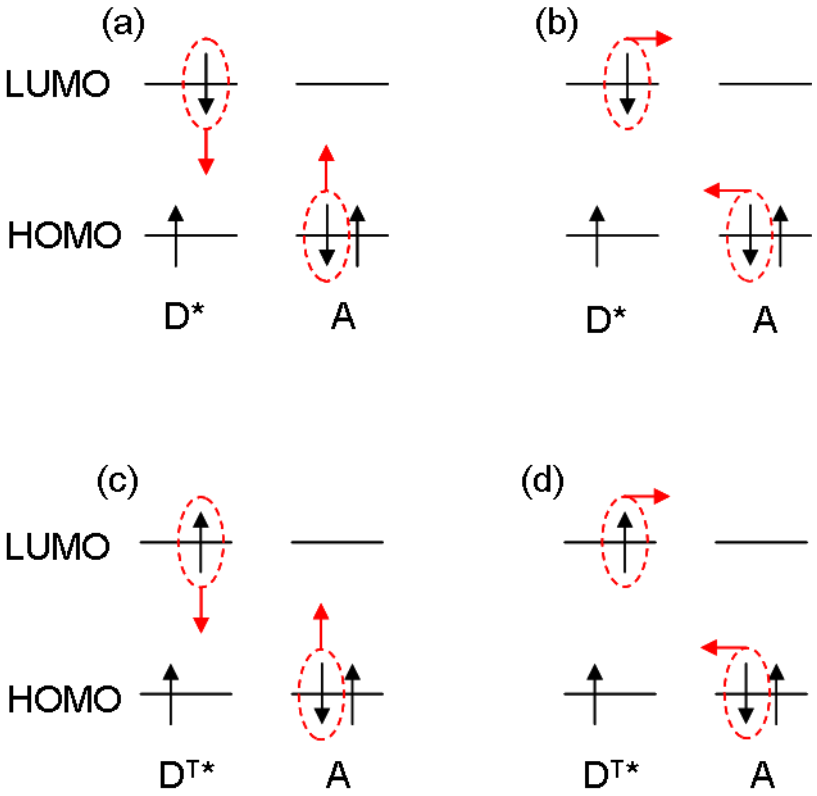

Figure 2.10 Schematic of the possible exciton diffusion processes: (a) Förster resonance energy transfer, FRET, and (b) Dexter energy transfer. (c) Triplet-triplet energy transfer for FRET (requires spin-orbit coupling) and for (d) Dexter energy transfer.

2.6.2 – Exciton dissociation

Dissociation is the process in which the components of the exciton (i.e. the electron and the hole) separate into free charge carriers. The process of dissociation occurs at a donor-acceptor interface providing it is energetically favourable [31]. This may be achieved if the LUMO energy level of the

acceptor is further away from the vacuum level that that of the donor [35]. This creates an energetic driving force and, provided the energy level difference is larger than the exciton binding energy [31], the exciton may dissociate into a geminate pair in which the electron and hole are still bound together but each exist in a different material. The geminate pair exists within a charge-transfer (CT) state. The energy of this state must be lower than the LUMO singlet levels otherwise energy transfer, rather than charge transfer, will occur [36].

Following this transfer process the electron-hole pair may undergo separation into free charge carriers if the internal electric field is sufficient to break the Coulomb attraction for the geminate exciton. The dissociation of charges in the CT state may also be expressed by the Onsager theory, to a first approximation [28]. Here, thermal energy possessed by the excited electron may be enough to overcome the attraction for the exciton. The dissociation and separation operations are displayed schematically in Figure 2.11.

One study characterised the CT state for a variety of donor polymers blended with an assortment of fullerene adducts [36]. They demonstrated that as the energy difference between the CT state and the lowest component absorption onset reduced below 0.35 eV, a decrease in the photogeneration rate was observed. This was due to the activation of singlet emission observed through electroluminescence, as well as the lack of photoluminescence quenching, consequently reducing the device

photocurrent. Therefore, the energy levels for choosing a polymer:fullerene system is critical to achieve efficient device performance. Indeed, if the energy level difference is not greater than the exciton binding energy (~ 300 meV) then electron transfer to the acceptor is not necessarily favourable. Conversely, an energy difference that is much larger than the binding energy does not exhibit any beneficial characteristics, as the resultant device efficiency is reduced through a decrease in the open circuit voltage V_{oc} [37], see Section 2.6.5.

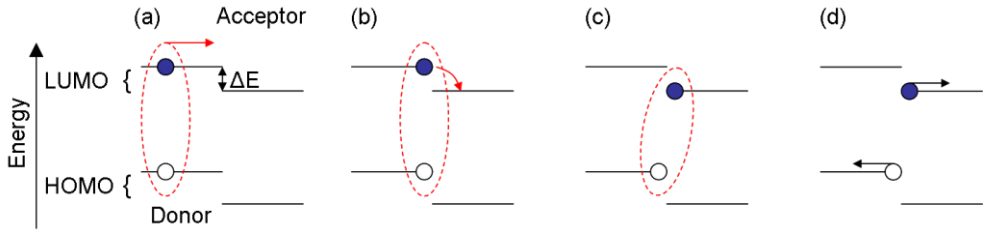

Figure 2.11 Schematic of exciton diffusion and its subsequent dissociation at a donor-acceptor interface to create a geminate pair (a-c). This process is followed by separation and transport of free charge carriers (d).

There are, however, several possible detrimental effects that may occur during the processes discussed above and are summarised in Figure 2.12. Recombination of the excited electron (a) can occur if the separation between the exciton and the interface is greater than the exciton diffusion length. Similarly, part (b) shows geminate recombination which may happen if the exciton is not separated into free charge carriers (this could be related to the disorder within the active layer and/or the internal field of the device). If energy transfer occurs instead of charge transfer, i.e. both electron and hole transfer to the acceptor, then recombination may occur within the

acceptor (c). A final detrimental effect is for a free electron and hole to recombine with each other (d); a process known as non-geminate recombination that can be caused by electronic traps within the material.

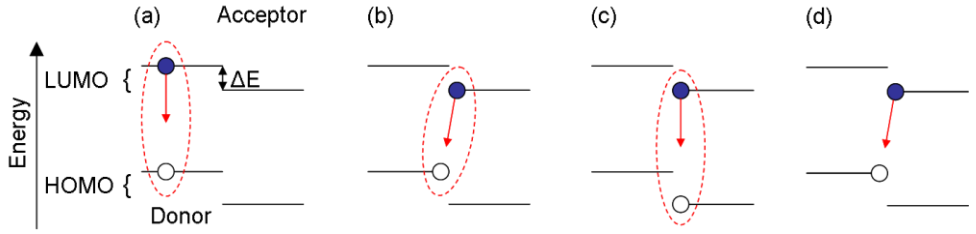

Figure 2.12 Various recombination processes in a donor-acceptor junction. (a) Excited state recombination, (b) geminate recombination, (c) recombination after energy transfer, and (d) non-geminate recombination.

2.6.3 – Charge transport

Following exciton dissociation, free charge carriers created need to be transported to an electrode for extraction. Charge transport in organic semiconductors is affected by the weak intermolecular coupling between molecules, as well as their spatial and energetic disorder. Consequently, charges are localised to a single molecule and transport occurs by phonon-assisted hopping (a process dependent on temperature and electric field). The activation energy for charge transport can be separated into two components: a disorder contribution and an intra/intermolecular contribution in which thermal activation is required for both. A Gaussian disorder model has been used to give a description of charge transport. The distribution of energetic states, $g(E)$, in a disordered system is given by [38]:

$$g(E) = \frac{1}{\sqrt{2\pi\sigma}} \exp\left(-\frac{E^2}{2\sigma^2} \right) \qquad \{2.8\}$$

where E is the energy of the site and σ is a disorder parameter (which determines the width of the transport distribution). The shape of the density of states can be inferred from the shape of the absorption spectra (caused from inhomogeneous broadening) in an amorphous organic material [38-39], since no direct experimental proof can be obtained.

The Miller-Abrahams equation gives the transition rate for phonon-assisted hopping, υ_{ij}, between molecular sites i and j as [40]:

$$\upsilon_{ij} = \upsilon_0 \exp(-2\gamma\Delta r_{ij}) \begin{cases} \exp\left(-\dfrac{E_j - E_i}{k_B T} \right) & E_i < E_j \\ 1 & E_i \geq E_j \end{cases} \qquad \{2.9\}$$

Here υ_0 is the attempt-to-jump frequency, γ is the inverse wavefunction localisation radius (or coupling matrix element between sites), Δr_{ij} is the distance between the sites, and E_i (E_j) is the energy of the occupied site i (unoccupied site j). In the condition where $E_i \geq E_j$, it is energetically favourable for charge transport to only occur by hopping from site i to j (neglecting thermal activation and the presence of an external electric field).

When an electric field is applied, charge transport is typically characterised by the charge carrier mobility, μ, which is dependent on temperature and the applied field. The applied electric field, F, will tilt the density of states

thereby lowering the energy for charge transport [41]. Through the use of Monte-Carlo simulations and with the assumption that the HOMO energy levels of the disordered system form a Gaussian distribution about an average, Bässler derived the following equation for $\mu(T,F)$ [38]:

$$\mu(T,F) = \mu_0 \exp\left[\left(-\frac{2}{3k_bT}\sigma\right)^2\right]\begin{cases}\exp\left[C\left(\sigma^2-\Sigma^2\right)\sqrt{F}\right], & \Sigma \geq 1.5\\ \exp\left[C\left(\sigma^2-2.25\right)\sqrt{F}\right], & \Sigma \leq 1.5\end{cases} \quad \{2.10\}$$

In equation 2.10, the mobility includes a diagonal disorder (which addresses the energetic distribution), σ, and an off-diagonal disorder (positional disorder), Σ. The μ_0 variable is the zero-field mobility (at infinite temperature) while C is a constant related to the intermolecular spacing.

Throughout Chapters 5-7, charge carrier mobility will be expressed through values determined from organic field effect transistors (OFET), although other measurements are possible, namely time-of-flight (TOF) and space charge limited current (SCLC). While SCLC measurements would also be applicable for the polymers presented in this thesis, TOF measurements (which require a thick semiconductor layer) would not be practical due to the low solubility of some of the polymers studied. It is worth noting that the carrier density and electric fields differ in each setup therefore influencing the resultant mobility. Although OFET devices are not ideal to determine bulk transport characteristics in OPV device (as the active layer is comprised of a blend of two materials), the measured mobilities can be compared to provide an upper approximation of the effectiveness of the hole

mobility for a variety of donor polymer systems. It is important to achieve similar hole and electron mobilities (~ 10^{-3} $cm^2V^{-1}s^{-1}$) in the active layer. This allows balanced charge transport in the device, which is limited by the material with the lower value, consequently improving device performance. Additional information regarding the OFET architecture and analysis is presented in Section 3.8.

2.6.4 – Charge extraction

Following the transport of free carriers to their respective electrodes, charge extraction may take place providing that the electrode materials have an appropriate work function. Note that in OPV device, the morphology and vertical stratification (the vertical distribution of materials between the electrodes) play a critical role in many of the processes presented above, and can also determine the efficiency of the extraction process. For example, if there is an abundance of the donor material positioned close to the cathode (electron extracting electrode), charge extraction may be reduced as a result of increased non-geminate recombination.

The device electrodes should therefore satisfy the following:

$$\begin{aligned} \Phi^{anode} &= HOMO^{donor} \\ \Phi^{cathode} &= LUMO^{acceptor} \end{aligned} \qquad \{2.11\}$$

where Φ is the work function. Electrodes which satisfy equation 2.11 are referred to as being in ohmic contact. A built-in potential, created by the

differing energy levels, is obtained which consequently dictates the direction in which free charge carriers travel; resulting in enhanced charge extraction by limiting geminate and non-geminate recombination.

In the metal-insulator-metal (MIM) picture, the open circuit voltage (V_{oc}) of the device is predicted to be related to the difference between the work function of the two electrodes. However, for a bulk heterojunction organic photovoltaic device, it has been observed that the energy levels of the donor and acceptor components in the active region play a significant role in the determination of the device V_{oc} [42-43]. It is generally accepted that, simplistically, the V_{oc} follows [44]:

$$V_{oc} = \frac{1}{e}\left(\left|E_{HOMO}^{Donor}\right| - \left|E_{LUMO}^{Acceptor}\right|\right) - 0.3V \qquad \{2.12\}$$

where *e* is the elementary charge and E is the energy of the corresponding component's energy level. The empirical factor of 0.3 V in equation 2.12 accounts for the difference between the V_{oc} and the built-in voltage.

Another study observed a similar relation for the V_{oc} with the empirical factor instead accounting for the binding energy of the geminate pair after charge transfer [45]. It has also been seen that the V_{oc} can have a dependence on charge transfer states [46], recombination [47] and light intensity [47-49]. Careful energy level matching between the work function of the anode and cathode electrodes with the active layer components (either through careful material selection or the introduction of buffer layers

[50-52]) can also have an influence. Similarly, the morphology of the active layer may alter the device V_{oc} [53-54].

The uses of a buffer layer between the materials and the metal electrodes (more details can be found in Section 3.3 and Chapter 4) have been used to improve device performance. The primary objective of such a layer is to reduce the energy barrier for charge extraction (thus preventing losses to the device V_{oc}), but can also provide protection for the active semiconductor from oxygen and humidity [55]. Furthermore, they can block charges (reduce charge leakage) [51,56] as well as redistributing the electric field distribution [57-58] (detailed in Section 3.10). The use of such layers have become common practise in OPV devices.

2.6.5 – Device characterisation

Characterisation of device performance is typically obtained by measuring a J-V curve under simulated solar radiation. Here, the device is subjected to an applied voltage while under illumination such that photogeneration, exciton diffusion, dissociation, and extraction may be performed. The power conversion efficiency (PCE) of the device is therefore governed by the effectiveness of these processes. Figure 2.13 displays a typical J-V curve with the parameters of interest annotated. Note that short-circuit is at V = 0 V, and open-circuit is when J = 0 $mAcm^{-2}$.

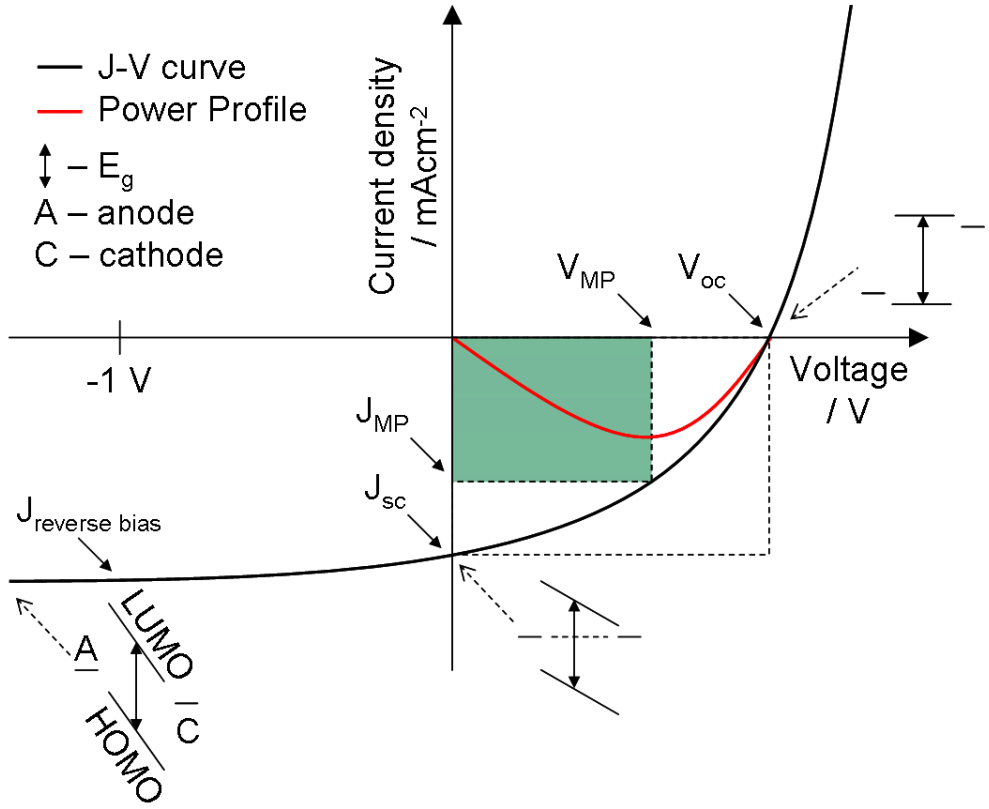

Figure 2.13 J-V characteristic displaying the location of $J_{reverse\ bias}$, J_{sc}, V_{oc}, J_{MP} and V_{MP}. A power profile is also shown to highlight the maximum power point. The green box denotes the maximum power, used for calculating the fill factor of the device. Energy level tilting due to the applied voltage is also demonstrated at reverse bias, short-circuit and open-circuit.

The device performance can then be calculated by:

$$PCE = \frac{P_{out}}{P_{in}} = \frac{J_{MP}V_{MP}}{P_{in}} = \frac{J_{sc}V_{oc}FF}{P_{in}} \qquad \{2.13\}$$

where P_{out} (P_{in}) is the output (input) power, $_{MP}$ represents the maximum power point of the device, J_{sc} is the short-circuit current, V_{oc} is the open-circuit voltage and *FF* is the fill factor, which is defined as:

$$FF = \frac{J_{MP}V_{MP}}{J_{sc}V_{oc}} \qquad \{2.14\}$$

The J-V characteristic of a highly efficient device will therefore include a deep lying J_{sc}, a high V_{oc} and a sharp curve at maximum power (for high FF values). Since OPV devices are designed to transport charges in a certain direction, the J-V characteristics may be expressed via a diode law. The equation for a non-ideal diode is given by:

$$J = J_0\left(\exp\left(\frac{eV}{nkT}\right)-1\right) \qquad \{2.15\}$$

where J_0 is the dark current, V the voltage and n the diode ideality factor (a value between 1 and 2). This does not take into account the various resistances within a device or the photocurrent produced when under illumination. Therefore, equation 2.15 can be modified to take these parameters into consideration:

$$J = J_0\left[\exp\left(\frac{e}{nkT}\left(V - JR_s\right)\right)-1\right] + \frac{V - JR_s}{R_p} - J_{ph} \qquad \{2.16\}$$

In equation 2.16, R_s is the series resistance (accounting for resistance of bulk transport, interface transfer and transport through the contacts), R_p is the parallel resistance (or shunt resistance which accounts for leakage in the device) and J_{ph} is the photocurrent. The expression J_0 multiplied by the square parentheses describes the diode current.

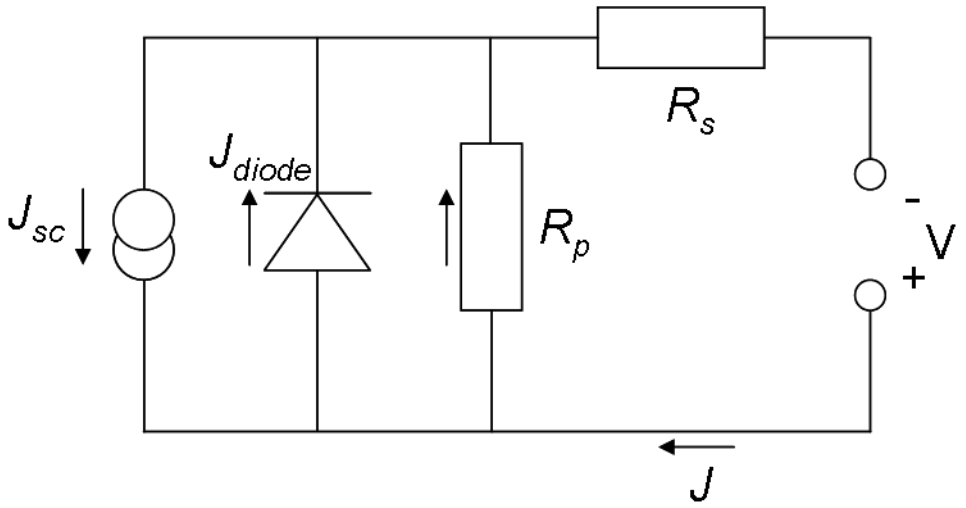

Figure 2.14 Equivalent circuit of an OPV device where J can be expressed by equation 2.16. Note that a capacitor is omitted as it may be contained within the diode and once it has been filled, the presented circuit holds true.

An organic photovoltaic device can be expressed as an equivalent circuit, as shown in Figure 2.14. For an ideal device, it can be seen that a large value of R_p will prevent current leakage and a small value of R_s will improve performance by reducing the resistance within the device (i.e. from bulk transport, interface transfer as well as the transport through contacts). These parameters have a distinct influence on the shape of the J-V curve with R_p primarily affecting the slope of the diode at short circuit and R_s influencing

the slope around open-circuit [59-60], as shown in Figure 2.15. Both parameters clearly have a parasitic effect on the device FF.

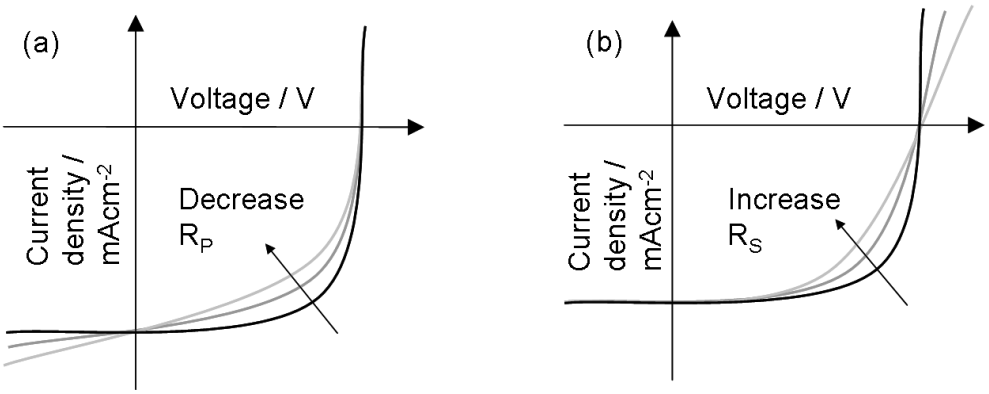

Figure 2.15 J-V curves representing the influence of (a) the parallel resistance R_p and (b) the series resistance R_s.

2.7 – Organic photovoltaic architecture

The architecture of an OPV device has evolved throughout the years. Initial devices were based on a single junction, where one material was deposited between two metal electrodes that possessed different work functions and therefore created an internal electric field. However, the efficiency of such devices was restricted to < 1% due to poor FF values (most likely due to large series resistances and/or because of the strong exciton binding energy). For example, Ghosh et al. positioned a tetracene active layer between aluminium and gold electrodes creating a device having an efficiency of 10^{-4}% in 1973 [61]. The same group further enhanced performance to 0.7% by using a merocyanine dye [62].

The use of a heterojunction (or bilayer) consisting of a thermally evaporated copper phthalocyanine (CuPc) layer followed by a perylene tetracarboxylic

derivative (PV) was implemented in 1986, with a PCE of ~ 1% being realised [63]. This device also incorporated a transparent indium tin oxide (ITO) electrode, which is now common practice for OPVs. The primary advantage of this device was the large improvement in the FF, with values of 65% being observed (compared with ~ 30% from merocyanine devices [62,64]). The bilayer architecture presented a method to dissociate excitons, with one material being used to transport holes (donor) and the other electrons (acceptor).

However, as described by equation 2.7, excitons must be created within a distance equivalent to the exciton diffusion length from an interface to allow the possibility of dissociation. Therefore, although this heterojunction provided an increase in device performance, losses were still present as only excitons created near the donor-acceptor interface could be separated into free charge carriers. A different architecture was incorporated in 1995 that addressed the losses observed from polymer-based heterojunction devices [65-66]. This type of device was termed a bulk heterojunction (or BHJ), and consisted of two materials that were intimately mixed together. Although such a structure can be formed via co-evaporation of low molecular weight molecules [67] or small molecules [68-69], solution processed materials can also be utilised. The choice of solvent for solution processed materials can help determine the resultant active layer morphology. The evaporation rate of a solvent, as well as the material's solubility, can play a crucial role in defining the length-scales of phase separation (the de-mixing of the two materials in a thin film). In an ideal device, the length-scales of phase

separation should be commensurate with the exciton diffusion length, but not so fine that it cannot form an interpenetrating network to extract charges.

A different architecture used for bulk heterojunction active layers is an inverted device structure where the ITO layer is instead utilised as the electron withdrawing electrode (i.e. the cathode). Inverted devices use a variety of different buffer layers at both electrodes while device operation is mostly unchanged. For example, a PTB7:$PC_{70}BM$ device with an ITO/PFN cathode and a MoOx/Al(or Ag) anode has realised device efficiency of 9.2% due to improved light harvesting capabilities [70]. Inverted devices have the ability to use air-stable high work function buffer layers and metal electrodes. This reduces the possibility of oxidation of these layers compared with the typical low work function materials in a normal architecture. The vertical stratification of the active layer may also be a reason for the use of an inverted device architecture. Despite these improvements, maximum device efficiencies are similar for both normal and inverted device architectures.

An alternative architecture is to use a multi-junction (tandem) cell. An energy level diagram of a typical device is displayed in Figure 2.16. Here, two (or more) sub-cells are combined by an intermediate recombination layer and can be processed by solution processing or thermal evaporation. Each sub-cell is designed to harvest the solar spectrum at distinct wavelengths to allow the overall device the opportunity to absorb a greater

portion of sunlight. This allows the device to reduce losses via thermalisation of absorbed photons with energy greater than the optical energy gap. Careful selection of the materials used for the recombination layer is also needed to satisfy the following requirements, among others [71]: high transparency, balanced recombination, processing conditions, and stability. Efficient devices have recently utilised a PEDOT:PSS and zinc oxide (ZnO) recombination layer allowing PCEs greater than 7%.

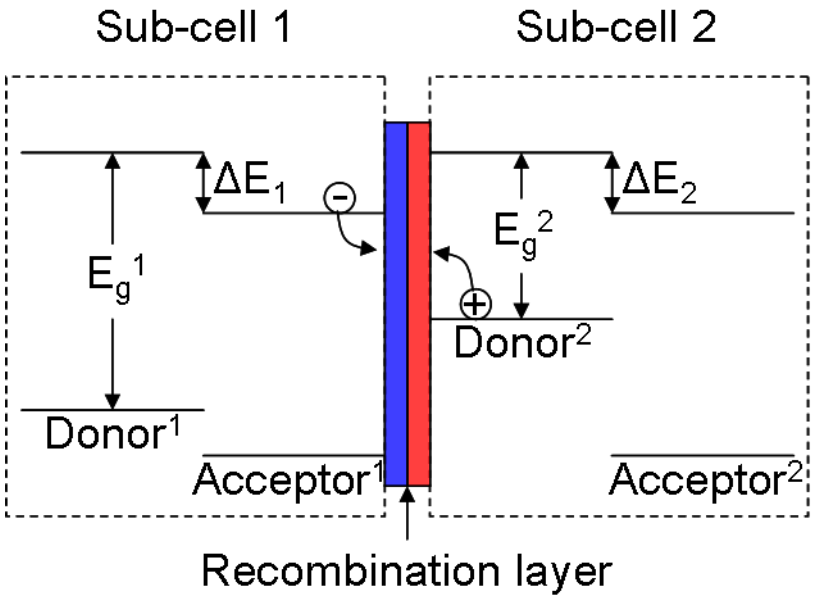

Figure 2.16 Energy level diagram of a two sub-cell tandem device, with donors of differing energy gap E_g. Sub-cell 1 uses a polymer with a greater energy gap to reduce thermalisation losses. The acceptors are represented by a similar material, although this does not need to be the case. The blue (red) part of the recombination layer represents the electron (hole) transporting layer.

The most efficient tandem devices reported have been 10.6% [72] and 12% [73] for polymer and small molecule active layers respectively. The overall device metrics of the tandem cell strongly depends on the individual cells. It can be seen that the overall V_{oc} is given by the sum of the V_{oc} of the individual sub-cells, as evident from review articles, for example [71]. The short circuit current, J_{sc}, is governed by the sub-cell with the smallest individual value. Therefore, careful consideration of the materials used in all sub-cells (as well as the recombination layer) is important to reduce losses in tandem devices.

2.8 – Fullerenes

Fullerenes are the most common electron-accepting materials used in OPV devices. It was found that photoinduced charge transfer to the buckminsterfullerene C_{60} was fast and efficient [74]. Fullerenes were also shown to have an electron mobility of 1 $cm^2V^{-1}s^{-1}$ in OFETs [75]. A more soluble version of C_{60} was achieved by functionalisation with a methyl-ester group to give $PC_{60}BM$ [66]. An alternative fullerene derivative which has also been widely used in OPVs is $PC_{70}BM$, which has a higher absorption coefficient in the visible range of the solar spectrum than $PC_{60}BM$. The difference in absorption coefficient has been attributed to the high degree of symmetry in C_{60} where low energy transitions are dipole forbidden thereby requiring higher energy photons [76-77]. However, C_{70} derivative has reduced symmetry therefore allowing such previously forbidden transitions to be possible. Although the majority of absorption in an OPV polymer:fullerene device comes from absorption by the donor polymer (due

to its high absorption coefficient), the blend ratios for efficient devices often have a large yield of fullerene. This is to reduce the distance an exciton must travel to encounter a donor:acceptor interface for charge separation. A gap in UV-Vis spectra in the 400-500 nm range from donor materials can be filled through the use of $PC_{70}BM$. These fullerene systems, along with many other derivatives, have continued to be used in OPV BHJ devices because of efficient charge transfer and electron mobility. Alternative acceptor materials have been explored, for example the polymer P(NDI2OD-T2) [78] has displayed very high electron mobilities [79], however OPV device efficiency is poor; an effect primarily attributed to rapid geminate recombination [80].

2.9 – PEDOT:PSS

Although the majority of OPV device research has focused on the development of donor systems for the active region, there is one polymer which has been widely used as an anode buffer layer. PEDOT:PSS, displayed in Figure 2.17, is a molecularly doped conjugated polymer that aids the charge extraction process at the anode electrode. The PSS dopant is required to allow PEDOT to be soluble [81]. Furthermore, the presence of PSS causes a net positive charge along the PEDOT chain which results in the two components to be closely linked together. This results in the formation of nanoparticles within aqueous solutions. Additionally, a free π-electron remains on the main chain which is highly mobile, resulting in large charge carrier mobilities being observed [82].

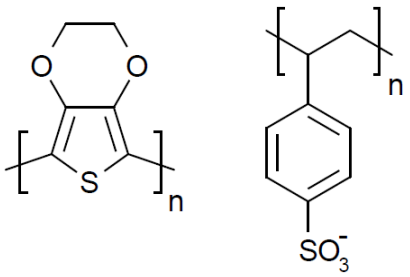

Figure 2.17 PEDOT and PSS chemical structure. PEDOT:PSS is mixed at a blend ratio of 1:6 in water.

PEDOT:PSS is typically deposited by spin casting from an aqueous solution and has a higher work function than the ITO anode; allowing energy level matching with donor polymer materials. Another advantage is that PEDOT:PSS can reduce the roughness of the ITO allowing a smoother platform for the donor:acceptor layer, as observed from organic light emitting diodes [83]. This allows a reduction in the probability of electrical shortages and inhomogeneities at the active layer:anode interface. However, as discussed in further detail in Section 4.1, this polymer is not best suited for a variety of new polymer systems that possess deeper HOMO energy levels, having the properties of improved operational stability as well as leading to increased open circuit voltage.

2.10 – Thesis polymer list

This final section displays the full name and chemical structure of all the donor polymer systems used within the remainder of the thesis. The number(s) contained inside the square parentheses next to each polymer acronym represents the chapters in which that polymer is explored.

PCDTBT [4,5,6]

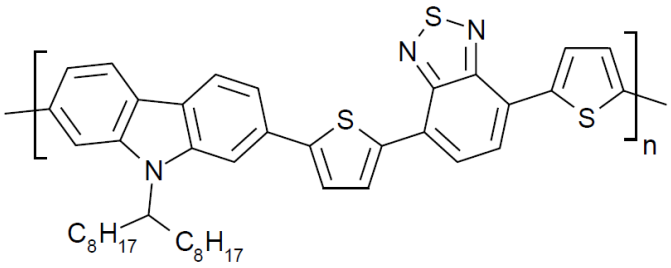

Poly[N-9’-heptadecanyl-2,7-carbazole-alt-5,5-(4’,7’-di-2-thienyl-2’,1’,3’-benzothiadiazole)]

PCDTBT-8 [5,6]

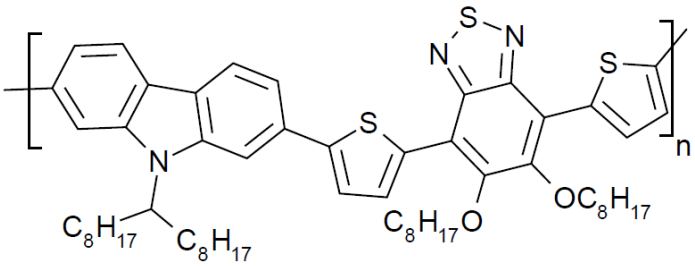

Poly[9-(heptadecan-9-yl)-9H-carbazole-2,7-diyl-alt-(5,6-bis(octyloxy)-4,7-di(thiophen-2-yl)benzo[c][1,2,5]thiadiazole)-5,5-diyl]

PCDT2BT-8 [5,7]

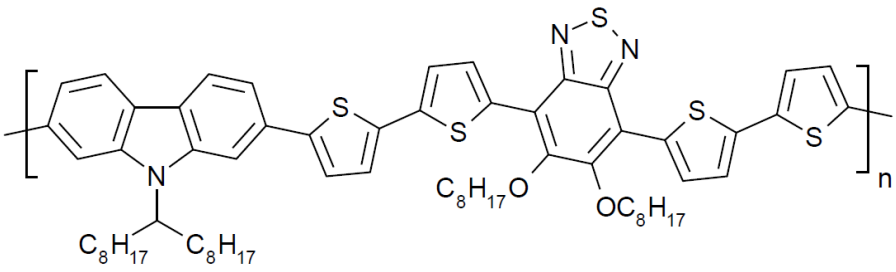

Poly[9-(heptadecan-9-yl)-9H-carbazole-2,7-diyl-alt-(5,6-bis(octyloxy)-4,7-di(2,2’-bithiophen-5-yl)benzo[c][1,2,5]thiadiazole-5,5-diyl]

PCDSeBT [6]

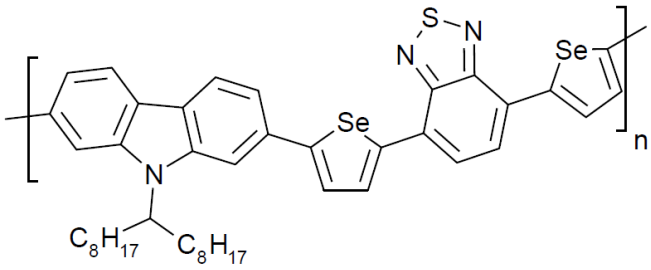

Poly[9-(heptadecan-9-yl)-9H-carbazole-2,7-diyl-alt(4’,7’-di-2-selenophenyl-2’,1’,3’-benzothiadiazole)-5,5-diyl]

PFDTBT [6]

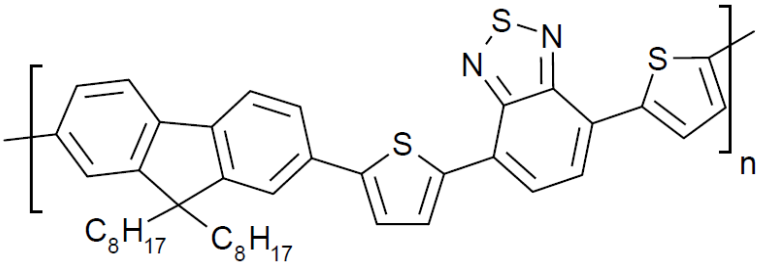

Poly[9,9-dioctyl-9H-fluorene-2,7-diyl-alt-(4’,7’-di-thiophen-2-yl)-2’,1’,3’-benzothiadiazole-5,5-diyl]

PFDSeBT [6]

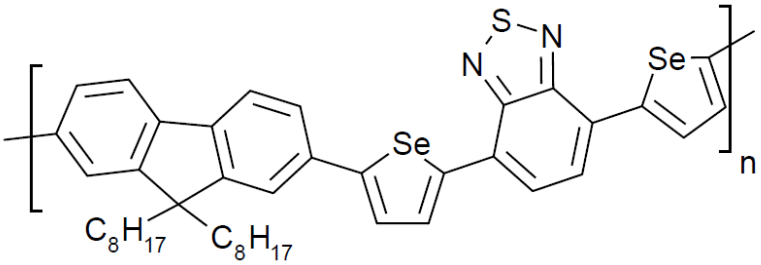

Poly[9,9-dioctyl-9H-fluorene-2,7-diyl-alt(4’,7’-di-2-selenophenyl-2’,1’,3’-benzothiadiazole)-5,5-diyl]

PCDSeBT-8 [6]

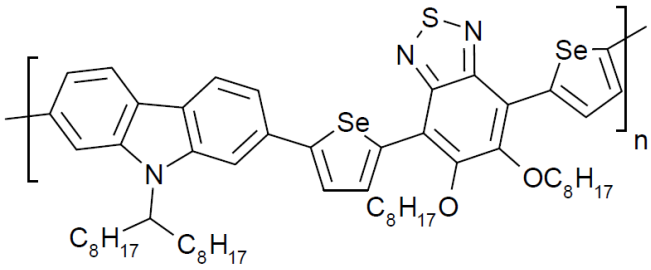

Poly[9-(heptadecan-9-yl)-9H-carbazole-2,7-diyl-alt-(5,6-bis(octyloxy)-4,7-di(selenophen-2-yl)benzo[c][1,2,5]thiadiazole-5,5-diyl]

PFDTBT-8 [6,7]

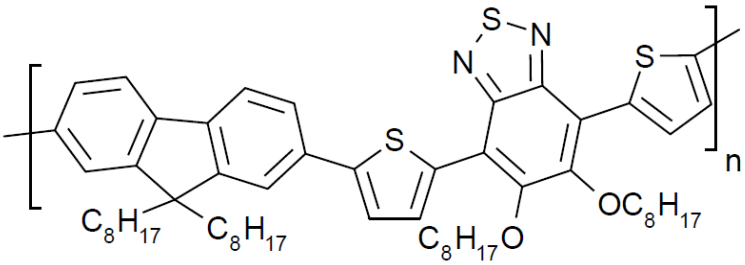

Poly[9,9-dioctyl-9H-fluorene-2,7-diyl-alt-(5,6-bis-(octyloxy)-4,7-di(thiophen-2-yl)benzo[c][1,2,5]thiadiazole)-5,5-diyl]

PFDSeBT-8 [6]

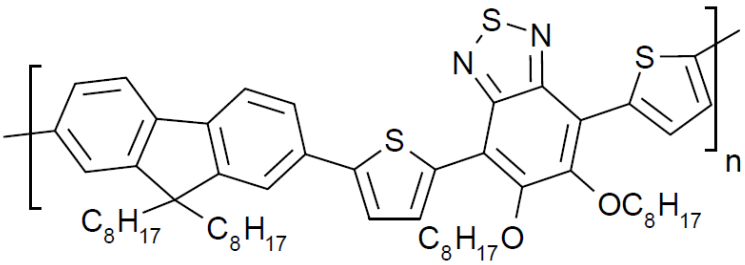

Poly[9,9-dioctyl-9H-fluorene,2-7-diyl-alt-(5,6-bis(octyloxy)-4,7-di(selenophen-2-yl)benzo[c][1,2,5]thiadiazole-5,5-diyl]

PFDT2BT-8 [7]

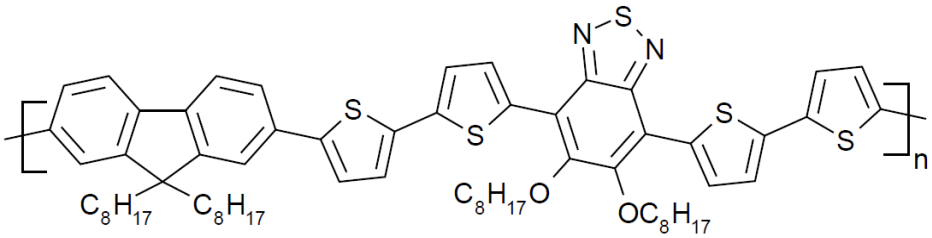

Poly[9,9-dioctylfluorene-2,7-alt-(5,6-bis(octyloxy)-4,7-di(2,2'-bithiophen-5-yl)benzo[c][1,2,5]thiadiazole)-5,5-diyl]

2.10.1 – Moiety structure and name

For ease, the following is a list of all the moieties (name, abbreviation and structure) within the above polymers.

C (Carbazole)

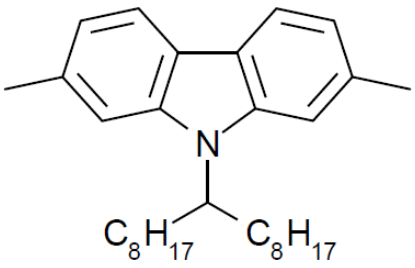

F (Fluorene)

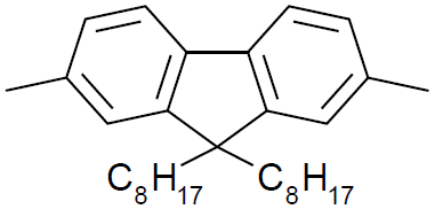

BT (Benzothiadiazole)

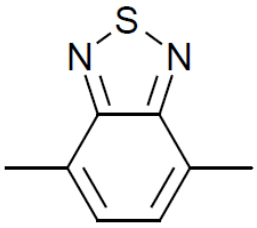

BT-8 (BT with bis(octyloxy))

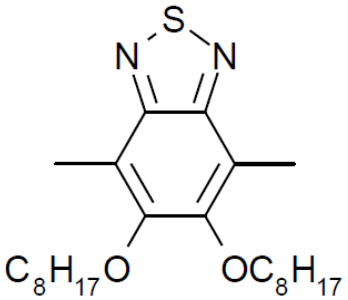

DTBT (dithiophenyl-BT)

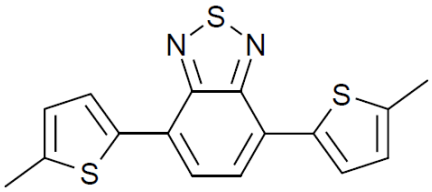

DSeBT (diselenophenyl-BT)

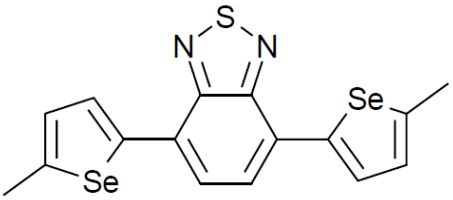

DT2BT-8 (di(bithiophenyl)-BT-8)

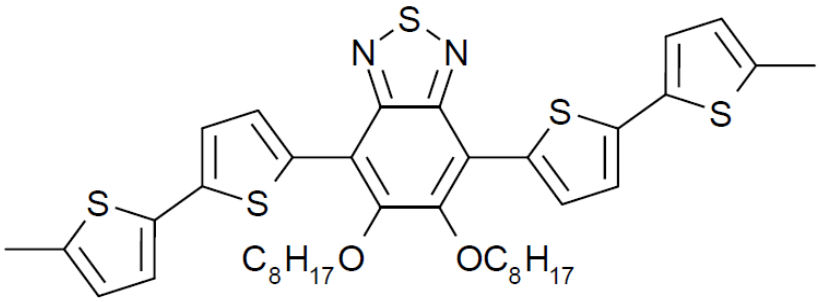

References

1. H. Shirakawa, E.J. Louis, A.G. MacDiarmid, C.K. Chiang, A.J. Heeger, Synthesis of electrically conducting organic polymers: halogen derivatives of polyacetylene, $(CH)_x$, *J. Chem. Soc., Chem. Commun.*, **1977**, 578-580
2. R.E. Peierls, *Quantum theory of solids*, 1st Edition, Clarendon Press, Oxford **1955**
3. C.S. Yannoni, T.C. Clarke, Molecular geometry of cis- and trans-polyacetylene by nutation NMR spectroscopy, *Phys. Rev. Lett.*, **1983**, *51*, 1191-1193
4. A.O. Patil, A.J. Heeger, F. Wudl, Optical properties of conducting polymers, *Chem. Rev.*, **1988**, *88*, 183-200

5. R.V. Kasowski, W.Y. Hsu, E.B. Caruthers, Electronic properties of polyacetylene, polyethylene, and polytetrafluoroethylene, *J. Chem. Phys.*, **1980**, *72*, 4896-4900
6. F. Wudl, M. Kobayashi, A.J. Heeger, Poly(isothianaphthene), *J. Org. Chem.*, **1984**, *49*, 3382-3384
7. Y. Liang, Y. Wu, D. Feng, S.-T. Tsai, H.-J. Son, G. Li, L. Yu, Development of new semiconducting polymers for high performance solar cells, *J. Am. Chem. Soc.*, **2009**, *131*, 56-57
8. Y. Liang, D. Feng, Y. Wu, S.-T. Tsai, G. Li, C. Ray, L. Yu, Highly efficient solar cell polymers developed via fine-tuning of structural and electronic properties, *J. Am. Chem. Soc.*, **2009**, *131*, 7792-7799
9. Y. Liang, Z. Xu, J. Xia, S.-T. Tsai, Y. Wu, G. Li, C. Ray, L. Yu, For the bright future – bulk heterojunction polymer solar cells with power conversion efficiency of 7.4%, *Adv. Mater.*, **2010**, *22*, E135-E138
10. H.-Y. Chen, J. Hou, S. Zhang, Y. Liang, G. Yang, Y. Yang, L. Yu, Y. Wu, G. Li, Polymer solar cells with enhanced open-circuit voltage and efficiency, *Nat. Photonics*, **2009**, *3*, 649-653
11. J. Hou, H.-Y. Chen, S. Zhang, R.I. Chen, Y. Yang, Y. Wu, G. Li, Synthesis of a low bang gap polymer and its application in highly efficient polymer solar cells, *J. Am. Chem. Soc.*, **2009**, *131*, 15586-15587
12. L. Huo, S. Zhang, X. Guo, F. Xu, Y. Li, J. Hou, Replacing alkoxy groups with alkylthienyl groups: a feasible approach to improve the properties of photovoltaic polymers, *Angew. Chem.*, **2011**, *123*, 9871-9876

13. S.C. Price, A.C. Stuart, L. Yang, H. Zhou, W. You, Fluorine substituted conjugated polymer of medium band gap yields 7% efficiency in polymer-fullerene solar cells, *J. Am. Chem. Soc.*, **2011**, *133*, 4625-4631
14. Y. Zhang, J. Zou, C.-C. Cheuh, H.-L. Yip, A.K.-Y. Jen, Significant improved performance of photovoltaic cells made from a partially fluorinated cyclopentadithiophene/benzothiadiazole conjugated polymer, *Macromolecules*, **2012**, *45*, 5427-5435
15. S. Albrecht, S. Janietz, W. Schindler, J. Frisch, J. Kurpiers, J. Kniepert, S. Inal, P. Pingel, K. Fostiropoulos, N. Koch, D. Neher, Fluorinated copolymer PCPDTBT with enhanced open-circuit voltage and reduced recombination for highly efficienct polymer solar cells, *J. Am. Chem. Soc.*, **2012**, *134*, 14932-14944
16. A.C. Stuart, J.R. Tumbleston, H. Zhou, W. Li, S. Liu, H. Ade, W. You, Fluorine substituents reduce charge recombination and drive structure and morphology development in polymer solar cells, *J. Am. Chem. Soc.*, **2013**, *135*, 1806-1815
17. Z.–G. Zhang, J. Wang, Structures and properties of conjugated donor-acceptor copolymers for solar cell applications, *J. Mater. Chem.*, **2012**, *22*, 4178-4187
18. R.S. Kularatne, H.D. Magurudeniya, P. Sista, M.C. Biewer, M.C. Stefan, Donor-acceptor semiconducting polymers for organic solar cells, *J. Polym. Sci. A Polym. Chem.*, **2013**, *51*, 743-768
19. M. Heeney, W. Zhang, D.J. Crouch, M.L. Chabinyc, S. Gordeyev, R. Hamilton, S.J. Higgins, I. McCulloch, P.J. Skabara, D. Sparrowe, S.

Tierney, Regioregular poly(3-hexyl)selenophene: a low band gap organic hole transporting polymer, *Chem. Commun.*, **2007**, 5061-5063

20. C.H. Woo, P.M. Beaujuge, T.W. Holcombe, O.P. Lee, J.M.J. Fréchet, Incorporation of furan into low band-gap polymers for efficient solar cells, *J. Am. Chem. Soc.*, **2010**, *132*, 15547-15549
21. A. Bhuwalka, J.F. Mike, M. He, J.J. Intemann, T. Nelson, M.D. Ewan, R.A. Roggers, Z. Lin, M. Jeffries-EL, Quaterthiophene-benzobisazole copolymers for photovoltaic cells: effect of heteroatom placement and substitution on the optical and electronic properties, *Macromolecules*, **2011**, *44*, 9611-9617
22. B. Kim, H.R. Yeom, M.H. Yun, J.Y. Kim, C. Yang, A selenophene analogue of PCDTBT: selective fine-tuning of LUMO to lower of the bandgap for efficient polymer solar cells, *Macromolecules*, **2012**, *45*, 8658-8664
23. S. Das, P.B. Pati, S.S. Zade, Cyclopenta[c]thiophene-based D-A conjugated copolymers: effect of heteroatoms (S, Se, and N) of benzazole acceptors on the properties of polymers, *Macromolecules*, **2012**, *45*, 5410-5417
24. S. Beaupré, A. Pron, S.H. Drouin, A. Najari, L.G. Mercier, A. Robitaille, M. Leclerc, Thieno-, furo-, and selenopheno[3,4-c]pyrrole-4,6-dione copolymers: effect of the heteroatom on the electrooptical properties, *Macromolecules*, **2012**, *45*, 6906-6914
25. E. Wang, M. Wang, L. Wang, C. Duan, J. Zhang, W. Cai, C. He, H. Wu, Y. Cao, Donor polymers containing benzothiadiazole and four thiophene

rings in their repeating units with improved photovoltaic performance, *Macromolecules*, **2009**, *42*, 4410-4415

26. H. Bronstein, D.S. Leem, R. Hamilton, P. Woebkenberg, S. King, W. Zhang, R.S. Ashraf, M. Heeney, T.D. Anthopoulos, J. de Mello, I. McCulloch, Indacenodithiophene-co-benzothiadiazole copolymers for high performance solar cells or transistors via alkyl chain optimization, *Macromolecules*, **2011**, *44*, 6649-6652
27. M. Pope, C.E. Swenberg, *Electronic processes in organic crystals and polymers*, 2nd Edition, Oxford University Press, New York, **1999**, p25
28. T.M. Clarke, J.R. Durrant, Charge photogeneration in organic solar cells, *Chem. Rev.*, **2010**, 6736-6767
29. J.-W. van der Horst, P.A. Bobbert, P.H.L. de Jong, M.A.J. Michels, G.Brocks, P.J. Kelly, Ab initio prediction of the electronic and optical excitations in polythiophene: isolated chains versus bulk polymer, *Phys. Rev. B*, **2000**, *61*, 15817-15826
30. J.-L. Brédas, D. Beljonne, V. Coropceanu, J. Cornil, Charge-transfer and energy-transfer processes in π-conjugated oligomers and polymers: a molecular picture, *Chem. Rev.*, **2004**, *104*, 4971-5003
31. B.C. Thompson, J.M.J. Fréchet, Polymer-fullerene composite solar cells, *Angew. Chem. Int. Ed.*, **2007**, *47*, 58-77
32. L.A.A. Pettersson, L.S. Roman, O. Inganäs, Modeling photocurrent action spectra of photovoltaic devices based on organic thin films, *J. Appl. Phys.*, **1999**, *86*, 487

33. J.-L. Brédas, J.E. Norton, J. Cornil, V. Coropceanu, Molecular understanding of organic solar cells: the challenges, *Acc. Chem. Res.*, **2009**, *42*, 1691-1699

34. J.R. Lakowicz, *Principles of fluorescence spectroscopy*, 3rd Edition, Springer, New York, **2006**

35. A.J. Heeger, N.S. Sariciftci, E.B. Namdas, *Semiconducting and metallic polymers*, 1st edition, Oxford University Press, Oxford, **2010**

36. M.A. Faist, T. Kirchartz, W. Gong, R.S. Ashraf, I. McCulloch, J.C. de Mello, N.J. Ekins-Daukes, D.D.C. Bradley, J. Nelson, Competition between the charge transfer state and the singlet states of donor or acceptor limiting the efficiency in polymer:fullerene solar cells, *J. Am. Chem. Soc.*, **2012**, *134*, 685-692

37. L.J.A. Koster, V.D. Mihailetchi, P.W.M. Blom, Ultimate efficiency of polymer/fullerene bulk heterojunction solar cells, *Appl. Phys. Lett.*, **2006**, *88*, 093511

38. D. Hertel, H. Bässler, Photoconduction in amorphous organic solids, **2008**, *Chemphyschem*, **2008**, *9*, 666-688

39. L. Kador, Stochastic theory of inhomogeneous spectroscopic line shapes reinvestigated, *J. Chem. Phys.*, **1991**, *95*, 5574-5581

40. A. Miller, E. Abrahams, Impurity conduction at low concentrations, *Phys. Rev.*, **1960**, *120*, 745-755

41. M. van der Auweraer, F.C. De Schryver, P.M. Borsenberger, H. Bässler, Disorder in charge transport in doped polymers, *Adv. Mater.*, **1994**, *6*, 199-213

42. C.J. Brabec, A. Cravino, D. Meissner, N.S. Sariciftci, T. Fromherz, M.T. Rispens, L. Sanchez, J.C. Hummelen, Origin of the open circuit voltage of plastic solar cells, *Adv. Funct. Mater.*, **2001**, *11*, 374-380

43. I. Riedel, J. Parisi, V. Dyakonov, L. Lutsen, D. Vanderzande, J.C. Hummelen, Effect of temperature and illumination on the electrical properties of polymer-fullerene bulk-heterojunction solar cells, *Adv. Funct. Mater.*, **2004**, *14*, 38-44

44. M.C. Scharber, D. Mühlbacher, M. Koppe, P. Denk, C. Waldauf, A.J. Heeger, C.J. Brabec, Design rules for donors in bulk-heterojunction solar cells – towards 10% energy-conversion efficiency, *Adv. Mater.*, **2006**, *18*, 789-794

45. B.P. Rand, D.P. Burk, S.R. Forrest, Offset energies at organic semiconductor heterojunctions and their influence on the open-circuit voltage of thin-film solar cells, *Phys. Rev. B*, **2007**, *75*, 115327

46. K. Vandewal, K. Tvingstedt, A. Gadisa, O Inganäs, J.V. Manca, On the origin of the open-circuit voltage of polymer-fullerene solar cells, *Nat. Mater.*, **2009**, *8*, 904-909

47. A. Maurano, R. Hamilton, C.G. Shuttle, A.M. Ballantyne, J. Nelson, B. O'Regan, W. Zhang, I. McCulloch, H. Azimi, M. Morana, C.J. Brabec, J.R. Durrant, Recombination dynamics as a key determinant of open circuit voltage in organic bulk heterojunction solar cells: a comparison of four different donor polymers, *Adv. Mater.*, **2010**, *22*, 4987-4992

48. P. Schilinsky, C. Waldauf, J. Hauch, C.J. Brabec, Simulation of light intensity dependent current characteristics of polymer solar cells, *Appl. Phys. Lett.*, **2004**, *95*, 2816

49. L.J.A. Koster, V.D. Mihailetchi, R. Ramaker, P.W.M. Blom, Light intensity dependence of open-circuit voltage of polymer:fullerene solar cells, *Appl. Phys. Lett.*, **2005**, *86*, 123509

50. C.J. Brabec, S.E. Shaheen, C. Winder, N.S. Sariciftci, P. Denk, Effect of LiF/metal electrodes on the performance of plastic solar cells, *Appl. Phys. Lett.*, **2002**, *80*, 1288

51. Z. He, C. Zhong, X. Huang, W.-Y. Wong, H. Wu, L. Chen, S. Su, Y. Cao, Simultaneous enhancement of open-circuit voltage, short-circuit current density, and fill factor in polymer solar cells, *Adv. Mater.*, **2011**, *23*, 4636-4643

52. Y. Sun, C.J. Takacs, S.R. Cowan, J.H. Seo, X. Gong, A. Roy, A.J. Heeger, Efficient, air-stable bulk heterojunction polymer solar cells using MoOx as the anode interfacial layer, *Adv. Mater.*, **2011**, *23*, 2226-2230

53. J. Liu, Y. Shi, Y. Yang, Solvation-induced morphology effects on the performance of polymer-based photovoltaic devices, *Adv. Funct. Mater.*, **2001**, *11*, 420-424

54. H. Hoppe, M. Niggemann, C. Winder, J. Kraut, R. Hiesgen, A. Hinsch, D. Meissner, N.S. Sariciftci, Nanoscale morphology of conjugated polymer/fullerene-based bulk-heterojunction solar cells, *Adv. Funct. Mater.*, **2004**, *14*, 1005-1011

55. K. Lee, J.Y. Kim, S.H. Park, S.H. Kim, S. Cho, A.J. Heeger, Air-stable polymer electronic devices, *Adv. Mater.*, **2007**, *19*, 2445-2449

56. S.H. Park, A. Roy, S. Beaupré, S. Cho, N. Coates, J.S. Moon, D. Moses, M. Leclerc, K. Lee, A.J. Heeger, Bulk heterojunction solar cells with

internal quantum efficiency approaching 100%, *Nat. Photonics*, **2009**, *3*, 297-302

57. B.V. Andersson, D.M. Huang, A.J. Moulé, O. Inganäs, An optical spacer is no panacea for light collection in organic solar cells, *Appl. Phys. Lett.*, **2009**, *94*, 043302
58. R. Po, C. Carbonera, A. Bernardi, N. Camaioni, The role of buffer layer in polymer solar cells, *Energy Environ. Sci.*, **2011**, *4*, 285-310
59. J. D. Servaites, S. Yeganeh, T.J. Marks, M.A. Ratner, Efficiency enhancement in organic photovoltaic cells: consequences of optimizing series resistance, *Adv. Funct. Mater.*, **2010**, *20*, 97-104
60. R.A. Street, K.W. Song, S. Cowan, Influence of series resistance on the photocurrent analysis of organic solar cells, *Org. Electron.*, **2011**, *12*, 244-248
61. A.K. Ghosh, T. Feng, Rectification, space-charge-limited current, photovoltaic and photoconductive properties of Al/tetracene/Au sandwich cell, *J. Appl. Phys.*, **1973**, *44*, 2781-2788
62. A.K. Ghosh, T. Feng, Merocyanine organic solar cells, *J. Appl. Phys.*, **1978**, *49*, 5982-5989
63. C.W. Tang, Two-layer organic photovoltaic cell, *Appl. Phys. Lett.*, **1986**, *48*, 183-185
64. T. Moriizumi, K. Kudo, Merocyanine-dye photovoltaic cell on a plastic film, *Appl. Phys. Lett.*, **1981**, *38*, 85-86
65. J.J.M. Halls, C.A. Walsh, N.C. Greenham, E.A. Marseglia, R.H. Friend, S.C. Moratti, A.B. Holmes, Efficient photodiodes from interpenetrating polymer networks, *Nature*, **1995**, *376*, 498-500

66. G. Yu, J. Gao, J.C. Hummelen, F. Wudl, A.J. Heeger, Polymer photovoltaic cells – enhanced efficiencies via a network of internal donor-acceptor heterojunctions, *Science*, **1995**, *270*, 1789-1791
67. M. Hiramoto, H. Fujiwara, M. Yokoyama, p-i-n like behavior in three-layered organic solar cells having a co-deposited interlayer of pigments, *J. Appl. Phys.*, **1992**, *72*, 3781
68. S. Uchida, J. Xue, B.P. Rand, S.R. Forrest, Organic small molecule solar cells with a homogeneously mixed copper phthalocyanine:C60 active layer, *Appl. Phys. Lett.*, **2004**, *84*, 4218
69. J. Sakai, T. Taima, T. Yamanari, K. Saito, Annealing effect in the sexithiophene:C70 small molecule bulk heterojunction organic photovoltaic cells, *Sol. Energy Mater. Sol. Cell*, **2009**, *93*, 1149-1153
70. Z. He, C. Zhong, S. Su, M. Xu, H. Wu, Y. Cao, Enhanced power-conversion efficiency in polymer solar cells using an inverted device structure, *Nat. Photonics*, **2012**, *6*, 591-595
71. T. Ameri, N. Li, C.J. Brabec, Highly efficient organic tandem solar cells: a follow up review, *Energy Environ. Sci.*, **2013**, *6*, 2390-2413
72. J. You, L. Dou, K. Yoshimura, T. Kato, K. Ohya, T. Moriarty, K. Emery, C.-C. Chen, J. Gao, G. Li, Y. Yang, A polymer tandem solar cell with 10.6% power conversion efficiency, *Nat. Commun.*, **2013**, *4*, 144
73. Heliatek GmbH. Press release 2013. http://www.heliatek.com/wp-content/uploads/2013/01/130116_PR_Heliatek_achieves_record_cell_effiency_for_OPV.pdf. Accessed: November 2013

74. N.S. Sariciftci, L. Smilowitz, A.J. Heeger, F. Wudl, Photoinduced electron transfer from a conducting polymer to buckminsterfullerene, *Science*, **1992**, *258*, 1474-1476

75. Th.B. Singh, N. Marjanović, G.J. Matt, S. Günes, N.S. Sariciftci, A. Montaigne Ramil, A. Andreev, H. Sitter, R. Schwödiauer, S. Bauer, High-mobility n-channel organic field-effect transistors based on epitaxially grown C_{60} films, *Org. Electron.*, **2005**, *6*, 105-110

76. J.W. Arbogast, C.S. Foote, Photophysical properties of C_{70}, *J. Am. Chem. Soc.*, **1991**, *113*, 8886-8889

77. M.M. Wienk, J.M. Kroon, W.J.H. Verhees, J. Knol, J.C. Hummelen, P.A. van Hal, R.A.J. Janssen, Efficient methano[70]fullerene/MDMO-PPV bulk heterojunction photovoltaic cells, *Angew. Chem. Int. Ed.*, **2003**, *42*, 3371-3375

78. Z. Chen, Y. Zheng, H. Yan, A. Facchetti, Naphthalenedicarboximide- vs perylenedicarboximide-based copolymers. Synthesis and semiconducting properties in bottom-gate N-channel organic transistors, *J. Am. Chem. Soc.*, **2009**, *131*, 8-9

79. H. Yan, Z. Chen, Y. Zheng, C. Newman, J.R. Quinn, F. Dötz, M. Kastler, A. Facchetti, A high-mobility electron-transporting polymer for printed transistors, *Nature*, **2009**, *457*, 679-686

80. J.R. Moore, S. Albert-Seifried, A. Rao, S. Massip, B. Watts, D.J. Morgan, R.H. Friend, C.R. McNeill, H. Sirringhaus, Polymer blend solar cells based on a high-mobility naphthalenediimide-based polymer acceptor: device physics, photophysics and morphology, *Adv. Energy Mater.*, **2011**, *1*, 230-240

81. A.M. Nardes, M. Kemerink, M.M. de Kok, E. Vinken, K. Maturova, R.A.J. Janssen, Conductivity, work function, and environmental stability of PEDOT:PSS thin films treated with sorbitol, *Org. Electron.*, **2008**, *9*, 727-734
82. Q. Wei, M. Mukaida, Y. Naitoh, T. Ishida, Morphological change and mobility enhancement in PEDOT:PSS by adding co-solvents, *Adv. Mater.*, **2013**, *25*, 2831-2836
83. C. Jonda, A.B.R. Mayer, U. Stolz, A. Elschner, A. Karbach, Surface roughness effects and their influence on the degradation of organic light emitting devices, *J. Mater. Sci.*, **2000**, *35*, 5645-5651

Chapter 3

Experimental methods

3.1 – Introduction

The various techniques employed throughout this thesis to determine a variety of parameters for polymer thin films and OPV devices are discussed in this chapter. Details regarding the solution, thin film and device preparations are provided which account for the key processes used throughout the following chapters. The different experimental techniques used are then discussed to provide the reader with a working knowledge of the instrument/experiment and data analysis.

3.2 – Solution and thin film preparation

All materials and solvents were used as received. The polymer donor systems were supplied by the University of Sheffield Chemistry Department and the fullerene $PC_{70}BM$ (95% purity) was obtained from either Solenne or Ossila Ltd. Further details regarding the polymer energy levels and molecular weights/numbers can be found in their respective chapter (as listed in Section 2.10). All thin film preparation (excluding the PEDOT:PSS layer, see Section 3.3) were performed in a nitrogen filled glovebox.

To prepare a polymer solution, the dry polymer was initially dissolved in the chosen chlorinated solvent: either chloroform ($CHCl_3$), chlorobenzene (CB) or di-chlorobenzene (DCB). The concentration was kept constant at 4 mg/ml for all polymers (this value was found to be at the upper limit of polymer solubility for a number of materials). Polymer solutions were then heated for 1-2 days at ~ 70°C with occasional shaking to ensure all the material had completely dissolved. The solution was then cooled for a few minutes and

added to another vial containing dry $PC_{70}BM$ powder. This method of mixing the polymer solution with dry fullerene was preferred due to the low concentration of the polymer solution. The polymer:fullerene solution was placed back onto the hotplate at the same temperature for a further 1-2 day period, again to ensure all material had fully dissolved. Although some polymers dissolved more rapidly, this routine was maintained to enable comparative studies. Solutions used in Chapters 6 and 7 were not filtered as only small quantities of polymer were available. Furthermore, filtration was not performed on many solutions in order to preserve limited material.

Thin films were created via a spin coating technique. This allowed for rapid film formation due to the initial expulsion of excess solution. The remaining solvent dried after a certain amount of time, which primarily depended on the solvent boiling point as well as the spin speed. The boiling point of each solvent is approximately 61°C, 131°C and 180°C for $CHCl_3$, CB and DCB respectively. For $CHCl_3$ and CB based polymer:fullerene solutions, spin times of 30s were adequate to create fully dry films. DCB based solutions however required spin times up to 300s. For spin speeds below 500 rpm, a multi-stage process was required due to the fact the excess solution could not be ejected from the sample at these low speeds. Two techniques were employed to resolve this issue: absorbing excess solution at the start of the spin process with a cotton bud, or subjecting the sample to a secondary spin at a higher spin speed. Both techniques were used depending on the initial spin speed and solvent. In all cases, care was taken to control resultant film thickness.

The thickness of the thin films was measured via a Dektak surface profiler. The film thickness, *d*, can be determined using the following equation:

$$d = \frac{c\eta(c)}{\sqrt{\omega}} \qquad \{3.1\}$$

where c is the solution concentration, $\eta(c)$ is the solution viscosity (dependent on the concentration), and ω is the spin speed. Fine-tuning the film thickness can be achieved by altering the spin speed (with c and $\eta(c)$ being kept constant):

$$\omega = \omega_R \left(\frac{t_R}{t} \right)^2 \qquad \{3.2\}$$

where t_R and ω_R are the reference samples thickness (as determined via Dektak measurements) and spin speed respectively.

3.3 – Device preparation

Pre-patterned glass/ITO (indium tin oxide) substrates with a sheet resistance of 20 Ω/□ were used throughout. Initially, these were coated with a photo-resist to protect the ITO (substrate style 1, Figure 3.1(a)). At some point during my PhD, the substrate design changed to style 2, Figure 3.1(b), in order to reduce the series resistance of the ITO layer. For both types of substrates a cleaning routine was used as follows.

The substrates were loaded into a rack for cleaning and sonicated in a heated 10% sodium hydroxide (NaOH) solution for 5 mins. They were subsequently "dump-rinsed" in de-ionised (DI) water twice before going back into the NaOH solution and sonicated for a further 5 mins. This step was found to be crucial for substrate style 1 in order to remove a photo-resist coating layer. After a further "dump-rinse" in DI water, the samples were subjected to a final sonication in isopropyl alcohol (IPA). With no further rinses required, substrates were dried with the use of a N_2 gun.

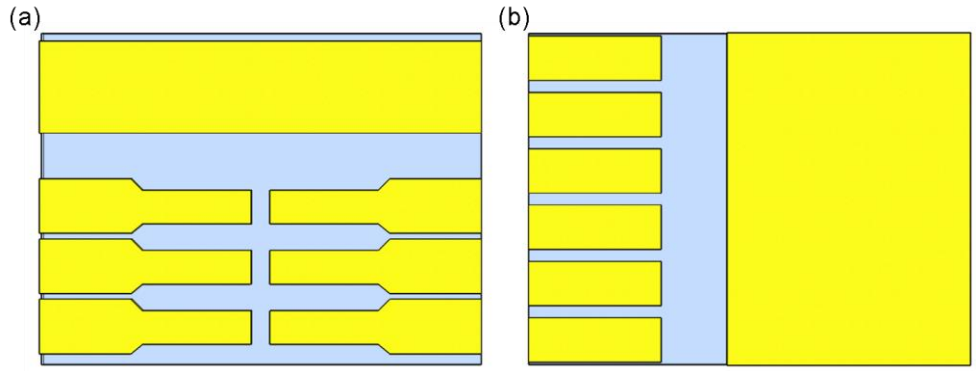

Figure 3.1 Pre-patterned glass/ITO substrate style 1 (a), and 2 (b). Both substrates are 20 x 15 mm.

Once a substrate was dried, an anode buffer layer was deposited on top of the ITO layer. This was either a PEDOT:PSS layer or a metal oxide. For PEDOT:PSS (HC Stark Clevios P VP AI4083), the dried substrate was placed in a spin-coater (performed outside a glovebox under a laminar flow) and a film was deposited, while the remaining substrates were held in the IPA solution. PEDOT:PSS was often mixed with DI water to create a thinner layer (thicknesses ranged from 20-40 nm). Solutions were always

filtered through a 0.45 μm PVDF filter before application. After deposition, the films were immediately placed on a hotplate heated to 150°C to prevent the PEDOT:PSS layer from absorbing moisture. Once all substrates were coated, the ITO/PEDOT:PSS substrates were transported to a N_2 filled glovebox and heated for a further 30-60 mins at 150°C (to ensure fully dried films) prior to the deposition of the active layer.

To fabricate a metal oxide buffer layer, all substrates were dried and placed inside a N_2 glovebox. They were then loaded into an evaporation mask, placed into a vacuum chamber and pumped down to ~ 10^{-7} mbar. The required metal oxide was then thermally evaporated while the substrates were rotated to allow a uniform deposition across the entire surface. A deposition rate of < 0.5Å/s was used to create a film free of voids. After the required film thickness was achieved (~ 10 nm), the substrates remained inside the chamber for a short time interval while the source and the substrates cooled. The chamber was then brought back to atmospheric pressure and the glass/ITO/metal oxide substrates were extracted. Note that the metal oxides used in Section 4.2 were deposited by Jonathan Griffin and were subjected to air exposure during transportation to the glovebox.

After the deposition of the anode buffer layer, the active layer was applied via spin-coating. The thickness of this layer was maintained between 40 and 100 nm. The ITO contact was cleaned free of any semiconductor material with IPA; a step crucial for efficient electrical contact for the cathode. This

was achieved by cleaning the top ITO contact in substrate style 1, or the left and right edges of the substrate for substrate style 2.

Cathode deposition was achieved via the same technique described above for the metal oxide buffer layers. An evaporation mask was again used, although it differed in style to that used for the metal oxide (apparent from part (b) and (d) in Figure 3.2). The metals used were calcium (Ca), aluminium (Al) and silver (Ag). An evaporation rate of 0.5 Å/s was used for intermediate layers (thicknesses of ~ 10 nm), whereas a rate of 1.5 Å /s was utilised for the highly reflective cathodes (thickness of 80-100 nm). The overlap between the ITO and patterned cathode defined the active pixel which had an area of 1.5 x 3 mm^2 for substrate style 1 and 2 x 2 mm^2 for style 2. Once the cathode deposition was completed, devices were again cooled and then placed back inside the glovebox. Any subsequent thermal annealing treatment was performed at this stage by placing the substrates on a hotplate. Devices were then annealed for ~ 30 mins and then rapidly quenched to room temperature by placing them on a metallic surface held at ambient temperature.

The device preparation process described above is summarised in Figure 3.2.

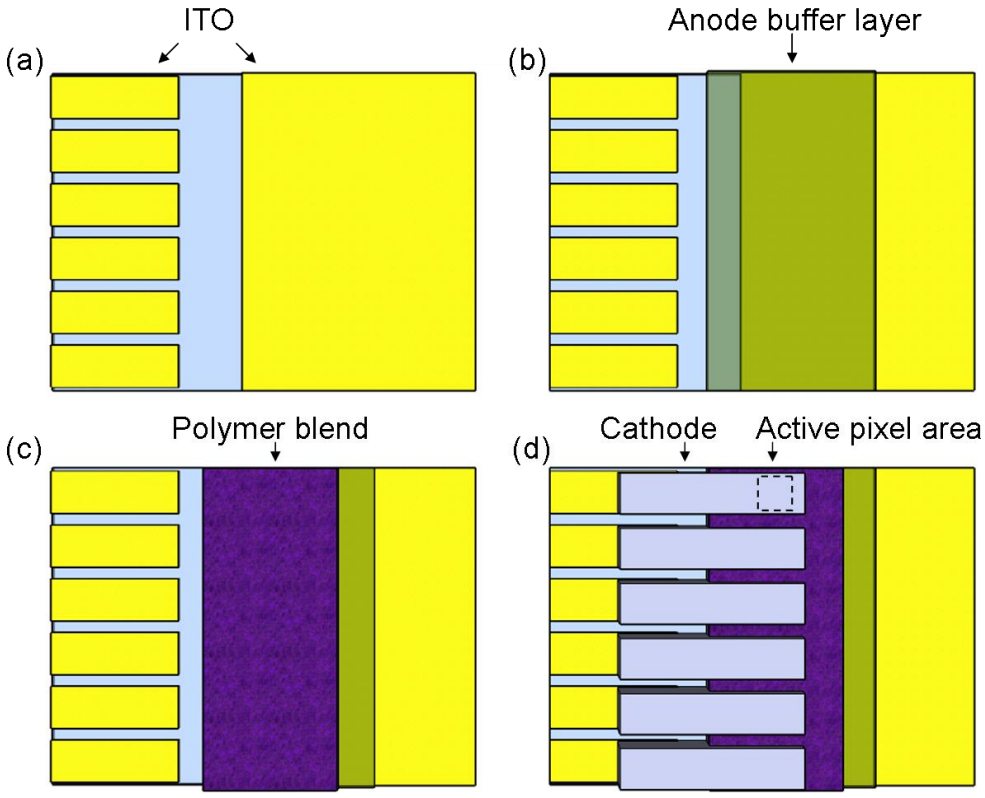

Figure 3.2 Summary of the device preparation process on substrate style 2. Part (a) depicts a cleaned glass/ITO substrate, while (b) displays the applied anode buffer layer such as PEDOT:PSS or a metal oxide. Part (c) shows the substrate with an active layer, and part (d) shows the fully completed device with a metal cathode.

An encapsulation step, prior to extraction from the glovebox was then used to improve the device stability by protecting the active layer from ambient conditions. This was achieved through the use of a UV epoxy and a glass slide. The devices were placed under a UV lamp for 30 mins to ensure a fully cured epoxy coating.

Device characterisation is achieved using a solar simulator. The layout of the solar simulator used (a Newport 92251A-1000) is shown in Figure 3.3. This had an output power of 100 mW/cm^2 with an AM1.5 spectrum, calibrated against a NREL certified silicon reference cell. A shadow mask was always used to create a highly defined pixel area. A Keithley 237 sourcemeter was used to record the J-V responses from devices under illumination from the solar simulator.

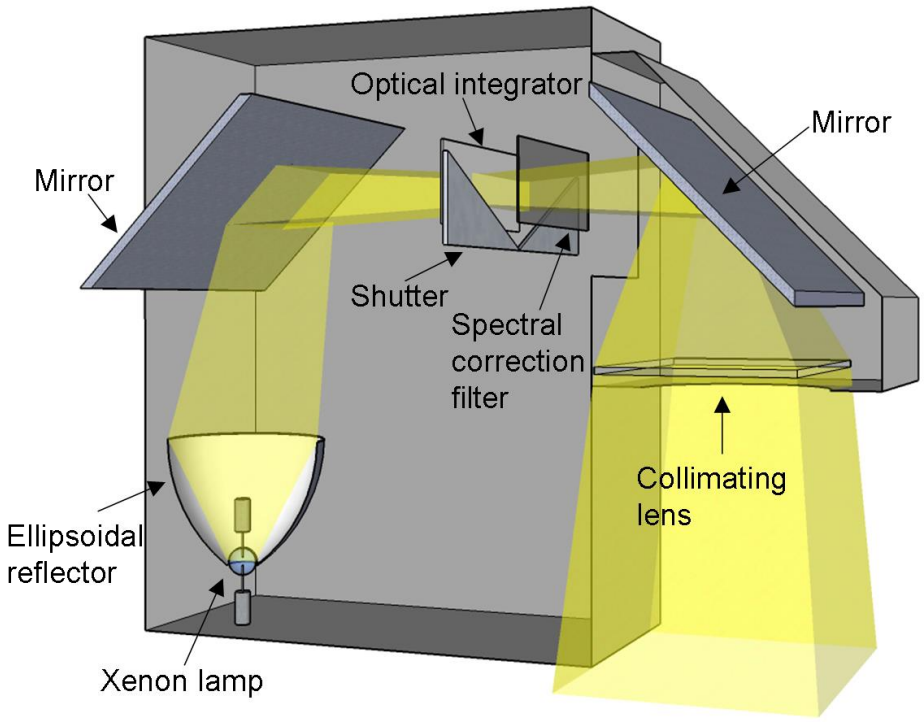

Figure 3.3 Layout of the solar simulator showing the light source as well as the filters used to obtain an AM1.5 output spectrum.

3.4 – UV-Vis spectroscopy

Absorption and photoluminescence characterisation was performed with a Horiba Fluoromax-4, spectrometer shown in Figure 3.4. A 150 W ozone-free Xenon arc lamp is used as the light source which is located in a separate housing. The excitation compartment is connected to the lamp housing by a quartz window. Two Czerny-Turner monochromators are used with the gratings possessing 1,200 grooves/mm, coated with MgF_2 (for protection against oxidation) that were used at a scan rate of 200 nm/s. The grating in the excitation (emission) compartment is blazed at 330 (500) nm. The slits in the excitation section are used to determine the bandpass of the light on the sample, whereas those in the emission compartment determine the intensity of the photoluminescence. A UV-enhanced silicon photodiode is used as a reference detector (to account for variations in the lamp output) and has a spectral response between 190 and 980 nm. Emission is detected using a photomultiplier tube capable of measuring light over the spectral range 180-850 nm.

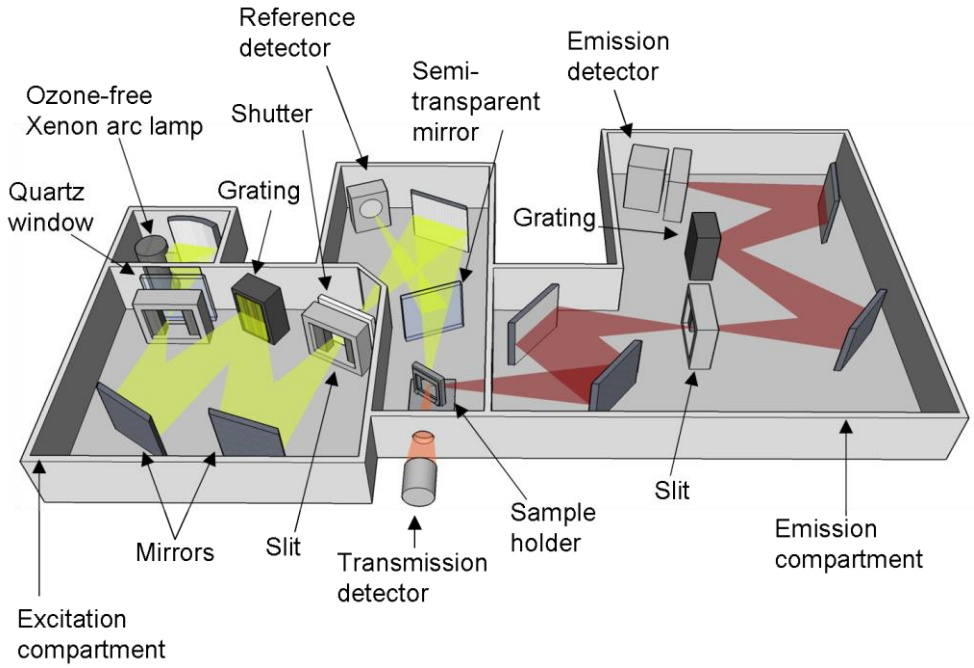

Figure 3.4 The setup of the UV-Vis spectrometer. The light source is housed in its separate section to prevent the heating of the optics. The excitation and emission compartments are located either side of the sample holder. A semi-transparent mirror allows the output of the Xenon light source to be monitored.

The absorption spectrum of the sample was achieved by measuring the wavelength of the light transmitted. Absorbance *A* (or optical density) is then calculated using Beer-Lambert's law:

$$A = -\log_{10}\left(\frac{I}{I_0}\right) \qquad \{3.3\}$$

where I (I_0) is the transmitted output of the sample (glass substrate). Thin film samples were measured from 350-900 nm in increments of 2 nm with a slit size of 2 nm.

PL spectra were achieved using the emission compartment of the spectrometer. To avoid direct reflection, the sample holder was held at an angle of 30° such that only emitted light from the sample was detected. Again, the output spectra were corrected for the reference spectrum.

3.5 – Photoluminescence quantum yield

The photoluminescence quantum yield (*PLQY*) was obtained using a frequency doubled Ti:Sapphire laser tuned to 400 nm with a neutral density filter to reduce the intensity. An Andor Shamrock 303 spectrometer and an Oriel iDus CCD detector, cooled to -40°C (to reduce thermal noise), with a slit size of 30 μm were used to acquire the data. Samples were placed inside an integrating sphere to average over all emission, therefore negating any angular orientation. As the polymers have relatively weak PL emission intensity, 1,000 accumulations were taken with an exposure time of 0.05 s. Dr David Coles assisted in data acquisition.

In order to determine the *PLQY* of a sample, several measurements were required. This included measuring the laser spectrum $L_0(\lambda)$ (before and after sample measurement to provide an average intensity) and the sample spectrum $S(\lambda)$, which also includes a remnant laser spectrum $L_1(\lambda)$. A calibration spectrum $C(\lambda)$ with a known radiometric spectrum $R(\lambda)$ used to account for wavelength-dependent bias from the apparatus was also required as well as a measurement for the self-absorption correction factor (obtained by comparing the photon flux of the sample outside and inside the integration sphere).

Analysis required correcting the sample and laser spectra by a sensitivity function, as determined by the calibration (*C(λ)* divided by *R(λ)*). Integrating the laser, sample and remnant laser spectra allowed their intensity to be calculated. The self-absorption correction was determined by normalising the spectra over a range where self-absorption was low and dividing the photon flux of the sample outside the sphere by that from the sample inside. The resultant *PLQY* value of the sample can then be calculated by:

$$PLQY = \frac{\text{number of emitted photons}}{\text{number of absorbed photons}} = \frac{I_S}{I_{L,0} - I_{L,1}} \qquad \{3.4\}$$

where I_S is the intensity from the sample (which is corrected for self-absorption), $I_{L,0}$ and $I_{L,1}$ are the laser and remnant laser intensity respectively.

3.6 – Atomic force microscopy

The surface properties of polymer:fullerene thin films were characterised using an atomic force microscope (AFM), with a simple view of the setup shown in Figure 3.5. Utilising the instruments tapping mode is key to eliminate shear forces which would otherwise scratch the sample's surface. Whilst in this mode, topography can be determined via changes in the oscillation amplitude of the cantilever. Simultaneously, phase imaging can be achieved by monitoring the differences in the phase of the oscillations relative to the driving signal. The phase signal determines the energy that is

locally dissipated in the film (dependent on the elasticity of the surface), and can be used to map the composition of the film.

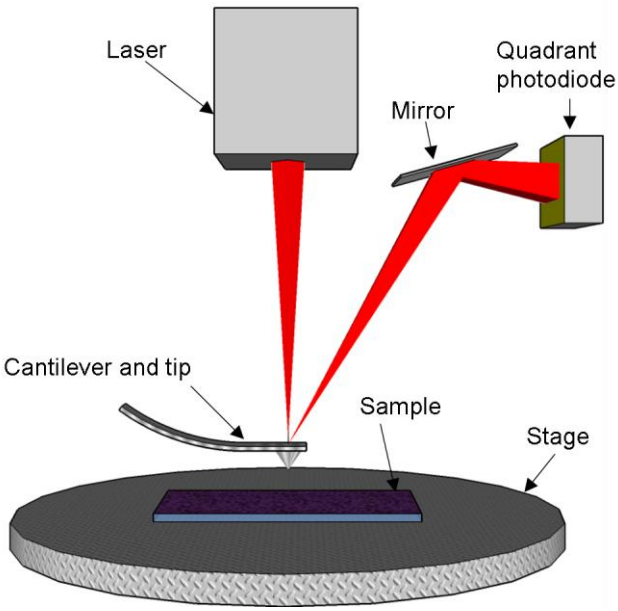

Figure 3.5 Setup of an AFM. The cantilever was a rotated monolithic silicon probe with a resonance frequency of 300 kHz and was attached to a piezoelectric component to enable smooth contact with the sample surface. Samples were fabricated in a glovebox where the solution was spun onto a glass slide.

3.7 – Grazing incident wide angle x-ray scattering

The ability to probe the molecular packing of thin films was achieved through the use of grazing incident wide angle x-ray scattering (GIWAXS). These experiments were performed at the Diamond Light Source, UK. The energy of the electrons from the synchrotron was selected (between 8 – 12 keV) via an optics lab in which further optics/filters were used to clean the beam (attenuating 2^{nd} order harmonics). The beam then interacted with the sample at an angle such that the scattered light could be detected. The

samples (pure polymer and polymer:fullerene thin films spin-cast on a silicon substrate) were loaded into a helium filled chamber to minimise unintended scattering from molecules in the ambient environment. The scattered beam was then characterised using a 2D Pilatus 2M detector. The process is shown schematically in Figure 3.6.

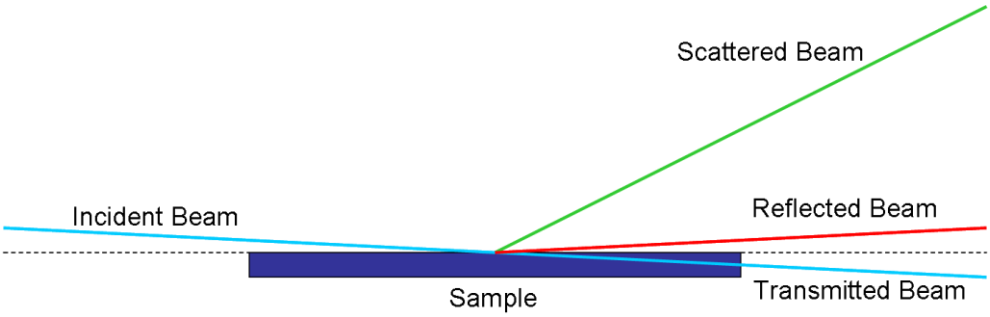

Figure 3.6 Schematic displaying the grazing incidence setup of GIWAXS with the various output beams. The reflected and transmitted beams were blocked by a beam stop.

The intensity and angle of light in the scattered beam can be used to determine internal molecular packing within the thin film. However, the transmitted and reflected beams can cause damage to the detector as they were of greater intensity than the scattered beam. A beam stop was therefore used to block the beam (typically made of lead) and was positioned between the sample and detector.

Coherent diffraction of the x-ray beam is described using Bragg's law:

$$2d \sin\theta = n\lambda \qquad \{3.5\}$$

where d is the distance between planes in a crystal lattice, θ is the grazing angle with respect to the lattice plane, n is the order of reflection (an integer) and λ is the wavelength of the x-ray. The resultant data measured by the detector is in reciprocal space (Q-spacing), which can be converted to real spacing by:

$$Q = \frac{2\pi}{d} = \frac{4\pi \sin\theta}{\lambda} \qquad \{3.6\}$$

In order to calibrate the scaling on the detector, a material with well defined Bragg peaks was used (Silver Behenate).

3.8 – Organic field effect transistors

Hole mobility of donor polymer systems was measured using organic field effect transistors (OFETs) that were fabricated and tested by Ossila Ltd. Figure 3.7 displays the architecture (bottom gate) used. A silicon substrate with a 300 nm silicon oxide (SiO_2) layer acted as the gate and insulator layers respectively. The gold source and drain contacts were then thermally evaporated onto the cleaned substrate with channel dimensions of 50 μm x 20 mm. A surface treatment of octadecyltrichlorosilane (OTS) was applied before the semiconductor layer was spin-cast in a N_2 filled glovebox. Devices were also analysed while they remained within the glovebox.

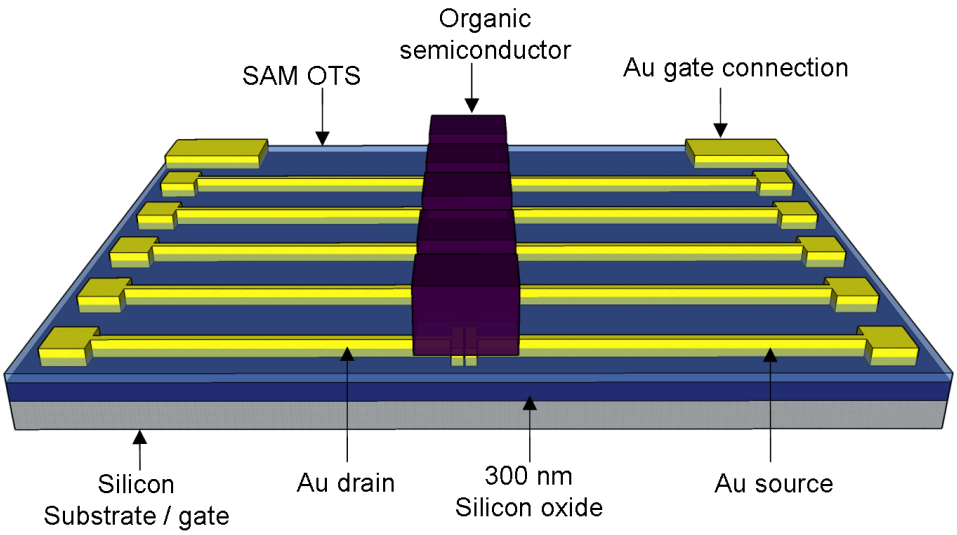

Figure 3.7 Schematic of an OFET device with a bottom gate architecture and a self-assembled monolayer (SAM) of OTS. Note that layer thickness is not to scale.

Transfer characteristics can be obtained for each polymer donor system by applying a constant drain voltage, V_D, while sweeping the gate voltage, V_G, and measuring the output source-drain current, I_{SD}. A threshold voltage, V_T, must be surpassed before a current flows through the device. The saturation regime is when $|V_D| \geq |V_G - V_T|$. In this regime, the source-drain current can be expressed as:

$$I_{SD} = \frac{WC_i\mu}{2L}(V_G - V_T)^2 \qquad \{3.7\}$$

where W (L) is the source drain channel width (length), C_i is the capacitance per unit area of the insulator layer and μ is the charge carrier mobility. Using values of W, L and C_i (20 mm, 50 μm and 1.08 x 10^{-8} Fcm^{-2} respectively, for

a SiO_2/OTS layer), equation 3.7 may be expressed in terms of the carrier mobility, namely:

$$\mu = \frac{2L}{WC_i} \frac{\partial(I_{SD}{}^{1/2})}{\partial V_G} \qquad \{3.8\}$$

where the gradient $\frac{\partial(I_{SD}{}^{1/2})}{\partial V_G}$ is taken above V_T. Figure 3.8 shows a typical saturated transfer characteristic with the threshold voltage and mobility displayed.

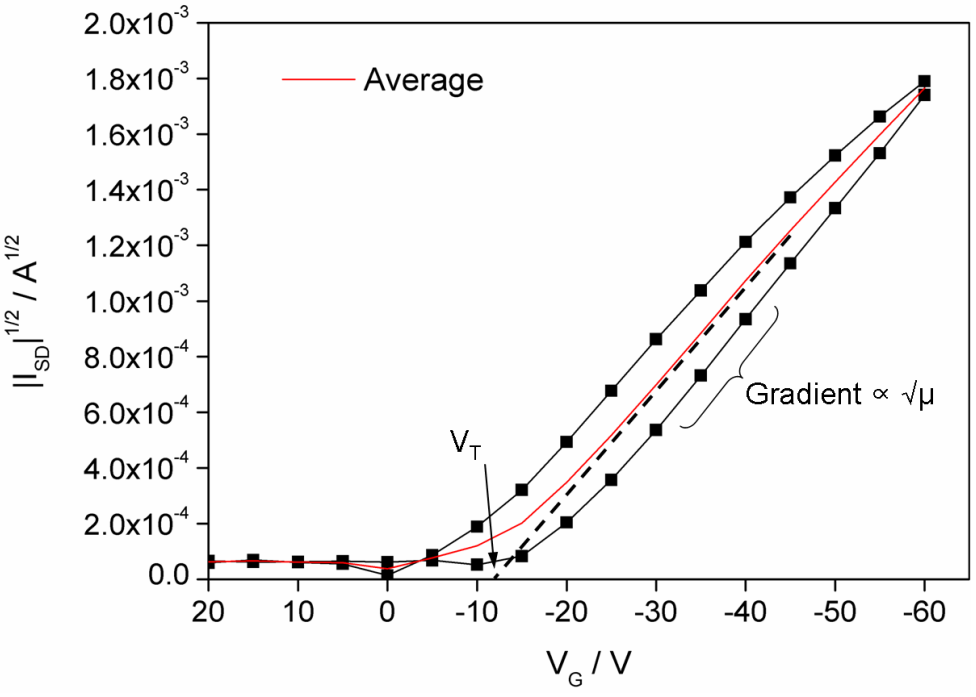

Figure 3.8 Saturated transfer characteristic example showing the average of two sweeps and the threshold voltage V_T.

3.9 – Spectroscopic ellipsometry

Spectroscopic ellipsometry (SE) is an optical technique which allows the optical constants of a film to be calculated, specifically the refractive index (n) and the extinction coefficient (k). Both of these values are of importance for use with the transfer matrix reflectivity model, discussed below in Section 3.10. SE utilises polarised light which changes upon reflection from the sample. This change provides a means to determine the various parameters required from the experiment. Here, a J.A. Woollam M-2000V ellipsometer with a wavelength range of 370 – 1,000 nm was used. Data was acquired by Dr. Tao Wang.

The technique involves characterising the amplitude of the light polarised parallel (R_p) and perpendicular (R_s) to the plane of incidence. Taking the ratio of these parameters gives the reflectance ratio:

$$\rho = \frac{R_s}{R_p} = \tan\psi \exp(i\Delta) \qquad \{3.9\}$$

where ψ is the ratio of amplitudes and Δ is the phase difference on reflection. Using the parameters ψ and Δ, the optical constants of the film may be calculated by reference to an optical model. This is achieved by utilising a Cauchy dispersion model to approximate the thickness of the film, where the real part of the refractive index (n) is estimated using:

$$n = A + \frac{B}{\lambda^2} + \frac{C}{\lambda^4} + ... \qquad \{3.10\}$$

with *A*, *B* and *C* being positive constants. This model however needs to be applied at a wavelength region where the material is non-absorptive, i.e. below the energy gap of an organic semiconductor. Finally, with the thickness of the sample determined, the refractive index and the extinction coefficient may be extracted by using a B-spline model incorporating a Kramers-Kronig model [1,2].

In order to extract the glass transition temperature (T_g) of a polymer, the sample was subjected to a variety of temperatures. The changes in ψ can then be plotted against temperature to determine the rate of film expansion. Polymers with a higher degree of packing (as observed from GIWAXS) will require higher temperatures to enable the molecules to become more mobile, thus resulting in a higher T_g. Note that this technique was utilised to determine the T_g of the polymers (rather than differential scanning calorimetry, DSC) as ultrathin films, < 100nm, were investigated. In this scenario, confinement (i.e. where physical properties are not necessarily a bulk property) was important.

3.10 – Transfer matrix reflectivity model

A transfer matrix reflectivity model (freely downloadable and described in refs [3,4]) was used to determine the various effects from replacing the metal cathode in a device (see Chapter 4). The model uses optical properties (namely the n/k data as obtained from SE) of the various materials used within each layer of the device to predict the maximum proportion of the solar spectrum to be harvested. The model however does not predict any

electrical properties, instead concentration on providing useful information for the optical improvements of devices. As OPV devices have layers in the nanometre range, the interference of light propagating through the device plays an important role in determining optical absorption efficiency. This is taken into account in the model and the thickness of each layer is selected at the start of its calculations.

By calculating the transmission and reflection at each interface, the electromagnetic (EM) field distribution throughout each layer can be determined. In order to achieve this, the model relies on a number of matrices that describe each interface of the structure (I_{jk}), the propagation through each layer (L_j) and the electric field within the structure (by relating the electric field in air with that in the final layer of the device, S). They are defined as:

$$I_{jk} = \frac{1}{t_{jk}} \begin{bmatrix} 1 & r_{jk} \\ r_{jk} & 1 \end{bmatrix} \qquad \{3.11\}$$

$$L_j = \begin{bmatrix} \exp\left(-i\xi_j d_j\right) & 0 \\ 0 & \exp\left(i\xi_j d_j\right) \end{bmatrix} \qquad \{3.12\}$$

$$S = \begin{bmatrix} S_{11} & S_{12} \\ S_{21} & S_{22} \end{bmatrix} = \left(\prod_{\upsilon=1}^{m} I_{(\upsilon-1)\upsilon} L_\upsilon \right) I_{m(m+1)} \qquad \{3.13\}$$

where t_{jk} and r_{jk} are the Fresnel complex transmission and reflection coefficients respectively at interface jk, ξ_j is the phase of layer j, d_j is the thickness of the layer and m is the number of layers in the device. By separating S into two subsets separated by layer j, i.e. $S = S_j^{'} L_j S_j^{''}$, the total internal electric field may be calculated:

$$E_j(x) = T \frac{S_{j11}^{''} e^{-i\xi_j(d_j - x)} + S_{j21}^{''} e^{i\xi_j(d_j - x)}}{S_{j11}^{'} S_{j11}^{''} e^{-i\xi_j d_j} + S_{j12}^{'} S_{j21}^{''} e^{i\xi_j d_j}} \qquad \{3.14\}$$

where T is the transmitted field from the substrate and x is a distance to the right of the boundary.

The maximum photocurrent, J_{max}, of the device can be calculated by:

$$J_{\max} = \int_{\lambda_1}^{\lambda_2} \frac{eA(\lambda)I(\lambda)}{hc} \lambda d\lambda \qquad \{3.15\}$$

where e is the elementary charge, $A(\lambda)$ is the wavelength-dependent absorption of the active layer (calculated in the model), $I(\lambda)$ is the AM1.5 solar spectrum, h is Planck's constant and c is the speed of light.

There are however limitations to the model. A key assumption is that the active layer has an IQE (internal quantum efficiency) that characterises how many electrons are extracted from the device per absorbed photon of 100% for all wavelengths. It also assumes each layer in the device is homogenous

and isotropic, and that interfaces are smooth. The model does not account for diffuse scattering or spatially dependent optical constants.

3.11 – Ultraviolet photoelectron spectroscopy

The deposition of metal oxide buffer layers was discussed previously in Section 3.3. To determine the work function of the various metal oxide buffer layers, ultraviolet photoelectron spectroscopy (UPS) was used to probe the binding energy of the electrons within the film. A schematic of the setup is displayed in Figure 3.9. A He (1) photon source is used with a photon energy of 21.22 eV.

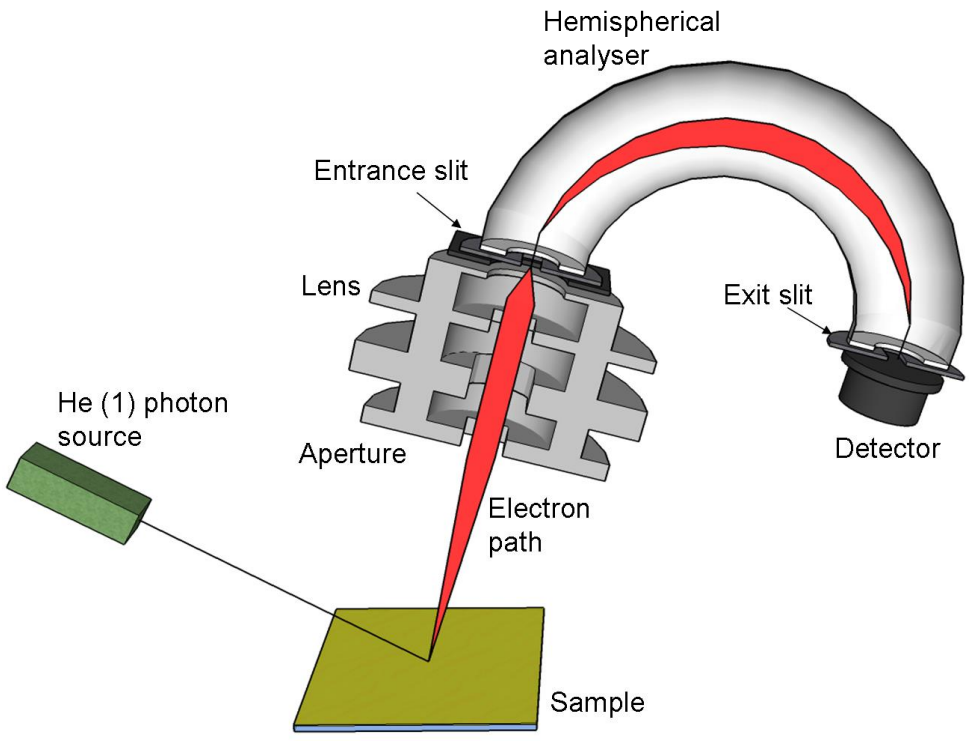

Figure 3.9 Layout of the UPS experiment. The metal oxide samples were prepared by thermal evaporation onto glass/ITO substrates at a thickness of ~ 10 nm.

The experiment utilises the photoelectric phenomenon described by equation 3.16 and relates the kinetic energy of an ejected electron (E_K) to its binding energy (E_B) and the energy of the incident photon (E_P). E_P is governed by the photon source, E_K is the energy possessed by the ejected electron, while E_B is dependent on the energy level populated by the electron.

$$E_K = E_P - E_B \qquad \{3.16\}$$

The valence energy levels and the work function may be extracted once the kinetic energy of the ejected electron has been determined. The ejected electron will possess a kinetic energy E_k of:

$$E_k = \frac{1}{2} m_e v^2 \qquad \{3.17\}$$

where m_e is the electron mass and v is its velocity. In the UPS experiment, the electron travels through a hemispherical analyser of known radius with an applied external magnetic field perpendicular to the analyser. The force may then be described by both the centripetal and the Lorentz force, respectively:

$$\underline{F} = \frac{m_e \underline{v}^2}{r} \qquad \{3.18\}$$

$$\underline{F} = e(\underline{v} \times \underline{B}) \qquad \{3.19\}$$

where r is the radius of the analyser, e is the elementary charge and $\underline{B}$ is the applied magnetic field. Equating these expressions allows the velocity of the electron to be obtained. Inputting this velocity into equation 3.17 permits kinetic energy to be expressed using:

$$E_k = \frac{(erB)^2}{2m_e} \qquad \{3.20\}$$

By varying the value of the magnetic field it is possible to determine a population spectrum. The work function and the valence band of the sample may then be extracted. An example of a molybdenum oxide (MoO_x) UPS spectrum is displayed in Figure 3.10 with the secondary electron cut-off (which determines the work function of the material), the valence/HOMO energy level and the location of defect states indicated.

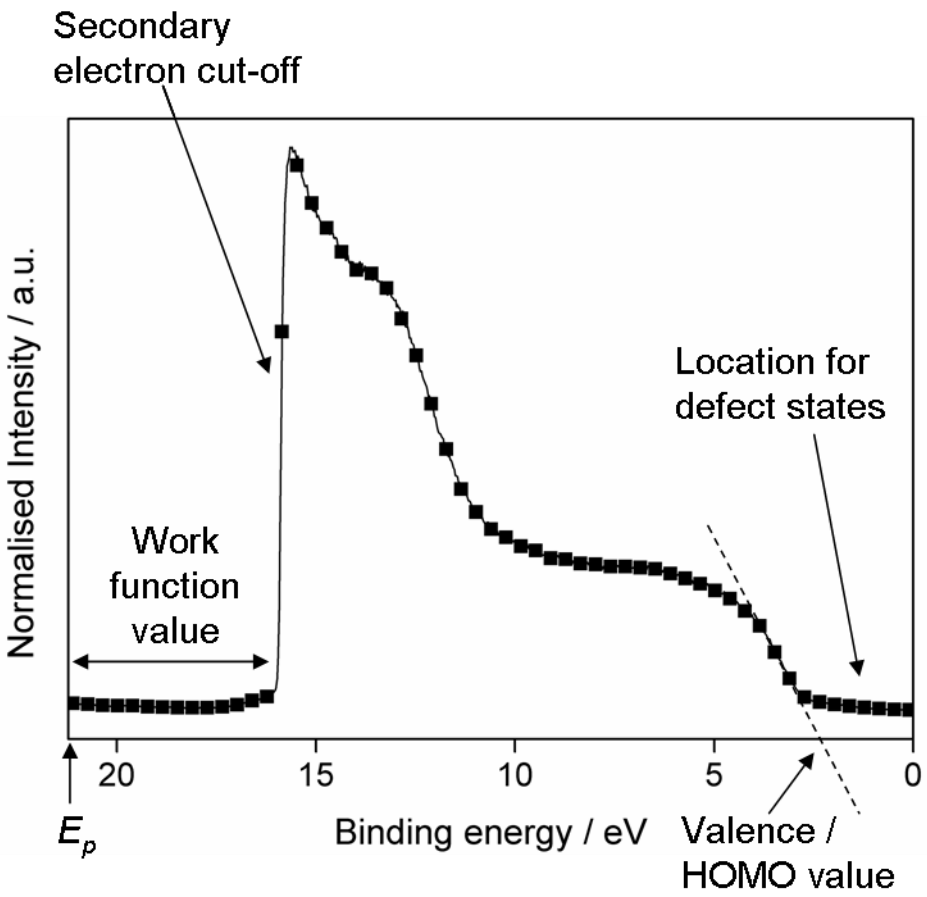

Figure 3.10 An example of an UPS spectrum with the location of the secondary electron cut-off, defect states and valence/HOMO energy level value indicated. Sample preparation and data taken by Jonathan Griffin.

3.12 – Cyclic voltammetry

In order to determine the HOMO and LUMO energy levels of a polymer, cyclic voltammetry (CV) was employed. The electrochemical cell of the equipment is shown in Figure 3.11. Here, the polymer was deposited on the top of the platinum working electrode by drop casting from a $CHCl_3$ solution at a concentration of 1 mg/ml. A Ag/Ag^+ reference electrode was used along with a platinum foil counter electrode. The three electrodes were

connected to a Princeton Applied Research Model 236A Potentiostat/Galvanostat.

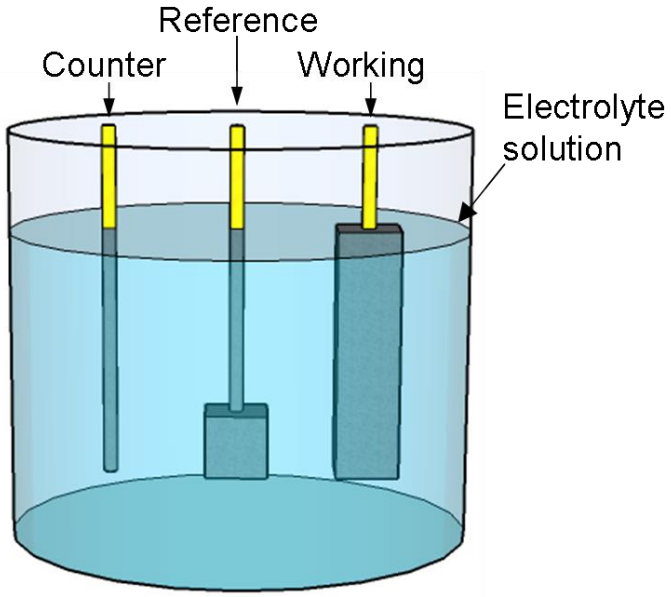

Figure 3.11 Schematic of the electrochemical cell of the CV equipment with the counter (platinum foil), reference (Ag/Ag^+) and working (platinum) electrodes highlighted. The electrodes were connected to a potentiostat and a current-voltage converter. The electrolyte solution was made from a tetrabutylammonium hexafluorophosphate solution in acetonitrile.

During the measurements, a potential was applied to the working and reference electrodes. The current response between the working and counter electrodes provided an insight into the energy levels of the polymer via an IV curve. From the curve, the oxidation and redox potentials of the polymer (corresponding to the energy required to extract/inject an electron from/to the polymer, respectively) may be determined. These values were measured against the Ag/Ag^+ reference electrode. Note it was taken that ferrocene/ferrocenium is 4.8 eV below the vacuum level.

It should also be noted that throughout this thesis, the presented HOMO and LUMO energy levels of the polymers are taken to be synonymous with the ionisation potential and the electron affinity respectively.

3.13 – Gel permeation chromatography

The presented polymer number-average and weight-average molecular weights (M_n and M_w respectively) were determined via gel permeation chromatography (GPC). The setup used is shown in Figure 3.12. The synthesised polymer was introduced to the top of the column, which contained a silica gel, shown in part (a).

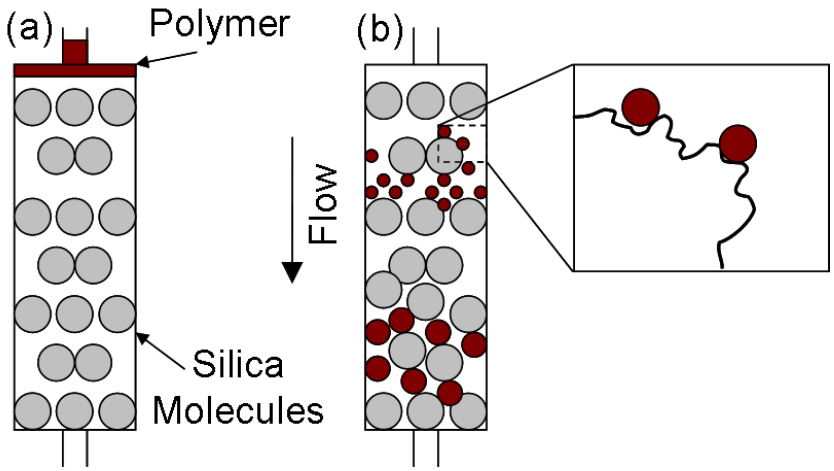

Figure 3.12 (a) GPC setup when the polymer is introduced to the column. (b) If the size of the polymer chain is large enough, the chain traverses through the column with little interactions with the silica molecules. However, smaller chains may be influenced consequently allowing a time discrepancy between the various polymer chain lengths.

The length of the polymer chain determines the time it spends within the column, with the smaller chains interacting more with the silica gel which act to increase its path, Figure 3.12(b). Once the polymer chain reaches the bottom of the column, a refractive index detector records the GPC curve, allowing the M_n and M_w distributions of the polymer to be determined. The detector was calibrated using a series of polystyrene narrow standards.

References

1. T. Wang, A.J. Pearson, D.G. Lidzey, R.A.L. Jones, Evolution of structure, optoelectronic properties, and device performance of polythiophene:fullerene solar cells during thermal annealing, *Adv. Funct. Mater.*, **2011**, *21*, 1383-1390
2. B. Johs, J.S. Hale, Dielectric function representation by B-splines, *Phys. Status Solidi A*, **2008**, *205*, 715
3. L.A.A. Pettersson, L.S. Roman, O. Inganäs, Modeling photocurrent action spectra of photovoltaic devices based on organic thin films, *J. Appl. Phys.*, **1999**, *86*, 487
4. G.F. Burkhard, E.T. Hoke, M.D. McGehee, Accounting for interference, scattering, and electrode absorption to make accurate internal quantum efficiency measurements in organic and other thin solar cells, *Adv. Mater.*, **2010**, *22*, 3293-3297

Chapter 4

Optimising the anode buffer layer and cathode for PCDTBT-based organic photovoltaic devices

In this chapter, an introduction to the low bandgap polymer PCDTBT will be presented and this will form the chemical structure basis for the novel polymers discussed in the following chapters. Optimisation of PCDTBT devices in this chapter will be primarily focussed around the buffer layer used at the ITO anode interface and the choice of cathode metals used in a conventional OPV device. The replacement of a PEDOT:PSS anode buffer layer with thermally evaporated metal oxides (MoO_x, V_2O_5 and WO_{3-x}) will be investigated, as well as simple stability comparisons for MoO_x and V_2O_5 devices. The final section of this chapter will address the use of a transfer matrix reflectivity model to determine the electric field distribution in a device for a variety of metal cathode materials (aluminium, silver and calcium) as well as a composite cathode that consists of a thin calcium layer capped by a highly reflective layer of either aluminium or silver. Such modelling results are compared with measurements made on OPV devices to determine an optimised fabrication protocol.

4.1 – Introduction

The introduction of PCDTBT into the OPV community in 2007 saw initial efficiencies of 3.6% realised [1]. Over the following years, such device performance was increased to 5.7% through the use of the cathode buffer layer lithium fluoride (LiF) [2]. An alternative approach was then explored by utilising the metal oxide optical spacer titanium oxide (TiO_x) where a maximum PCE of 6.1% was obtained [3]. The formation of a TiO_x layer uses a sol-gel process on top of the active layer and also requires a thermal annealing step which could consequently affect device morphology.

Although this process is not detrimental for PCDTBT (such a low-temperature annealing step merely extracts trapped solvent within the active layer with minimal effects on the phase separation [4]), its application to various other polymer donor components can result in degradation in device performance due to non-ideal modification to active layer morphology.

Further advances in device efficiency then came from the inclusion of silver nanoparticles within the active layer which act as a source for enhanced light absorption [5]. Through the use of this technique, device efficiencies of 7% were realised. Similar performance was also obtained through the replacement of the PEDOT:PSS anode buffer layer with the metal oxide molybdenum oxide (MoO_x), along with an anti-reflection coating [6]. The work function of MoO_x was measured to be closer to the HOMO energy level of PCDTBT than PEDOT:PSS leading to a smaller energy offset. This resulted in improved FF values for nominally identical devices. Other metal oxides (such as vanadium V_2O_5 and tungsten oxide WO_3) have also been shown to provide efficient OPV devices [7-10].

As mentioned previously, a smaller energy offset between the work function of the anode buffer layer and the donor material HOMO energy level can improve device efficiency. The use of a PEDOT:PSS permitted efficient charge extraction from polymer systems possessing a relatively low HOMO energy level (~ 5 eV). However, new donor polymers have been designed with deeper HOMO levels, with such values below the oxidation threshold

(approx. -5.27 eV [11]), to increase the polymer stability (for example PCDTBT). Furthermore, thin films of PEDOT:PSS exhibit an affinity to absorb oxygen [12] and water which can cause degradation to the ITO anode [13] as well as allow the migration of moisture to the active layer/cathode buffer layer interface [14]. Both effects are detrimental to device stability, with more significant consequences in devices with either insufficient or damaged encapsulation.

A variety of low bandgap polymers (such as the PBDTTT [15-17] and PTB family [18-19]) have obtained higher device efficiencies despite the use of a PEDOT:PSS layer. Here, the cathode buffer layer was replaced by a composite cathode consisting of a thin calcium layer (~ 20 nm) backed by a thick, opaque layer of aluminium (80-100 nm). Although calcium (like LiF and TiO_x) also presents complications within devices (such as oxidation or contamination), the latter part of this chapter will focus on the advantages associated with such an intermediate layer of calcium (namely its moderately good reflectivity and high charge extraction efficiency) compared with alternative metal cathode materials. In order to achieve this comparison of various possible cathode metals, a transfer matrix reflectivity model will be used. The model allows the electric field distribution to be determined for a variety of wavelengths as well as computing the maximum photocurrent (J_{max}) for a given polymer system. Section 3.10 provides details regarding the model input requirements, assumptions and analysis.

4.2 – Utilising metal oxides at the anode buffer layer

PCDTBT (chemical structure shown in Figure 4.1) has a HOMO energy level of -5.35 eV (as determined by CV and UPS), which is ~ 0.3 eV below the work function of PEDOT:PSS. To determine the effectiveness of alternative materials as the anode buffer layer, OPV devices were constructed (as detailed in Section 3.2 and 3.3) to characterise the difference in both the FF (extraction efficiencies) as well as the V_{oc} (energy level alignment). Table 4.1 presents the device metrics for various anode buffer layers. Note that all devices used a composite cathode of Ca/Al and were thermally annealed at 80°C (unless specified otherwise) after cathode deposition. Section 4.3 details the improvements in device performance and electric field distribution achieved from utilising such a cathode structure.

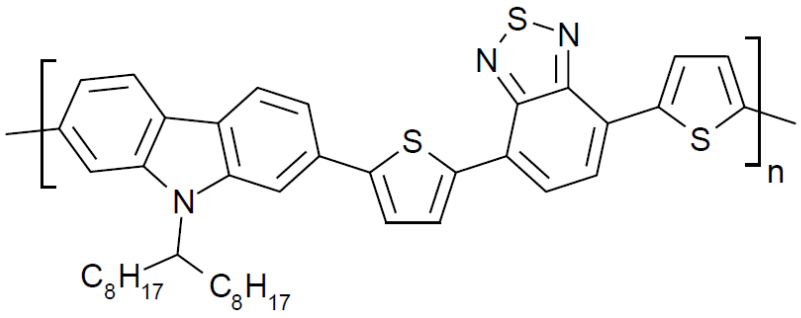

Figure 4.1 Chemical structure of PCDTBT.

Anode buffer layer	Solvent	Thickness / nm	J_{sc} / $mAcm^{-2}$	V_{oc} / V	FF / %	PCE / %
PEDOT:PSS	DCB	50	-7.82	0.58	50.80	2.30
	CB	65	-10.85	0.78	46.39	3.93
	$CHCl_3$	65	-10.26	0.82	57.80	4.86
MoO_x	$CHCl_3$	65	-8.84	0.86	63.90	4.86
	CB	70	-9.91	0.89	62.64	5.53[a)]
V_2O_5	CB	70	-9.39	0.87	64.55	5.30[a)]
WO_{3-x}	CB	70	-0.12	0.43	18.52	0.01[a)]

Table 4.1 Optimised device metrics for various anode buffer layers. Device architecture was ITO/Anode buffer layer/PCDTBT:$PC_{70}BM$/Ca/Al (blend ratio of 1:4). All devices were thermally annealed at 80°C after the deposition of the cathode, except metal oxide devices marked with [a)].

Despite the PCDTBT:$PC_{70}BM$ blend performing best when cast from a $CHCl_3$ solvent when used with a PEDOT:PSS anode buffer layer (with PCEs approaching 5%), thin films cast from CB allowed superior efficiencies to be acquired when a metal oxide buffer layer was used. The J-V characteristics of the best performing pixels for each anode buffer layer are shown in Figure 4.2. The key difference between these devices is that a greater J_{sc} is obtained when PEDOT:PSS is used, however the V_{oc} and FF are larger for the metal oxides (MoO_x and V_2O_5) leading to enhanced performance.

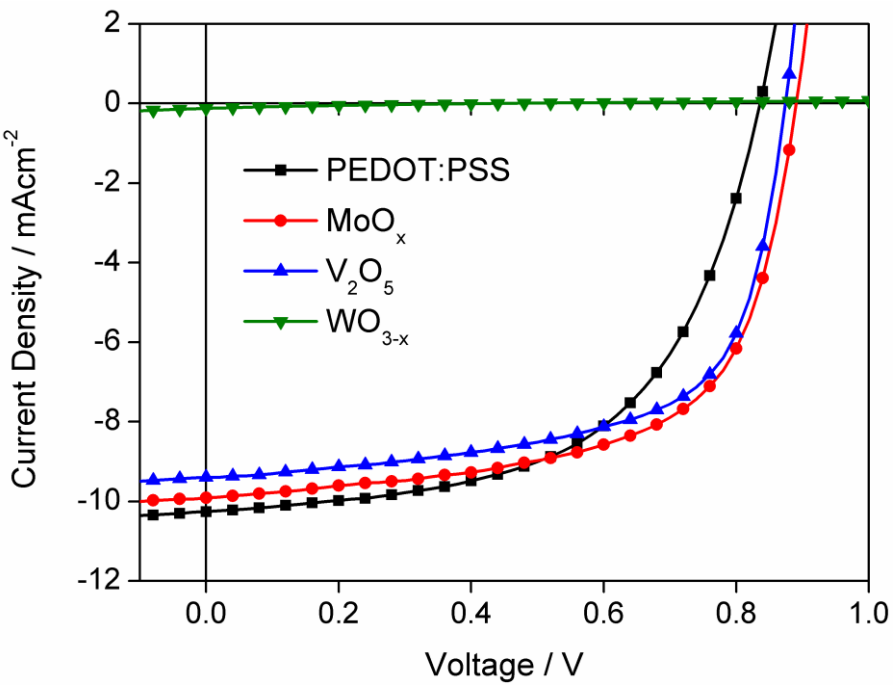

Figure 4.2 J-V characteristics of the best pixels for the anode buffer layers PEDOT:PSS and the metal oxides: MoO_x, V_2O_5 and WO_{3-x}. Note that the PEDOT:PSS based device was fabricated and tested by staff at Ossila Ltd.

UPS (ultraviolet photoelectron spectroscopy) results suggest that both the MoO_x and the V_2O_5 layer have a work function of -5.4 eV (see Figure 4.3), a value much closer to the HOMO energy level of PCDTBT than PEDOT:PSS, hence larger V_{oc} and FF values are observed. The smaller values of J_{sc} are most likely due to greater absorption within the metal oxide layers compared with PEDOT:PSS.

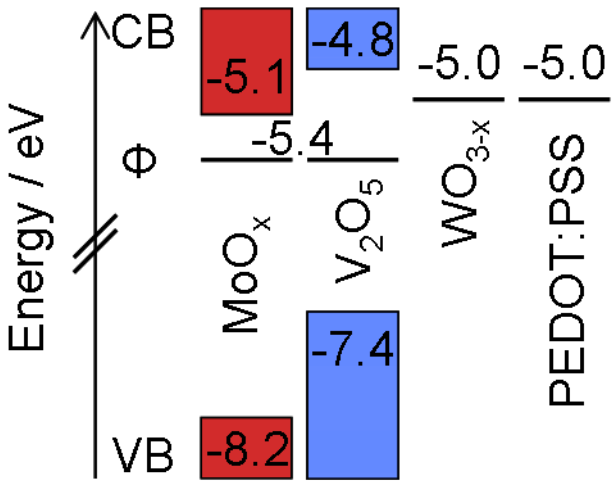

Figure 4.3 Band diagram of the investigated metal oxides and PEDOT:PSS. CB (VB) corresponds to the conduction (valence) band and Φ is the work function. Values of the metal oxide films were determined via UPS.

Devices based on a WO_{3-x} buffer layer however were characterised by very poor performance. This was due to the presence of metallic (or defect) states in the metal oxide layer, as observed from UPS (see Figure 4.4 inset). A similar result was observed on varying the stoicheometry (changing the amount of metallic to oxide states within the resultant film) in sputtered MoO_x films [20]. Here, films containing a large amount of metallic states resulted in a work function of -4.5 eV, consequently leading to large energy offset with the PCDTBT HOMO level and hence poor device performance. It was shown that as the oxidation states of MoO_x increased (achieved by altering the oxygen content during deposition), the occupied metallic states disappeared and the work function deepened to -5.3 eV which allowed efficient devices to be realised. For WO_{3-x}, it is likely that the large amount of metallic states within the layer prevented it acting as an efficient hole extraction layer.

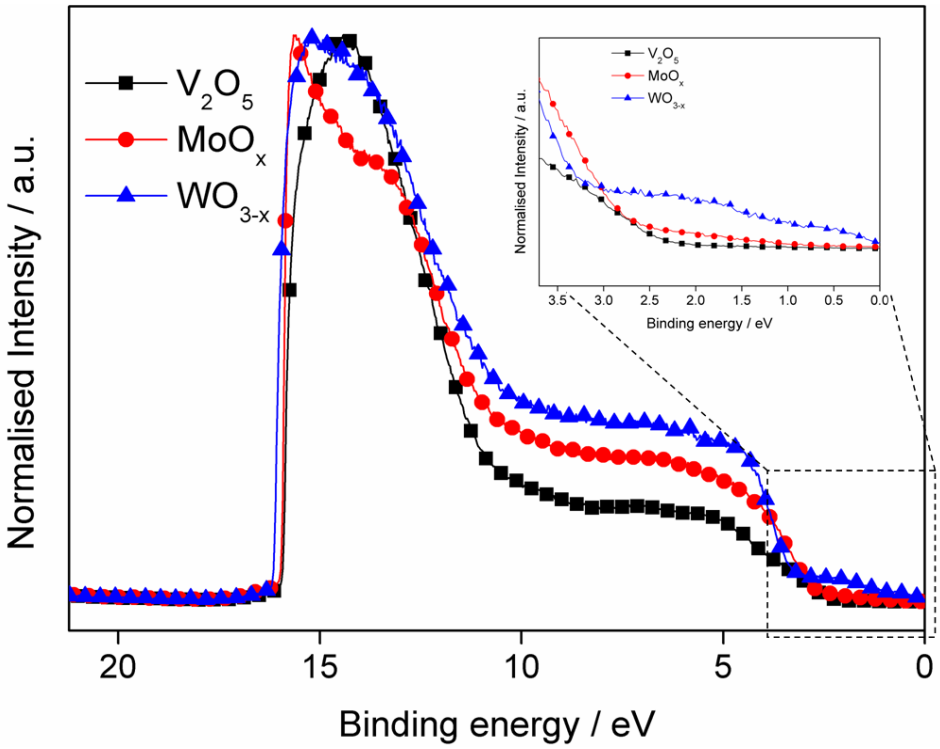

Figure 4.4 Normalised UPS spectra of thermally evaporated MoO_x, V_2O_5 and WO_{3-x} thin films. Inset is a close view of the defect states in WO_{3-x}. Device preparation as well as data acquisition performed by Jonathan Griffin.

Simple device stability tests (devices stored in ambient conditions in the dark, measured ~ 1 month apart) for devices utilising a MoO_x or V_2O_5 hole buffer layer were recorded over a 2 month period. The average PCE, taken for the top 50% of 18 pixels, remained fairly constant after the 60 day study. A small increase in PCE was observed for both metal oxide layers after 40 days resulting from a general improvement in both the J_{sc} and V_{oc}, while the FF remained relatively constant. This could be due to changes at the interface between the buffer layer and active layer. After 60 days, the average PCE for MoO_x devices degraded by ~ 2.7% from their initial values (a value still within experimental uncertainty levels), however the average

PCE for V_2O_5 displayed minimal losses. Although these were only initial tests on the dark lifetime of devices, both metal oxides underwent only minor degradation; a feature likely to be of benefit in PCDTBT-based OPV devices.

4.3 – Cathode materials

Figure 4.5(a) shows the modelled value of J_{max} (as determined using Equation 3.15 from Section 3.10) for a PCDTBT:$PC_{70}BM$ OPV using an Ag cathode and a 10 nm thick MoO_x anode buffer layer as a function of the thickness of the active layer. It can be seen that there are two maxima in the predicted photocurrent response that occur for PCDTBT:$PC_{70}BM$ layer thicknesses of ~ 70 nm and ~ 200 nm. These resonances result from optical interference effects within the device, as have been previously demonstrated in OPVs [10, 21, 22]. The predicted maximum photocurrent for the 200 nm thick PCDTBT:$PC_{70}BM$ layer is -15 $mAcm^{-2}$; a value larger than that predicted for a thickness of 70 nm (-11.9 $mAcm^{-2}$). The larger value of J_{max} anticipated in devices with thicker active layers results directly from the improved optical absorption that occurs in more optically dense films. It is clear however that these values most probably over-estimate photocurrent yield as the calculation does not include sub-optimal charge extraction efficiency. As a result of relatively low hole carrier mobility in amorphous polymers such as PCDTBT (discussed in further detail in Chapters 5 and 6), efficient charge extraction will be particularly problematic in devices utilising a 200 nm thick PCDTBT:$PC_{70}BM$ film [23]. Indeed, recent spectroscopic studies have indicated that non-geminate recombination and

thus incomplete charge-extraction is a dominant loss mechanism in PCDTBT:PCBM OPVs [24]. Furthermore, practical difficulties also arise in producing such thick active layers resulting from the relatively low solubility of PCDTBT (a condition addressed in the synthesis of polymers discussed in Chapter 5). As such, the remainder of this section focuses on active layer thicknesses that are less than 100 nm.

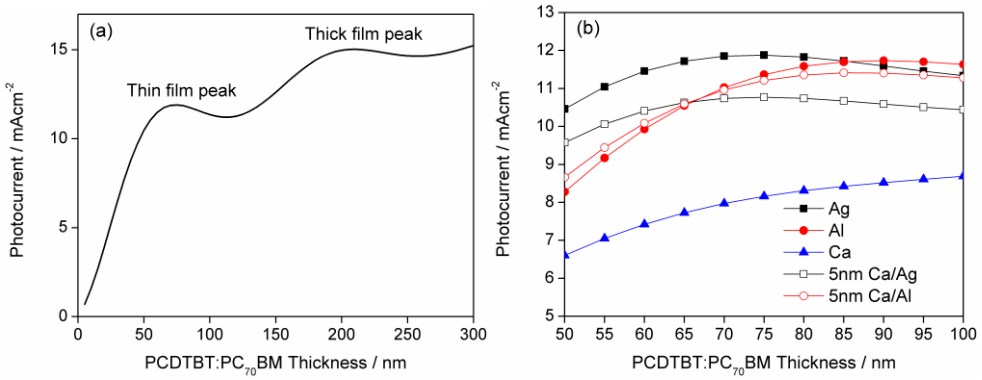

Figure 4.5 Modelled photocurrent for (a) an active layer thickness ranging from 0-300 nm with a reflective Ag cathode, displaying the "thin" and "thick" interference peaks. Part (b) displays a closer view of the thin film peak for a variety of metal cathode materials.

In Figure 4.5(b), the calculated value of J_{max} from PCDTBT:PC_{70}BM OPV devices utilising either an Ag, Al, Ca, Ca/Ag or Ca/Al cathode as a function of active layer film thickness is plotted. The MoO_x film thickness is again fixed at 10 nm. It can be seen that J_{max} is predicted to be a strong function of cathode composition, with high-reflectivity Ag producing devices with the highest overall photocurrent for a PCDTBT:PC_{70}BM film thickness less than 85 nm. For active layer thicknesses greater than 85 nm, a larger photocurrent is predicted from an OPV utilising an Al cathode. It is clear

that a calcium cathode results in the lowest predicted photocurrent due to its lower reflectivity and greater optical loss. The photocurrent from a series of composite cathodes (a 5 nm Ca interface layer backed by opaque Ag or Al) is also plotted. It can be seen that the incorporation of a thin Ca film appears to have a more significant effect on the photocurrent generated by an Ag cathode compared to an Al cathode. Indeed, the maximum predicted photocurrent that can be generated using a Ca/Ag cathode is around 90% of that which can be generated using a Ag cathode, whereas the maximum photocurrent that can be generated using a Ca/Al cathode is ~98% of a regular Al cathode. The reasons for the larger predicted reduction in maximum photocurrent that can be generated using a Ca/Ag layer will be explored later in this section.

The analysis presented in Figure 4.5 confirms that the optical properties of the cathode play an important role in determining the maximum available photocurrent yield from OPVs containing a relatively thin active organic semiconductor layer. However, this analysis ignores the effect of the metal work-function on extraction or effects resulting from recombination at an interface, with such effects known to be particularly problematic in OPVs utilising silver, gold or palladium cathodes [25]. The metal Ca is known to efficiently extract electrons in BHJ OPVs utilising fullerene acceptors [26], however the analysis presented in Figure 4.5 confirms previous studies [26,27] that indicate that it can reduce device efficiency through increased absorption losses into the device. Therefore, the maximum available photocurrent available from an OPV utilising a film of Ca backed by an

optically thick layer of either Ag or Al is explored. This is shown in Figure 4.6 parts (a) and (b) respectively. Here, the thickness is varied independently for both the MoO_x anode buffer layer (between 0 and 50 nm) and the Ca layer (0 and 50 nm). In each case, the thickness of the PCDTBT:$PC_{70}BM$ layer is fixed at the respective interference maximum of 75 nm for Ca/Ag and 85 nm for Ca/Al.

It can be seen that for all devices, the photocurrent is apparently reduced as the thickness of the MoO_x layer increases. The modelling suggests that this effect has two origins; in MoO_x layers having a thickness $\leq$ 10 nm, it appears that photocurrent is reduced by additional absorption by the MoO_x with such absorption being approximately linearly dependent upon MoO_x thickness. This effect is however relatively small; for example in a device incorporating a 10 nm thick MoO_x film, the absorption by the MoO_x is around 3% of that of the PCDTBT:$PC_{70}BM$ layer.

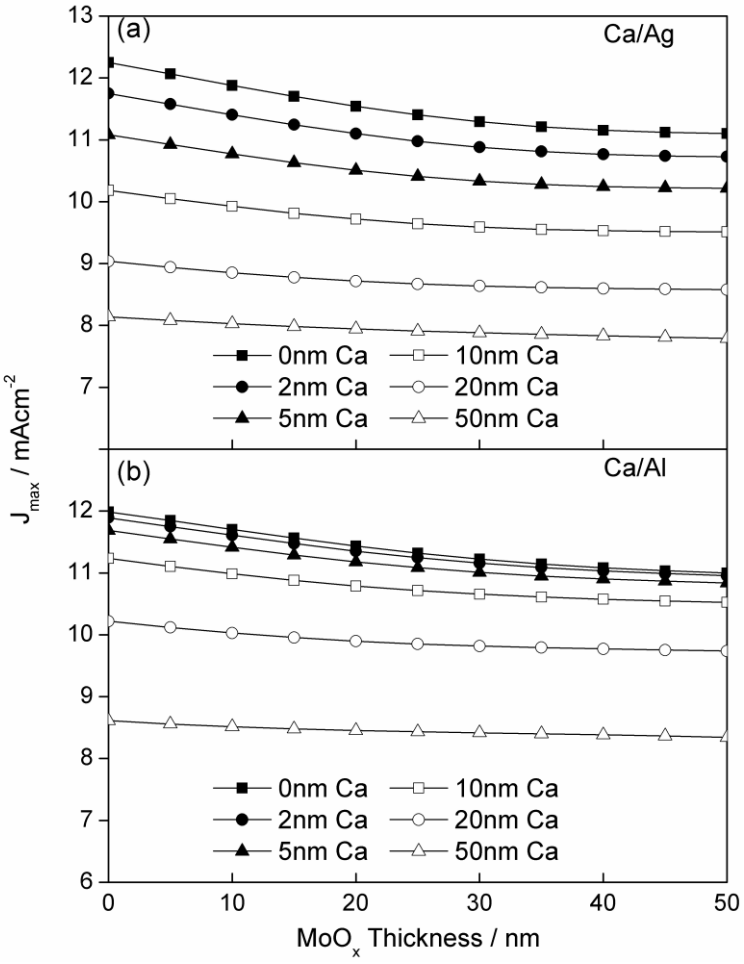

Figure 4.6 The calculated J_{max} for a PCDTBT:$PC_{70}BM$ OPV as a function of MoO_x and Ca layer thickness for (a) a composite Ca/Ag cathode, and (b) a Ca/Al cathode. For both cathodes, the thickness of the active semiconductor remains constant at its optimised value of 75 and 85 nm respectively.

The effect of thicker MoO_x layers is however more complicated, as such layers both absorb more light as well as redistribute the electromagnetic field within the device in a non-linear fashion [25,28]. This redistribution will, in many cases, reduce the absorption by the active layer and thereby reduce the device photocurrent as exemplified by Figure 4.6. The modelling

also indicates that the addition of a Ca layer (of any thickness) similarly reduces J_{max} below that of a device incorporating either a pure Al or Ag cathode. Greater losses result from the use of a thicker Ca layer which is consistent with increased optical loss in the absorptive Ca. Intriguingly, the model suggests that the efficiency of Ca interfaces backed with Al are more efficient, with lower optical loss, than those backed with highly reflective Ag for any given thickness of Ca.

To explore the origin of this result, the optical absorption and field strength at the active layer:cathode interface, for a composite cathode based on 5 nm of Ca backed with either Al or Ag (as shown in Figure 4.7(a) and (b) respectively), are calculated. The MoO_x thickness was kept constant at 10 nm and the active layer thickness fixed at 75 or 85 nm for Ca/Ag and Ca/Al, respectively. Figure 4.7 shows the value of E^2 (where E is the confined electromagnetic field amplitude within the device, see Section 3.10) as a function of distance from the cathode interface. Here, data is plotted for a range of wavelengths between 400 and 650 nm, corresponding to the photoresponse of the active layer. It can be seen that there is a significantly higher penetration of the electromagnetic field into the Ag reflector compared to Al; an effect commensurate with its larger skin-depth (lower optical density).

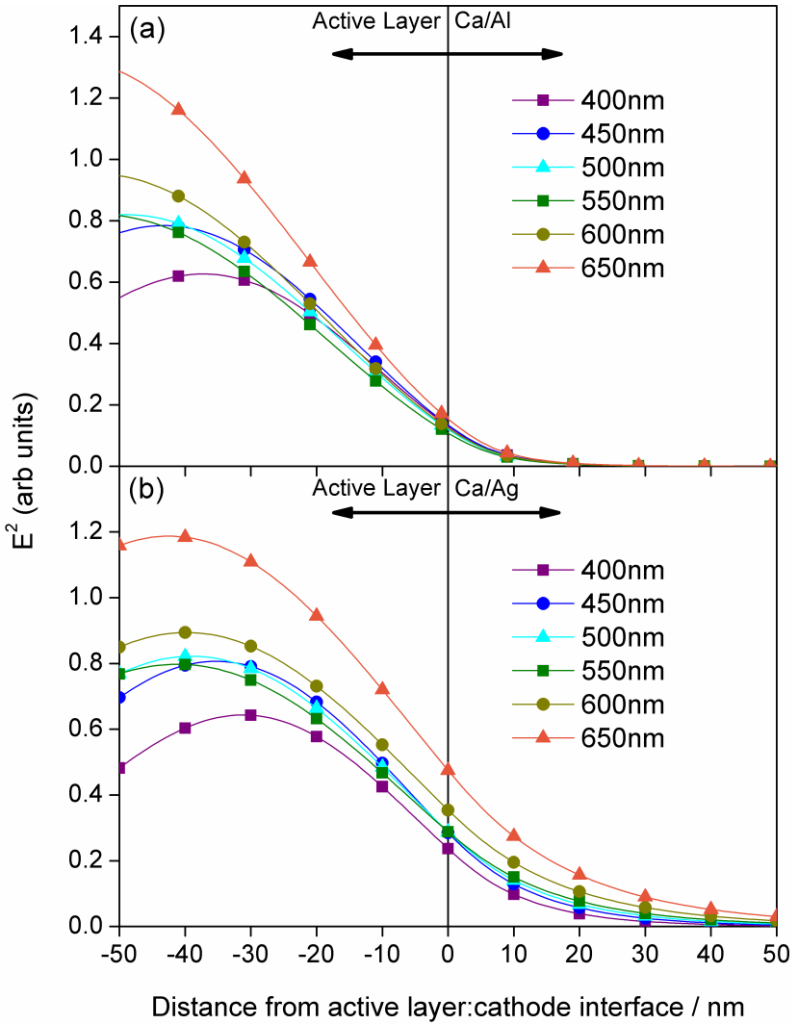

Figure 4.7 Part (a) shows the calculated electric field intensity (E^2) at the interface between the active semiconductor layer and the Ca/Al cathode in a PCDTBT:$PC_{70}BM$ OPV. Part (b) similarly shows E^2 for an OPV device utilising a Ca/Ag cathode. In both parts, field intensity is plotted at a number of different characteristic wavelengths as indicated in the figure, with the thickness of the MoO_x layer constant at 10 nm and the calcium layer being 5 nm.

Using the transfer matrix model enables the optical absorption within each of the individual layers within the device to be calculated. In particular, in a Ca/Ag cathode the relative total absorption of the optical field in the Ca and

Ag layers are predicted to be 21% and 4% respectively. In a device utilising a Ca/Al cathode however, the relative absorption in the Ca and Al layers is 7% and 10% respectively. This demonstrates that whilst Al is more absorptive at optical frequencies than Ag, its smaller skin depth reduces the field intensity close to its surface, and thus absorption in the significantly more absorptive Ca layer is reduced, with more optical energy absorbed by the active semiconductor layer (resulting in a higher value of J_{max} when a composite cathode is used).

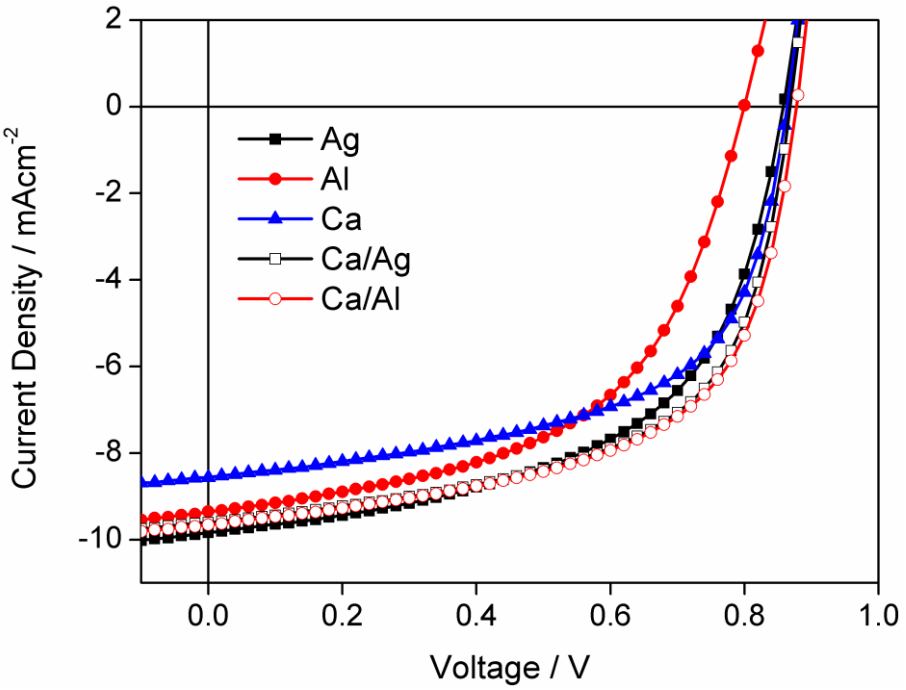

Figure 4.8 Measured J-V characteristics for Ag, Al, Ca, Ca/Ag and Ca/Al based PCDTBT:$PC_{70}BM$ (1:4) OPV devices having a 10 nm thick MoO_x hole extraction layer. For both devices utilising a composite cathode, the calcium layer is fixed at 5 nm.

A series of devices based on either an Ag, Al, Ca, Ca (5 nm)/Ag or Ca (5 nm)/Al cathode were fabricated to examine the extent to which the optical structure of the cathode determines the practical efficiency of a PCDTBT:$PC_{70}BM$ OPV. The J-V characteristics of representative devices are plotted in Figure 4.8, with device metrics summarised in Table 4.2. Note that the individual results presented in Table 4.2 are the average from at least 24 different pixels (maximum PCE presented in parentheses) with error bars representing the standard deviation about the mean for the top 12 performing pixels. It can be seen that the most efficient devices are created using the Ca/Al composite cathode, having a maximum PCE of 5.0%.

A small variation in short-circuit current between the different cathode devices can be seen, with devices having an Ag cathode displaying the highest values of J_{sc}; a result in qualitative agreement with the modelling results shown in Figure 4.5(b). It can be seen however that the J_{sc} recorded from both the composite Ca/Al and Ca/Ag cathode devices are identical to one another, within experimental uncertainty, and also similar to a device using a pure silver cathode. Clearly, the larger photocurrent (approximately 6%) predicted by the use of a Ca/Al cathode compared to a Ca/Ag cathode, from the model, is not reproduced within experimental uncertainty. However the J_{sc} recorded from devices using a pure Ca cathode are 88% that of the Ag cathode devices; a result qualitatively consistent with enhanced optical loss in the absorptive calcium.

Cathode	J_{sc} / $mAcm^{-2}$	V_{oc} / V	FF / %	PCE average [max] / %
Ag	-9.6 ± 0.1	0.85 ± 0.01	55.7 ± 0.9	4.55 ± 0.07 [4.68]
Al	-9.2 ± 0.1	0.78 ± 0.01	53.1 ± 0.9	3.90 ± 0.06 [4.01]
Ca	-8.4 ± 0.1	0.86 ± 0.01	58.7 ± 0.4	4.26 ± 0.04 [4.33]
Ca/Ag	-9.4 ± 0.2	0.86 ± 0.01	59.5 ± 0.4	4.81 ± 0.09 [4.94]
Ca/Al	-9.4 ± 0.1	0.86 ± 0.01	60.6 ± 0.3	4.90 ± 0.06 [5.01]

Table 4.2 Device metrics for a series of nominally identical PCDTBT:$PC_{70}BM$ devices prepared using different cathodes. A 10 nm MoO_x anode buffer layer was utilised for all. The average obtained from the top 50% of 24 pixels, with the errors represented by their standard deviation. The maximum PCE is displayed in parentheses.

The V_{oc} of the different devices are similar at around 0.85 V; a value consistent with previous studies in which values between 0.75 [23] and 0.91 V [2] have been reported. Interestingly, the V_{oc} of devices utilising an Al cathode were significantly lower than those of either Ca or Ag based devices. It can be seen that despite the work function of the materials used varying by 1.4 eV ($\Phi_{Al} - \Phi_{Ca}$) [29], the differences between the V_{oc} of the different devices do not exceed 100 mV (with only 10 mV separating the V_{oc} of Ag and Ca cathode devices, see Section 2.6.4 for details regarding the V_{oc} in devices). Notably however, the largest V_{oc} is recorded from devices having a layer of calcium adjacent to the top of the semiconductor surface; an outcome arising from charge transfer to the fullerene as well as Fermi-pinning [25].

It is clear that there is also a significant difference in the FF of the different devices, with the largest value of ~ 60% being recorded in devices utilising a Ca/Al cathode. The significantly enhanced FF of the Ca/Al, high V_{oc} and relatively high J_{sc} (due to low optical losses) result in these devices having the highest PCE; a result in agreement with other reports [30] on the effectiveness of composite metal cathodes to optimise the efficiency of P3HT:PCBM based devices.

Finally, the effect of active layer thickness in determining the efficiency of the composite cathode devices is addressed. Here, devices are fabricated using a composite Ca/Al cathode (5 nm / 100 nm) and a 10 nm thick MoO_x anode buffer layer. The measured PCE, V_{oc} and FF of the devices as a function of PCDTBT:PC_{70}BM thickness is shown in Figure 4.9(a), with the photocurrent (average J_{sc} and at -1 V) shown in Figure 4.9(b). For comparison, the J_{max} calculated using the transfer matrix model for the device in part (b) is also plotted.

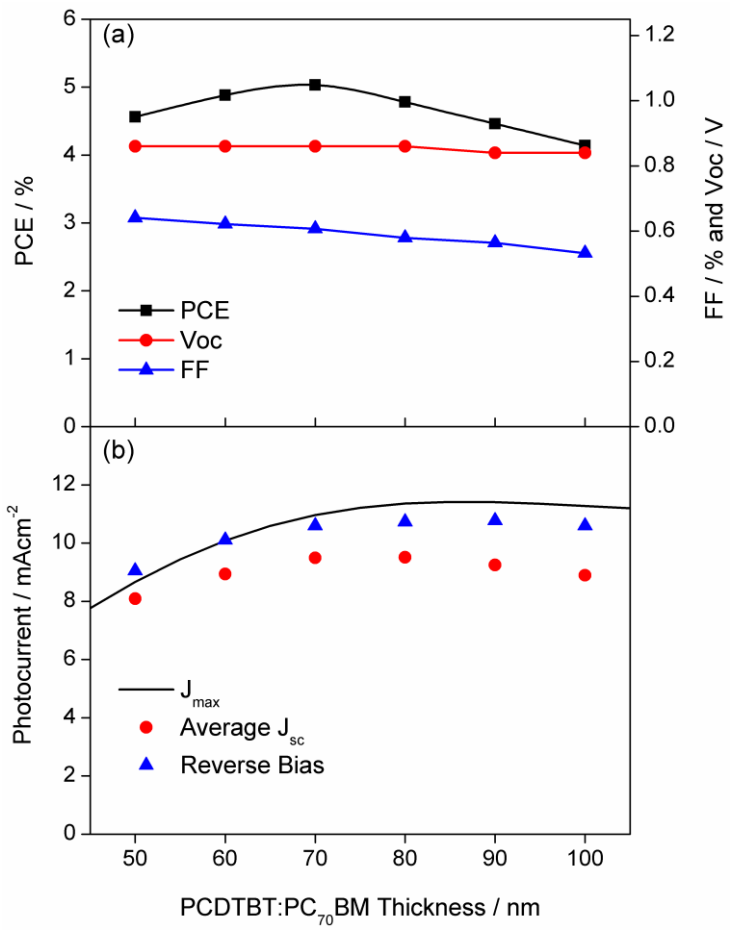

Figure 4.9 Part (a) shows the PCE, V_{oc} and FF values of a series of PCDTBT:PC_{70}BM devices with varying active layer thickness, a 10 nm MoO_x anode buffer layer and 5 nm Ca buffer layer capped with Al. Connecting lines are used as a guide to the eye. Part (b) shows the measured J_{sc} and photocurrent at a reverse bias of -1 V from the same series of OPVs as a function of active layer thickness. The calculated maximum photocurrent (J_{max}) of each device is also shown using a line.

As it can be seen, the device V_{oc} remains approximately constant over the range of active layer thicknesses studied (50 to 100 nm). These results are in agreement with other recent studies that also evidenced a drop-off in V_{oc}, FF and PCE in PCDTBT:PC_{70}BM OPVs as active layer thickness is increased

to over 200 nm [23]. The measured J_{sc} is on average 15% lower than the predicted J_{max}, with the discrepancy increasing as the thickness of the active layer increases. However, when a bias of -1 V is applied to the device, the agreement between the recorded photocurrent and J_{max} is much improved; although for films having a thickness ≥ 80 nm, the recorded photocurrent is observed to be slightly less than J_{max}. This clearly indicates that device efficiency is limited by charge extraction; a problem that becomes more severe as the active layer thickness increases. In addition to this observation, the FF also undergoes some reduction as film thicknesses increases. Indeed, despite the optical model suggesting that the most efficient devices should be created using PCDTBT:$PC_{70}BM$ layer having a thickness of ~85 nm (thereby maximising the photocurrent), the highest device PCE recorded (5.1%) is obtained in devices having a PCDTBT:$PC_{70}BM$ thickness of 70 nm (similarly observed in Section 4.2 regarding the optimisation of anode buffer layers, see Table 4.1). This confirms other work that suggests that the efficiency of PCDTBT-based OPVs is limited by sub-optimal charge extraction resulting from non-geminate recombination (including traps) [23].

4.4 – Conclusion

In summary, the effects of different anode buffer layers and cathode structures on the maximum device performance that can be obtained from a PCDTBT:$PC_{70}BM$ OPV have been studied. The use of metal oxides at the anode layer provides improved efficiency through increases in device FF and V_{oc} (most likely due to improved energy level alignment). Device

stability tests displayed only minor degradation in efficiency after 2 months for a MoO_x and V_2O_5 anode buffer layer.

By using a transfer matrix reflectivity model, the maximum photocurrent was modelled for a variety of cathode materials with composite structures, including structures in which a thin film of calcium was backed with an optically thick layer of aluminium or silver. Device photocurrent was observed to be a function of cathode reflectivity although the work function of the cathode plays only a minor role in determining the device V_{oc} due to Fermi-pinning. Composite cathodes result in both high reflectivity (and thus efficient optical harvesting), good fill factor (efficient charge extraction) and slightly improved open circuit voltage; effects which combine to produce devices having optimal power conversion efficiencies.

The advantages obtained in using devices utilising a Ca/Al composite cathode is used throughout the remaining chapters of this thesis. This technique allows high performance devices to be created using a variety of alternative donor polymers.

References

1. N. Blouin, A. Michaud, M. Leclerc, A low-bandgap poly(2,7-carbazole) derivative for use in high-performance solar cells, *Adv. Mater.*, **2007**, *19*, 2295-2300
2. T.-Y. Chu, S. Alem, P.G. Verly, S. Wakim, J. Lu, Y. Tao, S. Beaupré, M. Leclerc, F. Bélanger, D. Désilets, S. Rodman, D. Waller, R.

Gaudiana, Highly efficient polycarbazole-based organic photovoltaic devices, *Appl. Phys. Lett.*, **2009**, *95*, 063304

3. S.H. Park, A. Roy, S. Beaupré, S. Cho, N. Coates, J.S. Moon, D. Moses, M. Leclerc, K. Lee, A.J. Heeger, Bulk heterojunction solar cells with internal quantum efficiency approaching 100%, *Nat. Photonics*, **2009**, *3*, 297-302
4. T. Wang, A.J. Pearson, A.D.F. Dunbar, P.A. Staniec, D.C. Watters, H. Yi, A.J. Ryan, R.A.L. Jones, A. Iraqi, D.G. Lidzey, Correlating structure with function in thermally annealed PCDTBT:$PC_{70}BM$ photovoltaic blends, *Adv. Funct. Mater.*, **2012**, *22*, 1399-1408
5. D.H. Wang, K.H. Park, J.H. Seo, J. Seifter, J.H. Jeon, J.K. Kim, J.H. Park, O.O. Park, A.J. Heeger, Enhanced power conversion efficiency in PCDTBT/$PC_{70}BM$ bulk heterojunction photovoltaic devices with embedded silver nanoparticle clusters, *Adv. Energy Mater.*, **2011**, *1*, 766-770
6. Y. Sun, C.J. Takacs, S.R. Cowan, J.H. Seo, X. Gong, A. Roy, A.J. Heeger, Efficient, air-stable bulk heterojunction polymer solar cells using MoO_x as the anode interfacial layer, *Adv. Mater.*, **2011**, *23*, 2226-2230
7. V. Shrotriya, G. Li, Y.Y. Yao, C.W. Chu, Y. Yang, Transition metal oxides as the buffer layer for polymer photovoltaic cells, *Appl. Phys. Lett.*, **2006**, *88*, 073508
8. C. Tao, S. Ruan, G. Xie, X. Kong, L. Shen, F. Meng, C. Liu, X. Zhang, W. Dong, W. Chen, Role of tungsten oxide in inverted polymer solar cells, *Appl. Phys. Lett.*, **2009**, *94*, 043311

9. S. Han, W.S. Shin, M. Seo, D. Gupta, S.-J. Moon, S. Yoo, Improving performance of organic solar cells using amorphous tungsten oxides as an interfacial buffer layer on transparent anodes, *Org. Electron.*, **2009**, *10*, 791-797
10. C.H. Peters, I.T. Sachs-Quintana, W.R. Mateker, T. Heumueller, J. Rivnay, R. Noriega, Z.M. Beiley, E.T. Hoke, A. Salleo, M.D. McGehee, The mechanism of burn-in loss in a high efficiency polymer solar cell, *Adv. Mater.*, **2012**, *24*, 663-668
11. D.M. de Leeuw, M.M.J. Simenon, A.R. Brown, R.E.F. Einerhand, Stability of n-type doped conducting polymers and consequences for polymeric microelectronic devices, *Synthetic Met.*, **1997**, *87*, 53-59
12. K. Norman, M.V. Madsen, S.A. Gevorgyan, F.C. Krebs, Degradation patterns in 16883-16892
13. M.P. de Jong, L.J. van Ijzendoorn, M.J.A. de Voigt, Stability of the interface between indium-tin-oxide and poly(3,4-ethylenedioxythiophene)/ poly(styrenesulfonate) in polymer light-emitting diodes, *Appl. Phys. Lett.*, **2000**, *77*, 2255-2257
14. E. Voroshazi, B. Verreet, A. Buri, R. Müller, D. Di Nuzzo, P. Heremans, Influence of cathode oxidation via the hole extraction layer in polymer:fullerene solar cells, *Org. Electron.*, **2011**, *12*, 736-744
15. J. Hou, H.-Y. Chen, S. Zhang, R.I. Chen, Y. Yang, Y. Wu, G. Li, Synthesis of a low band gap polymer and its application in highly efficient polymer solar cells, *J. Am. Chem. Soc.*, **2009**, *131*, 15586-15587

16. H.-Y. Chen, J. Hou, S. Zhang, Y. Liang, G. Yang, Y. Yang, L. Yu, Y. Wu, G. Li, Polymer solar cells with enhanced open-circuit voltage and efficiency, *Nature Photonics*, **2009**, *3*, 649-653
17. L. Huo, S. Zhang, X. Guo, F. Xu, Y. Li, J. Hou, Replacing alkoxy groups with alkylthienyl groups: A feasible approach to improve the properties of photovoltaic polymers, *Angew. Chem. Int. Ed.*, **2011**, *50*, 9697-9702
18. Y. Liang, D. Feng, Y. Wu, S.-T. Tsai, G. Li, C. Ray, L. Yu, Highly efficient solar cell polymers developed via fine-tuning of structural and electronic properties, *J. Am. Chem. Soc.*, **2009**, *131*, 7792-7799
19. Y. Liang, Z. Xu, J. Xia, S.-T. Tsai, Y. Wu, G. Li, C. Ray, L. Yu, For the bright future - bulk heterojunction polymer solar cells with power conversion efficiency of 7.4%, *Adv. Mater.*, **2010**, *22*, E135-E138
20. J. Griffin, D.C. Watters, H. Yi, A. Iraqi, D. Lidzey, A.R. Buckley, The influence of MoO_x anode stoicheometry on the performance of bulk heterojunction polymer solar cells, *Adv. Energy Mater.*, **2013**, *3*, 903-908
21. J. Gilot, I. Barbu, M.M. Wienk, R.A.J. Janssen, The use of ZnO as optical spacer in polymer solar cells: theoretical and experimental study, *Appl. Phys. Lett.*, **2007**, *91*, 113520
22. L.H. Slooff, S.C. Veenstra, J.M. Kroon, D.J.D. Moet, J. Sweelssen, M.M. Koetse, Determining the internal quantum efficiency of highly efficient polymer solar cells through optical modeling, *Appl. Phys. Lett.*, **2007**, *90*, 143506

23. Z.M. Beiley, E.T. Hoke, R. Noriega, J. Dacuña, G.F. Burkhard, J.A. Bartelt, A. Salleo, M.F. Toney, M.D. McGehee, Morphology-dependent trap formation in high performance polymer bulk heterojunction solar cells, *Adv. Energy Mater.*, **2011**, *1*, 954-962
24. F. Etzold, I.A. Howard, R. Mauer, M. Meister, T.-D. Kim, K.-S. Lee, N.S. Baek, F. Laquai, Ultrafast exciton dissociation followed by nongeminate charge recombination in PCDTBT:PCBM photovoltaic blends, *J. Am. Chem. Soc.*, **2011**, *133*, 9469-9479
25. R. Steim, F.R. Kogler, C.J. Brabec, Interface materials for organic solar cells, *J. Mater. Chem*., **2010**, *20*, 2499-2512
26. A. Hadipour, D. Cheyns, P. Heremans, B.P. Rand, Electrode considerations for the optical enhancement of organic bulk heterojunction solar cells, *Adv. Energy Mater*., **2011**, *1*, 930-935
27. A.K. Pandey, P.E. Shaw, I.D.W. Samuel, J.M. Nunzi, Effect of metal cathode reflectance on the exciton-dissociation efficiency in heterojunction organic solar cells, *Appl. Phys. Lett.*, **2009**, *94*, 103303
28. B.V. Andersson, D.M. Huang, A.J. Moulé, O. Inganäs, An optical spacer is no panacea for light collection in organic solar cells, *Appl. Phys. Lett.*, **2009**, *94*, 043302
29. C.J. Brabec, A. Cravino, D. Meissner, N.S. Sariciftci, T. Fromherz, M.T. Rispens, L. Sanchez, J.C. Hummelen, Origin of the open circuit voltage of plastic solar cells, *Adv. Funct. Mater*., **2001**, *11*, 374-380
30. M.O. Reese, M.S. White, G. Rumbles, D.S. Ginley, S.E. Shaheen, Optimal negative electrodes for poly (3-hexylthiophene):[6,6]-phenyl

C61-butyric acid methyl ester bulk heterojunction photovoltaic devices, *Appl. Phys. Lett.*, **2008**, *92*, 053307

Chapter 5

Improving the solubility of PCDTBT with octyloxy substituents on the benzothiadiazole unit

In the previous chapter, details were given regarding the selection of the anode buffer layer and cathode material for optimised PCDTBT based devices. During preparation of the active layer semiconductor solution it was evident that the polymer exhibited poor solubility which increased device preparation times. This chapter addresses novel polymers based on PCDTBT with its aim to improve polymer solubility. Two polymers were synthesised and tested; namely the materials PCDTBT-8 and PCDT2BT-8. Optical and electronic properties of these polymers will be discussed together with an analysis of their solubility via solution preparation at various concentrations. Organic field effect transistor (OFET) hole mobilities will be presented as well as an optimisation study of bulk heterojunction solar cells for both novel polymers. An emphasis will be placed on the significance and importance of thermal annealing treatments.

5.1 – Introduction

An appealing aspect of organic photovoltaic devices is the large combination of polymer materials that can be designed as electron-donors. Many research groups have studied the effects of various alterations along the polymer backbone on the optical and electronic properties of a polymer, as described in Section 2.3 and discussed in review articles [1-7]. Each method affects a different aspect of polymer behaviour, thus allowing the fine-tuning of polymer properties to enhance the efficiency and performance of OPV devices.

The inclusion of electron-deficient groups, for example octyloxy substituents on the benzothiadiazole (BT) unit, can allow the HOMO energy level to be increased with only minor affects on the polymer absorption [8]. Polymers containing octyloxy substituents have also been observed to exhibit higher solubility and therefore an increased synthesis yield and molecular weight (M_w) [9-12]. This enhanced solubility is likely to be due to the increase of solution entropy, as discussed in Section 2.4. Such manipulation of chemical structure is likely to be beneficial as a result of increased solution preparation times, increased V_{oc} values as well as superior stability against oxidation. A number of side-groups have been previously functionalised on the BT unit, including octyloxy (OC_8H_{17}), decyloxy ($OC_{10}H_{21}$) [13], dodecyloxy ($OC_{12}H_{25}$) [14] and tetradecyloxy ($OC_{14}H_{29}$) [15].

The absorption of a donor-acceptor conjugated polymer however undergoes only minor changes upon functionalising side-groups on the BT. To enhance the device J_{sc}, the resultant polymer needs to increase the overlap with the long wavelength regime of the solar spectrum. One technique to achieve such a red-shift in low bandgap polymers is to increase the conjugation length through the inclusion of additional thiophene repeat units along the polymer backbone. This has been performed for various polymers containing either a fluorene unit [16-18], indolocarbazole [19,20] or thiophene-phenylene-thiophene (TPT) coplanar units [21,22]. It is particularly important to stress here that a red-shift is not always achieved through this technique as it is dependent on the polymer structure, with the

interactions between the donor-acceptor components of the parent co-polymer playing a crucial role [23].

Device fabrication techniques (e.g. post-deposition thermal treatments) also play a critical role in determining OPV efficiency. Unlike the polymer PCDTBT which has been shown to not require a thermal annealing process to optimise device efficiency [24], various other polymers have displayed enhanced performance upon being thermally annealed (for example P3HT [25,26] and POD2T-DTBT [27]). Here, annealing at or above the polymer:fullerene blend glass transition temperature (T_g) can drive modification in the active layer morphology which, as discussed previously, can increase device efficiency.

Figure 5.1 shows the chemical structure of the polymers PCDTBT-8 (a) and PCDT2BT-8 (b) explored in this chapter. These materials were synthesised by Dr. H. Yi and Dr. A. Iraqi in the Department of Chemistry at the University of Sheffield. Both polymers are functionalised with octyloxy substituents on the BT unit, with PCDT2BT-8 also having additional thiophene moieties along the polymer backbone. Note that PCDTBT-8 is similar to PC-DODTBT [10] and HXS-1 [28] materials, with the latter differing through the substitution of a linear chain on the carbazole unit. In contrast with the results presented in this chapter, PC-DODTBT was unable to realise OPV PCEs > 1.5%. This may be due to sub-optimal active layer morphology from either incorrect polymer:fullerene blend ratios or casting solvent. Additionally, the HOMO energy level of PC-DODTBT is 5.11 eV

(~ 0.3 eV lower than PCDTBT-8) which could partly explain the low observed V_{oc}. It is also worth noting that although HXS-1 devices achieved efficiencies > 5%, the polymer exhibited poor solubility as its active layers had to be spincast from a heated solution. This chapter will, however, present the individual optimisation of PCDTBT-8 and PCDT2BT-8 based on conditions established from Chapter 4.

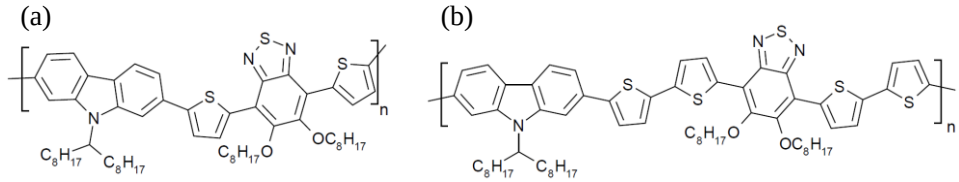

Figure 5.1 Chemical structures of (a) PCDTBT-8 and (b) PCDT2BT-8.

5.2 – UV-Vis spectroscopy and energy levels

The absorption spectra of polymers PCDTBT, PCDTBT-8 and PCDT2BT-8 when prepared into thin films are shown in Figure 5.2, with peak values and optical energy gaps displayed in Table 5.1. It can be seen that the introduction of the solubilising substituents on the benzothiadiazole (BT) unit cause a blue-shift in the peak absorption wavelength for PCDTBT-8 (536 nm compared to 570 nm for PCDTBT). The onset of absorption for this polymer occurs at a value of 627 nm, correlating to an optical energy gap of 1.98 eV; a value ~ 0.1 eV larger than PCDTBT. This increased energy gap corresponds to reduced electronic delocalisation which could be due to the electron donating properties of the octyloxy substituents reducing the electron accepting characteristics of the BT moiety; properties that may ultimately affect the overall charge carrier mobility. Replacing the branched

sidegroup on the carbazole unit with a linear group (i.e. as was done for HXS-1) causes a small spectral shift of the absorption peak to ~ 540 nm, with a shoulder existing at 579 nm and an optical energy gap of ~ 1.95 eV [28]. This optical energy gap is similar to that of PCDTBT-8, suggesting a similar effect on the electronic conjugation due to the presence of the octyloxy substituents.

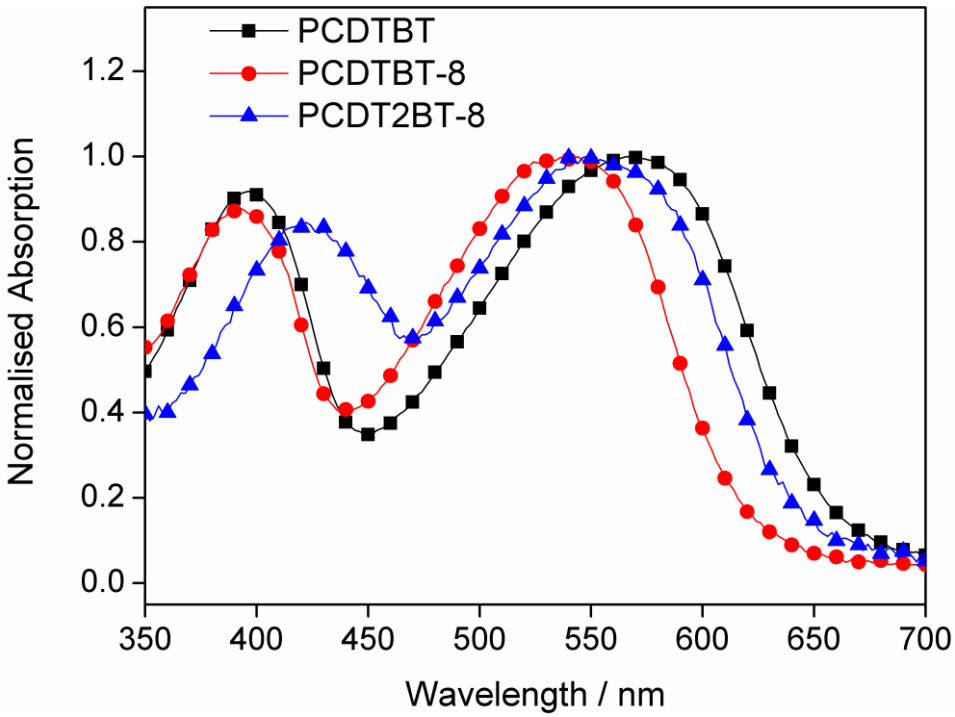

Figure 5.2 Normalised thin film UV-Vis absorption spectra for PCDTBT (spun from $CHCl_3$), PCDTBT-8 (CB) and PCDT2BT-8 ($CHCl_3$).

The absorption spectrum is red-shifted upon inclusion of additional thiophene rings along the polymer backbone, as is evident in PCDT2BT-8. In this polymer, the peak absorption is positioned at 548 nm corresponding to a red-shift of ~ 12 nm compared with PCDTBT-8, with an absorption onset at ~ 642 nm (an optical energy gap of ~ 1.93 eV). The inclusion of

two additional thiophene moieties along the polymer backbone results in a reduced optical energy gap of ~ 0.05 eV compared with PCDTBT-8, as a result of increased electronic conjugation. This increase in conjugation length is probably due to both steric and electronic factors. As thiophene units contribute towards the electron charge density along the polymer backbone, additional thiophene moieties are likely to increase intramolecular charge transport, a result consistent with enhanced OFET hole mobility as reported later in Section 5.5.1. Furthermore, the distance between octyloxy substituents is increased along the polymer chain, thereby reducing their mutual steric interactions and resulting in a reduced optical energy gap. Comparing the absorption spectra of PCDT2BT-8 as a thin film and in a $CHCl_3$ solution (see Table 5.1) there are only small changes in peak wavelength, suggesting little to no structural differences.

Polymer	λ_{max} / nm Thin film ($CHCl_3$ Solution)	E_g^{op} / eV	M_w / kDa	HOMO / eV	LUMO / eV
PCDTBT	396 (392) / 570 (547)	1.88	32.6	-5.35	-3.42
PCDTBT-8	391 (384) / 536 (513)	1.98	34.8	-5.40	-3.27
PCDT2BT-8	421 (420) / 548 (542)	1.93	57.2	-5.20	-3.29

Table 5.1 UV-Vis, optical energy gaps, molecular weight and HOMO/LUMO energy levels of PCDTBT, PCDTBT-8 and PCDT2BT-8. Data acquired by Hunan Yi and Solyman Al-Faifi from the Chemistry department.

The energy levels (as determined from CV) for the three polymers are shown in Table 5.1. The inclusion of octyloxy sidegroups on the BT unit increases the HOMO energy level (consistent with the introduction of electron-deficient groups) possibly due to the reduced electronic conjugation along the polymer backbone. The inclusion of additional thiophenes (PCDT2BT-8) results in a reduced HOMO energy level but with a LUMO energy level comparable with that of PCDTBT-8. The change in the HOMO level is likely to be due to the presence of the more electron donating thiophene repeat units along the polymer backbone (c.f. P3HT HOMO energy level of -5.2 eV [29]). The similar LUMO levels for PCDTBT-8 and PCDT2BT-8 is a result consistent with a weakening of the electron accepting capabilities of the BT moiety upon inclusion of the electron donating octyloxy substituents.

5.3 – Determining the solubility of the polymers and polymer:fullerene blends

To explore the solubility limits of the polymers PCDTBT, PCDTBT-8 and PCDT2BT-8, each were dissolved in $CHCl_3$ at various concentrations, heated for the same length of time and then filtered through a 0.45 μm PTFE filter. Solubility could be judged by the presence (or lack thereof) of polymer aggregates in the solution as well as the clarity or turbidness of the solution. The use of a PTFE filter allowed a further determination of the extent of undissolved polymeric material that remained within the solution.

It was found that PCDTBT did not fully dissolve; even at a low concentration of 2 mg/ml. Polymeric aggregates were clearly visible at 5 mg/ml while at 20 mg/ml a gelatinous solution was formed. In contrast, PCDTBT-8 displayed turbid solutions only at concentrations in excess of 5 mg/ml and did not form polymer aggregates in any of the solutions. The longer polymer backbone of PCDT2BT-8 resulted in the formation of turbid solutions at all concentrations. However, the octyloxy sidegroups similarly prevented each solution from forming any polymer aggregates. These results suggest that the introduction of the substituents on the BT unit allow the polymer to dissolve at high concentrations without allowing the formation of aggregates.

Passing the various solutions through a PTFE filter provides a complementary measure of polymer solubility. A PCDTBT solution diluted to 1 mg/ml was able to be filtered without blocking the filter pores. PCDT2BT-8 also necessitated a similar concentration for complete filtration (a consequence of its longer polymer backbone). However, PCDTBT-8 could be easily filtered at concentrations in excess of 10 mg/ml. Upon performing similar tests where the polymer was mixed with $PC_{70}BM$ (at a 1:4 w/w blend ratio) it was found that the introduction of the fullerene aids polymer solubility and allows a significant increase in maximum solution concentration that could be achieved.

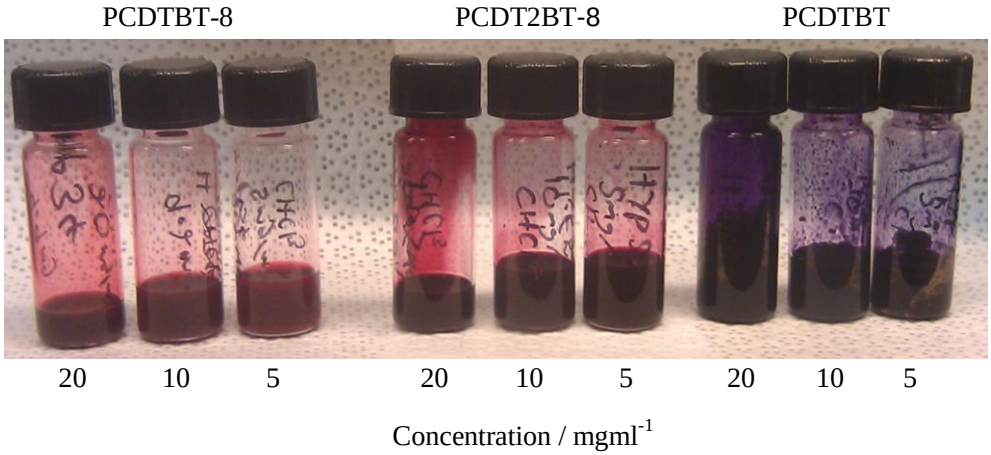

Figure 5.3 An optical image of PCDTBT-8, PCDT2BT-8 and PCDTBT at various concentrations in $CHCl_3$. Solution preparation and photo taken by Dr James Kingsley.

An optical image of the polymer solutions at the various concentrations tested is displayed in Figure 5.3. Here, the differences in solubility are clearly evident. PCDTBT was determined to have a solubility limit at ~ 1 mg/ml and 50 mg/ml (pristine and fullerene blend solution respectively), whereas the introduction of the octyloxy sidegroups caused PCDTBT-8 to be significantly more soluble with limits at 20 mg/ml and > 50 mg/ml. PCDT2BT-8 has limits at ~ 1 mg/ml and 20 mg/ml due to the additional thiophene rings along the backbone. The inclusion of side-chains on the extra thiophene moieties would most likely further enhance the solubility of PCDT2BT-8, however a polymer without such sidegroups would likely be insoluble if the octyloxy substituents were to be removed (see Chapter 7 for comparisons of analogous polymers where varying the positioning of the soluble sidechains for fluorene based polymers is described). It is also clear that the introduction of $PC_{70}BM$ into solutions causes an improvement in

polymer solubility; this is indicative that the fullerene material is capable of filling spaces between polymer chains, therefore aiding solubilisation.

5.4 – GIWAXS

To determine whether the introduction of octyloxy substituents affects the polymer π-π packing in a thin film, grazing incident wide-angle x-ray scattering (GIWAXS, see Section 3.7) was used to probe the molecular packing for PCDTBT and PCDTBT-8. The measured diffraction patterns are displayed in Figure 5.4. The π-π stacking distance for PCDTBT was determined to be 4.00 ± 0.02 Å whereas PCDTBT-8 was found to be 4.2 ± 0.03 Å. This increased intermolecular distance is a result consistent with the introduction of octyloxy sidegroups increasing the separation between polymer chains (similar conclusions are presented in Chapter 6). If the π-π packing distance of PCDTBT-8 is compared with HXS-1 (which exhibited a π-π distance of 4.0 Å) it appears that the linear group on the HXS-1 carbazole unit allows the polymer chains to pack more closely; as occurs for PCDTBT. Combining the linear sidechain on the carbazole unit as well as a non-substituted BT unit could lead to even smaller π-π distance, although reduced solubility is likely to be significant.

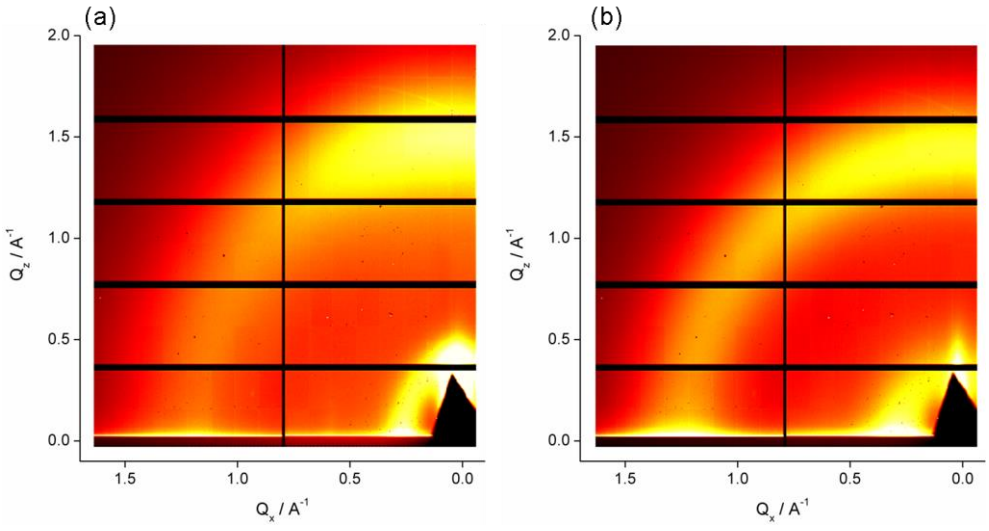

Figure 5.4 2D-GIWAXS images of pure PCDTBT (a) and PCDTBT-8 (b) thin films cast onto silicon/silicon oxide substrates at a grazing angle of 0.2º.

5.5 – Device optimisation

The polymers PCDTBT-8 and PCDT2BT-8 were subjected to a device optimisation regime where the choice of casting solvent, blend ratio (with $PC_{70}BM$), active layer thickness, and thermal annealing temperature were investigated. Throughout the process, a composite cathode of calcium / aluminium (5 / 100 nm) was used (see Section 4.3 for full details). The results from the optimisation of OPV devices based on the two materials are shown in Table 5.2.

Polymer	Solvent	Blend Ratio	Active Layer Thickness / nm	Annealing Temperature / °C	J_{sc} / $mAcm^{-2}$	V_{oc} / V	FF / %	PCE / %
PCDTBT	DCB	1:4	50	80	-7.82	0.58	50.8	2.30
	CB	1:4	65	80	-10.85	0.78	46.4	3.93
	$CHCl_3$	1:2	75	80	-8.02	0.82	61.8	4.06
	-	1:3	85	80	-9.19	0.80	57.9	4.26
	-	1:4	65	80	-10.26	0.82	57.8	4.86[(a)]
PCDTBT-8	DCB	1:4	93	80	-6.92	0.76	42.8	2.25
	$CHCl_3$	1:4	72	80	-8.36	0.82	48.8	3.34
	CB	1:2	100	120	-7.28	0.74	39.5	2.13
	-	1:3	100	120	-8.14	0.76	38.7	2.39
	-	1:4	72	80	-8.39	0.82	48.6	3.35
	-	1:4	72	120	-9.38	0.96	46.9	4.22[(a)]
PCDT2BT-8	DCB	1:4	81	80	-8.29	0.80	40.2	2.67
	CB	1:4	87	80	-7.14	0.82	47.4	2.77
	$CHCl_3$	1:2	60	110	-7.60	0.88	49.5	3.31
	-	1:3	59	110	-8.68	0.90	51.7	4.04
	-	1:4	65	80	-8.11	0.82	52.7	3.50
	-	1:4	61	110	-8.44	0.90	54.2	4.12[(a)]

Table 5.2 Optimisation table of devices utilising a PEDOT:PSS anode buffer layer and a Ca/Al composite cathode. [(a)] device metrics used in Figure 5.7.

An important variable explored for both polymers was the casting solvent. Varying the casting solvent has an important effect due to the differing solubility of the polymers as well as the formation of appropriate nanostructure in the active layer, with the resultant morphologies differing due to the varying drying times of the solvents (which is related to their different boiling points, see Section 3.2). The solvents used (in order of their boiling points) were $CHCl_3$, CB and DCB (having boiling points of approximately 61°C, 131°C and 180°C respectively).

Devices utilising a PCDTBT-8:$PC_{70}BM$ blend at a weight ratio of 1:4 (w/w) displayed highest efficiencies when cast from $CHCl_3$ and CB (PCE ≈ 3.35%), with reduced V_{oc} and J_{sc} values when cast from DCB. For devices having active layers comprised of PCDT2BT-8:$PC_{70}BM$ (1:4) had a higher efficiency when cast from $CHCl_3$ (due to improvements in both the J_{sc} and FF) and reached efficiencies of 3.5%. It is clear that despite this polymer exhibiting a reduced optical energy gap, the J_{sc} values are lower than those observed from PCDTBT-8. This could be due to (or a combination of) non-ideal phase separation, non-geminate recombination or a reduced molar absorbance. Note that devices were annealed at 80°C (similar temperature for PCDTBT) to attempt to increase efficiency by extracting trapped solvent within the active layer.

5.5.1 – Thermal annealing

Unlike OPV devices based on PCDTBT in which thermal annealing does not significantly increase PCE (see Section 4.1), both PCDTBT-8 and

PCDT2BT-8 require the use of a thermal annealing step during fabrication to obtain improvements in device efficiency. The glass transition temperature (T_g) for both polymers was measured using spectroscopic ellipsometry (see Section 3.9, as performed by Dr Tao Wang). The resultant T_g values of 80-90°C and 100°C were determined for PCDTBT-8 and PCDT2BT-8 respectively for thin films cast from $CHCl_3$, displayed in Figure 5.5. It is expected that changes in film morphology will occur if a film is annealed at or above its T_g, as molecules in the active region can become more mobile. This offers the prospect of polymer:fullerene blends undergoing organisation to form a film having ideal phase separation more suited to exciton dissociation and charge extraction.

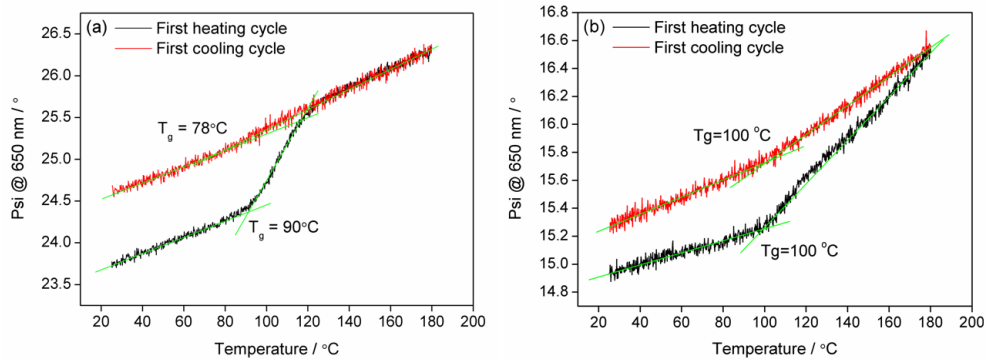

Figure 5.5 Glass transition temperatures T_g measured using spectroscopic ellipsometry for thin films cast from $CHCl_3$ of PCDTBT-8 (a) and PCDT2BT-8 (b) as determined from the first heating and cooling cycles. The initial film thicknesses were 50-60 nm for both polymers.

To determine whether thermal annealing can be used to improve OPV efficiency, completed devices were subjected to various thermal annealing temperatures. In this experiment, the devices were soaked under the solar simulator for a length of ~ 0.5 hr such that their efficiencies stabilised (effectively a simplified burn-in process [30]). Devices were then subjected to an initial thermal annealing temperature of 50°C for 5 mins, and then quickly quenched (cooled) for 1 min before being measured again using the solar simulator. The temperature was then increased by 10°C and repeated until a peak efficiency was observed. Figure 5.6(a) displays the normalised PCE for a PCDTBT-8:$PC_{70}BM$ (1:4 cast from CB) device and a PCDT2BT-8:$PC_{70}BM$ (1:4 cast from $CHCl_3$). A comparison of the V_{oc} for OPVs made from both polymers is also presented in Figure 5.6(b). It can be seen that optimised efficiencies are obtained using a thermal annealing temperature of 120°C for PCDTBT-8 and 110°C for PCDT2BT-8, with the maximum V_{oc} value also coinciding with these temperatures. These temperatures also coincide with the T_g measured for both polymers, suggesting that morphological changes achieved using thermal annealing are critical to improving device efficiency through enhanced V_{oc}. Note that the decrease in efficiency at annealing temperature 120°C for PCDT2BT-8 is due to a large reduction in the J_{sc}.

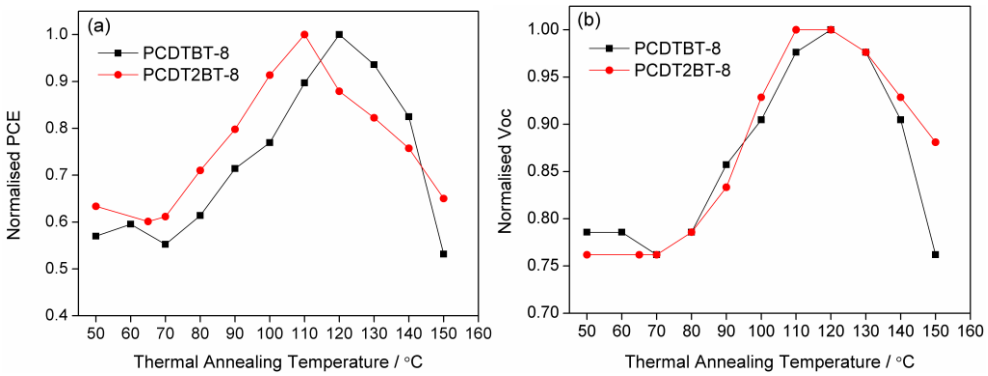

Figure 5.6 – Normalised PCE (a) and V_{oc} (b) for various thermal annealing temperatures. Both polymers were initially exposed to the simulated solar radiation for 0.5 hr prior to any thermal annealing. Devices were then heated for 5 mins at each given temperature and subsequently cooled to room temperature for 1 min before measurement.

A maximum efficiency of 4.4% was obtained for PCDTBT-8 based devices utilising a MoO_x anode buffer layer when spin cast from CB and then thermally annealed at 120°C. This efficiency is reduced to 4.2% when a PEDOT:PSS anode is used instead. This is a significant improvement compared to unannealed devices that yield a maximum PCE of 3.35%. We find that the primary device metric which underwent the largest improvement on annealing was the V_{oc}, which increased from 0.82 V to 0.96 V (corresponding to a ~ 17% improvement). This is a relatively high open-circuit voltage, especially compared to PCDTBT which typically exhibit values of 0.86 V (see Chapter 4). We speculate that this increase is due to a combination of PCDTBT-8 having a deeper HOMO energy level together with a thermal annealing treatment that drives improved vertical stratification or superior contact between the various layers at their interfaces. Despite this large increase, the PCE is mainly limited by its FF

with values < 50%, although OFET hole mobilities (see Section 3.8) indicate values of 4.5 x 10^{-4} $cm^2V^{-1}s^{-1}$; a respectable mobility for an amorphous polymer. Note that HXS-1 has a large FF value of 69% (despite displaying a similar hole mobility); a property that most likely results from a smaller π-π packing distance as well as the use of solvent additives that (as described in more detail in Chapter 7) can also improve the FF.

PCDT2BT-8 can also be used to create OPV devices having an efficiency of 4.1% upon thermally annealing at 110°C, a process that similarly increases the V_{oc} and J_{sc}. Although larger FF values were obtained (possibly due to a greater planarity from the inclusion of extra thiophene rings), device efficiency was lower than PCDTBT-8 due to lower J_{sc} and V_{oc} values. Hole mobilities of 2.7 x 10^{-3} $cm^2V^{-1}s^{-1}$ were obtained pointing to enhanced rigidity of the polymer backbone. However, it is worth noting that the mobility measured for both polymers were from films that were not annealed at their optimised thermal annealing temperatures used to prepare bulk heterojunction devices. This was because the pure polymer films most likely exhibit a different T_g than the polymer:fullerene blends.

Figure 5.7 shows the optimised J-V characteristics of a PCDTBT OPV (taken from Figure 4.2), PCDTBT-8 and PCDT2BT-8 for devices utilising a PEDOT:PSS anode buffer layer and thermally annealed at their respective optimised temperature. The various differences in device metrics are clearly apparent, especially the large improvement in the V_{oc} from BT-8 based polymers.

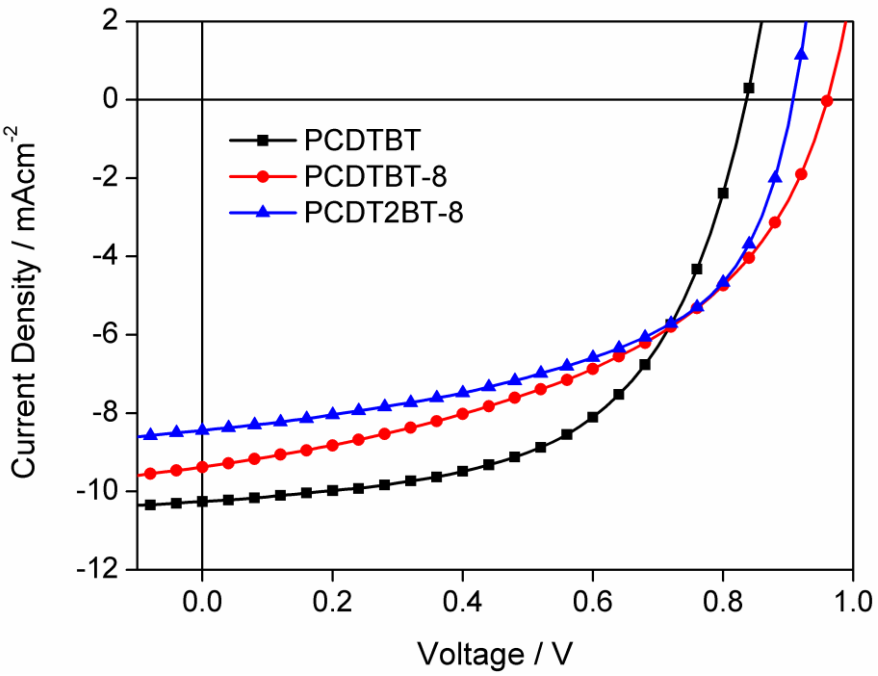

Figure 5.7 J-V characteristics of optimised devices with device metrics in Table 5.2 (indicated by [a]). All devices utilised a PEDOT:PSS anode buffer layer and a composite cathode of Ca/Al.

5.6 – Conclusion

In summary, two polymers with soluble sidegroups on the BT unit were synthesised and used in bulk heterojunction solar cells. The introduction of octyloxy substituents on the BT unit causes an increase in the optical energy gap and therefore a reduced electronic delocalisation, whereas the inclusion of additional thiophene moieties along the polymer backbone red-shifts the absorption (reducing the optical energy gap) which leads to an increased electronic delocalisation. This is due to the octyloxy sidegroups reducing the electron accepting capabilities of the BT unit, and the extra thiophene rings improving the electron donating abilities of the donor repeat units along the polymer backbone.

The octyloxy substituents dramatically increase the polymer solubility, with an upper solubility limit (taken from the onset of the formation of a turbid solution) of 20 mg/ml for PCDTBT-8 in $CHCl_3$ (compared with 1 mg/ml for PCDTBT). The additional side-chains on the BT unit cause an increase in the solution entropy as well as separate the polymer chains. However, additional thiophene rings along the polymer backbone result in a decreased solubility limit (~ 1 mg/ml). Although polymeric aggregates were not formed, a turbid solution was seen from low concentrations which are likely due to the lack of solubilising side-groups on the thiophene units which is typically used for polymers like P3HT.

The optimisation of bulk heterojunction solar cells consisted of varying the casting solvent, blend ratio (with the fullerene $PC_{70}BM$), active layer thickness and thermal annealing temperature. A thermal annealing treatment was found to be necessary to optimise BT-8 based polymer OPV efficiency, with values > 4% achieved. An annealing temperature of 120°C for PCDTBT-8 resulted in an optimised PCE of 4.22%, with a J_{sc} of -9.38 $mAcm^{-2}$, V_{oc} of 0.96 V and FF of 46.9%. PCDT2BT-8 required a slightly lower annealing temperature of 110°C, allowing a PCE of 4.12 % to be obtained with a J_{sc} of -8.44 $mAcm^{-2}$, V_{oc} of 0.90 V, and FF of 54.2%. Despite both polymers having a deep-lying HOMO energy level, PCEs were not dramatically enhanced upon the substitution of PEDOT:PSS with thermally evaporated MoO_x (as seen in Section 4.2). Efficiencies for PCDTBT-8 devices were improved to 4.4% through a small increase in the FF.

Hole mobilities obtained in unannealed films as measured using an OFET technique gave values for PCDT2BT-8 of 2.7 x 10^{-3} $cm^2V^{-1}s^{-1}$. This is higher than that for the other two polymers studied which is likely to result from a greater degree of backbone rigidity upon inclusion of the additional thiophene moieties.

The improved solution preparation from the inclusion of octyloxy substituents will be used in the following chapter. This will be combined with a study in which thiophene is replaced with selenophene to further red-shift polymer absorption spectra to attempt to improve the ability of the devices to harvest more sunlight and improve OPV efficiency.

References

1. E. Bundgaard, F.C. Krebs, Low band gap polymers for organic photovoltaics, *Sol. Energ. Mat. Sol C.*, **2007**, *91*, 954-985
2. J. Chen, Y. Cao, Development of novel conjugated donor polymers for high-efficiency bulk-heterojunction photovoltaic devices, *Acc. Chem. Res.*, **2009**, *42*, 1709-1718
3. Y.-J. Cheng, S.-H. Yang, C.-S. Hsu, Synthesis of conjugated polymers for organic solar cell applications, *Chem. Rev.*, **2009**, *109*, 5868-5923
4. S. Beaupré, P.-L.T. Boudreault, M. Leclerc, Solar-energy production and energy-efficient lighting: photovoltaic devices and white-light-emitting diodes using poly(2,7-fluorene), poly(2,7-carbazole), and poly(2,7-dibenzosilole) derivatives, *Adv. Mater.*, **2010**, *22*, E6-E27

5. C.L. Chochos, S.A. Choulis, How the structural deviations on the backbone of conjugated polymers influence their optoelectronic properties and photovoltaic performance, *Prog. Polym. Sci.*, **2011**, *36*, 1326-1414
6. H. Zhou, L. Yang, W. You, Rational design of high performance conjugated polymers for organic solar cells, *Macromolecules*, **2012**, *45*, 607-632
7. R.S. Kularatne, H.D. Magurudeniya, P. Sista, M.C. Biewer, M.C. Stefan, Donor–acceptor semiconducting polymers for organic solar cells, *J. Polym. Sci. A Polym. Chem.*, **2013**, *51*, 743-768
8. Z.-G. Zhang, J. Wang, Structures and properties of conjugated donor–acceptor copolymers for solar cell applications, *J. Mater. Chem.*, **2012**, *22*, 4178-4187
9. P. Ding, C.-C. Chu, B. Liu, B. Peng, Y. Zou, Y. He, K. Zhou, C.-S. Hsu, A high-mobility low-bandgap copolymer for efficient solar cells, *Macromol. Chem. Phys.*, **2010**, *211*, 2555-2561
10. P. Ding, C.-C. Chu, Y. Zou, D. Xiao, C. Pan, C.-S. Hsu, New low bandgap conjugated polymer derived from 2, 7-carbazole and 5, 6-bis(octyloxy)-4, 7-di(thiophen-2-yl) benzothiadiazole: synthesis and photovoltaic properties, *J. Appl. Polym. Sci.*, **2012**, *123*, 99-107
11. Y. Huang, M. Zhang, Y. Jing, H. Fan, X. Guo, Y. Li, Synthesis and photovoltaic properties of a donor-acceptor copolymer of dithienosilole and 5,6-bis(octyloxy)benzo[1,2,5]thiadiazole, *Macromol. Chem. Phys.*, **2012**, *213*, 2529-2535

12. M.S. Almeataq, H. Yi, S. Al-Faifi, A.A.B. Alghamdi, A. Iraqi, N.W. Scarratt, T. Wang, D.G. Lidzey, Anthracene-based donor–acceptor low band gap polymers for application in solar cells, *Chem. Commun.*, **2013**, *49*, 2252-2254
13. P. Ding, C. Zhong, Y. Zou, C. Pan, H. Wu, Y. Cao, 5,6-bis(decyloxy)-2,1,3-benzooxadiazole-based polymers with different electron donors for bulk-heterojunction solar cells, *J. Phys. Chem. C*, **2011**, *115*, 16211-16219
14. J. Sun, Y. Zhu, X. Xu, L. Lan, L. Zhang, P. Cai, J. Chen, J. Peng, Y. Cao, High efficiency and high V_{oc} inverted polymer solar cells based on a low-lying HOMO polycarbazole donor and a hydrophilic polycarbazole interlayer on ITO cathode, *J. Phys. Chem. C*, **2012**, *116*, 14188-14198
15. M. Helgesen, S.A. Gevorgyan, F.C. Krebs, R.A.J. Janssen, Substituted 2,1,3-benzothiadiazole- and thiophene-based polymers for solar cells – introducing a new thermocleavable precursor, *Chem. Mater.*, **2009**, *21*, 4669-4675
16. E. Wang, M. Wang, L. Wang, C. Duan, J. Zhang, W. Cai, C. He, H. Wu, Y. Cao, Donor polymers containing benzothiadiazole and four thiophene rings in their repeating units with improved photovoltaic performance, *Macromolecules*, **2009**, *42*, 4410-4415
17. Z. Chen, J. Fang, F. Gao, T.J.K. Brenner, K.K. Banger, X. Wang, W.T.S. Huck, H. Sirringhaus, Enhanced charge transport by incorporating additional thiophene units in the poly(fluorene-thienyl-benzothiadiazole) polymer, *Org. Electron.*, **2011**, *12*, 461-471

18. J.-H. Kim, H.U. Kim, D. Mi, S.-H. Jin, W.S. Shin, S.C. Yoon, I.-N. Kang, D.-H. Hwang, Introduction of perylene units for enhanced interchain interaction in conjugated polymers for organic photovoltaic devices, *Macromolecules*, **2012**, *45*, 2367-2376
19. J. Lu, F. Liang, N. Drolet, J. Ding, Y. Tao, R. Movileanu, Crystalline low band-gap alternating indolocarbazole and benzothiadiazole-cored oligothiophene copolymer for organic solar cell applications, *Chem. Commun.*, **2008**, 5315-5317
20. E. Zhou, S. Yamakawa, Y. Zhang, K. Tajima, C. Yang, K. Hashimoto, Indolo[3,2-b]carbazole-based alternating donor–acceptor copolymers: synthesis, properties and photovoltaic application, *J. Mater. Chem.*, **2009**, *19*, 7730-7737
21. S.-H. Chan, C.-P. Chen, T.-C. Chao, C. Ting, C.-S. Lin, B.-T. Ko, Synthesis, characterization, and photovoltaic properties of novel semiconducting polymers with thiophene-phenylene-thiophene (TPT) as coplanar units, *Macromolecules*, **2008**, *41*, 5519-5526
22. C.-P. Chen, S.-H. Chan, T.-C. Chao, C. Ting, B.-T. Ko, Low-bandgap poly(thiophene-phenylene-thiophene) derivatives with broaden absorption spectra for use in high-performance bulk-heterojunction polymer solar cells, *J. Am. Chem. Soc.*, **2008**, *130*, 12828-12833
23. A. Tsami, T.W. Bünnagel, T. Farrell, M. Scharber, S.A. Choulis, C.J. Brabec, U. Scherf, Alternating quinoxaline/oligothiophene copolymers – synthesis and unexpected absorption properties, *J. Mater. Chem.*, **2007**, *17*, 1353-1355

24. T. Wang, A.J. Pearson, A.D.F. Dunbar, P.A. Staniec, D.C. Watters, H. Yi, A.J. Ryan, R.A.L. Jones, A. Iraqi, D.G. Lidzey, Correlating structure with function in thermally annealed PCDTBT:$PC_{70}BM$ photovoltaic blends, *Adv. Funct. Mater.*, **2012**, *22*, 1399-1408
25. W. Ma, C. Yang, X. Gong, K. Lee, A.J. Heeger, Thermally stable, efficient polymer solar cells with nanoscale control of the interpenetrating network morphology, *Adv. Funct. Mater.*, **2005**, *15*, 1617-1622
26. G. Li, V. Shrotriya, J. Huang, Y. Yao, T. Moriarty, K. Emery, Y. Yang, High-efficiency solution processable polymer photovoltaic cells by self-organization of polymer blends, *Nat. Mater.*, **2005**, *4*, 864-868
27. K.-H. Ong, S.-L. Lim, H.-S. Tan, H.-K. Wong, J. Li, Z. Ma, L.C.H. Moh, S.-H. Lim, J.C. de Mello, Z.-K. Chen, A versatile low bandgap polymer for air-stable, high-mobility field-effect transistors and efficient polymer solar cells, *Adv. Mater.*, **2011**, *23*, 1409-1413
28. R. Qin, W. Li, C. Li, C. Du, C. Veit, H.-F. Schleiermacher, M. Andersson, Z. Bo, Z. Liu, O. Inganäs, U. Wuerfel, F. Zhang, A planar copolymer for high efficiency polymer solar cells, *J. Am. Chem. Soc.*, **2009**, *131*, 14612-14613
29. B.C. Thompson, J.M.J. Fréchet, Polymer-fullerene composite solar cells, *Angew. Chem. Int. Edit.*, **2008**, *47*, 58-77
30. C.H. Peters, I.T. Sachs-Quintana, W.R. Mateker, T. Heumueller, J. Rivnay, R. Noriega, Z.M. Beiley, E.T. Hoke, A. Salleo, M.D. McGehee, The mechanism of burn-in loss in a high efficiency polymer solar cell, *Adv. Mater.*, **2012**, *24*, 663-668

Chapter 6

Effect of replacing thiophene with selenophene in PCDTBT and its derivatives

The previous chapter presented two polymers based on PCDTBT having the inclusion of octyloxy side-groups on the BT unit which improved polymer solubility while maintaining a high device performance. The addition of extra thiophene repeat units along the polymer backbone was also shown to reduce the optical energy gap. In this chapter, the sulphur heteroatom in the thiophene units is replaced with selenium (to give a selenophene moiety) to lower the optical energy gap which consequently allows a greater overlap with the solar spectrum to be gained. Comparison of the effects of substituting selenium into PCDTBT and PCDTBT-8 (from Chapter 5), as well as fluorene derivatives, will be investigated with their optical and electronic properties being presented.

6.1 – Introduction

Thiophene repeat units have been widely explored in OFET and OPV donor materials courtesy of their electron-donating characteristics. Most notably, P3HT has been used to create OPV devices with efficiencies of greater than 5% [1]. Following this, a variety of high performing donor polymers have been synthesised having thiophene moieties along their backbone. Co-polymers have included thiophene units as a spacer between the "donor" and "acceptor" components, such as those containing the benzothiadiazole "acceptor" unit [2-8], to enhance the optical and electronic properties.

As a result of polymer synthesis, these thiophene units can be modified to fine-tune polymer properties. A direct replacement of the sulphur heteroatom in a thiophene repeat unit is possible as long as conjugation is

maintained. This can be easily achieved by using a different atom from Group 16 in the periodic table (for example oxygen or selenium). The result of this substitution can have a direct influence on the resultant polymer absorption. Selenophene moieties (whereby the sulphur heteroatom in a thiophene is replaced with selenium) are more electron-rich than thiophene; a property that consequently increases the electronic delocalisation of the polymer, leading to a reduced optical energy gap and thus a red-shift of polymer absorption. This effect has been observed in P3HT based polymers such as P3HS [9], as well as many other polymer systems [10-15]. Further advantages of selenophene over thiophene repeat units include greater rigidity and stronger intermolecular interactions which may aid charge carrier mobility [16-17]. Despite such potential benefits, the majority of studies on these materials have not evidenced significant improvements in OPV efficiency. An exception to this comes from a study in which OPV efficiencies of 6.87% were observed; a result of a high J_{sc} value of -16.8 $mAcm^{-2}$ [18].

Fluorene-based polymers have also been used in OPV devices due to their good solubility and chemical and thermal stability [19-25]. However, device efficiency has been limited to ~ 4.5% due to low FF and charge carrier mobility [26]. Section 7.1 provides more detail regarding fluorene-based polymers. Carbazole units have, as presented in Chapters 4 and 5, been shown to achieve PCEs in excess of 7% [27-28] in OPV devices. Both selenophene and fluorene units are explored (as the donor component) in

this chapter to determine the effect of such chemical substitution with the aim of the work being to improve device efficiency.

Figure 6.1 summarises the donor and acceptor moieties investigated in this chapter. Note that the thiophene units and the sidegroups on the BT unit are modified to create selenophene and octyloxy containing polymers respectively. The full structure of each polymer is shown in Section 2.10.

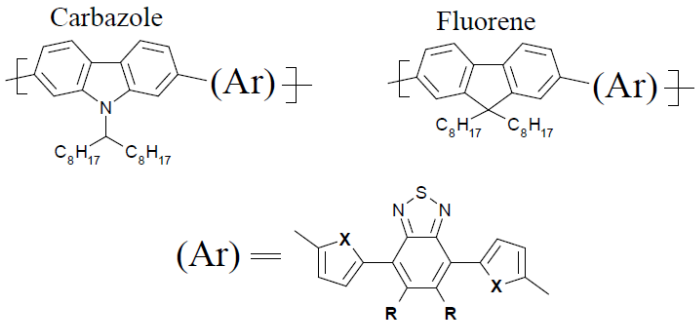

PCDTBT : Carbazole, X=S, R=H
PCDSeBT : Carbazole, X=Se, R=H
PFDTBT : Fluorene, X=S, R=H
PFDSeBT : Fluorene, X=Se, R=H
PCDTBT-8 : Carbazole, X=S, R=OC_8H_{17}
PCDSeBT-8 : Carbazole, X=Se, R=OC_8H_{17}
PFDTBT-8 : Fluorene, X=S, R=OC_8H_{17}
PFDSeBT-8 : Fluorene, X=Se, R=OC_8H_{17}

Figure 6.1 Comparison of all the polymer chemical structures. For full structure of each polymer, refer to Section 2.10.

It is worth noting that some of the polymers presented in this chapter have previously been reported in the literature (PCDTBT, PFDTBT, PCDTBT-8, PCDSeBT, PFDSeBT and PFDTBT-8). References regarding previous studies on PCDTBT have been provided in Chapter 4, and those on PCDTBT-8 provided in Chapter 5. Fluorene-based polymers, including PFDTBT and its derivatives, were discussed above (also see Section 7.1).

The selenium version of PCDTBT, i.e. PCDSeBT, has been observed to increase device efficiency, compared with its thiophene equivalent, with a PCE of 4.12% reported [10]. However, in that same study the thiophene reference (PCDTBT) provided lower efficiencies compared with that reported from other groups, as well as those presented in Chapters 4 and 5. PFDSeBT has also been previously utilised in OPV devices and was referred to as PFO-SeBT [29]. In this report, PCEs of PFO-SeBT were restricted to 1% due to poor J_{sc} and FF values, despite varying the ratio of the co-monomers along the donor polymer backbone. Previous work on the polymer PFDTBT-8 reported OPV efficiencies of 3.1% [30]. The low J_{sc} achieved however prevented this polymer from achieving the high performances demonstrated in Section 6.4.

6.2 – UV-Vis spectroscopy and energy levels

The thin film absorption spectra of the polymers are shown in Figure 6.2 (part (a) for BT- and (b) for BT-8 based polymers) with peak absorption wavelengths (both in thin films and in $CHCl_3$ solution) and optical energy gaps summarised in Table 6.1 and Figure 6.3 part (a). It is evident that replacing the thiophene repeat units with selenophene results in a red-shift in the optical absorption (consistent with reports outlined above). This results in the Se-based polymers exhibiting a reduced optical energy gap and therefore a greater electronic delocalisation; a property consistent with the selenium heteroatom being more electron-rich. However, this trend is not observed for the polymers PFDTBT and PFDSeBT where the latter has, in fact, a blue-shifted thin film absorption peak and a similar optical energy

gap. This effect could be attributed to a higher degree of aggregation in PFDTBT thin films as the absorption peak in solution is much lower than PFDSeBT (549 *vs*. 575 nm respectively).

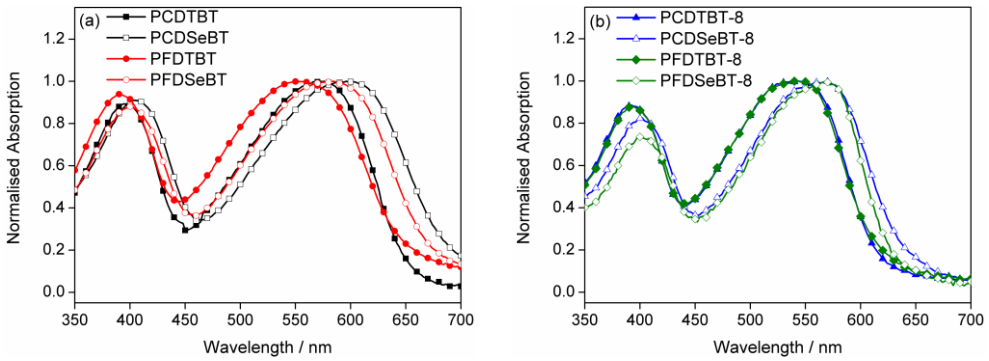

Figure 6.2 Normalised thin film absorption spectra for (a) BT-based polymers and (b) for BT-8.

Polymer	λ_{max} / nm Thin film ($CHCl_3$ Solution)	E_g^{op} / eV	HOMO / eV	LUMO / eV	E_g^{elec} / eV
PCDTBT	396 (392) / 570 (547)	1.88	-5.35	-3.42	1.93
PCDSeBT	404 (404) / 596 (584)	1.82	-5.46	-3.25	2.21
PFDTBT	408 (393) / 592 (549)	1.86	-5.34	-3.44	1.90
PFDSeBT	399 (400) / 571 (575)	1.86	-5.42	-3.25	2.17
PCDTBT-8	391 (384) / 536 (513)	1.98	-5.40	-3.27	2.13
PCDSeBT-8	399 (393) / 555 (540)	1.94	-5.47	-3.09	2.38
PFDTBT-8	391 (388) / 544 (518)	1.98	-5.44	-3.32	2.12
PFDSeBT-8	411 (398) / 599 (548)	1.87	-5.47	-3.12	2.35

Table 6.1 UV-Vis, optical and electrical energy gap, as well as the energy levels for all polymers. Data acquired by Hunan Yi, Abdulaziz Alghamdi and Solyman Al-Faifi from the Chemistry department.

Similar effects to those reported in Section 5.2 can be seen by comparing the BT and BT-8 equivalents; i.e. a blue-shifted absorption upon including octyloxy side chains resulting in a larger optical energy gap. This is due to the functionalised BT unit having a reduced electron accepting capability. Replacing the carbazole with fluorene generally results in a red-shift in peak absorption wavelength as well as a decreased E_g^{op}, although the opposite is true for PFDSeBT and PCDSeBT where the carbazole polymer has a red-shifted peak value: 571 and 590 nm respectively.

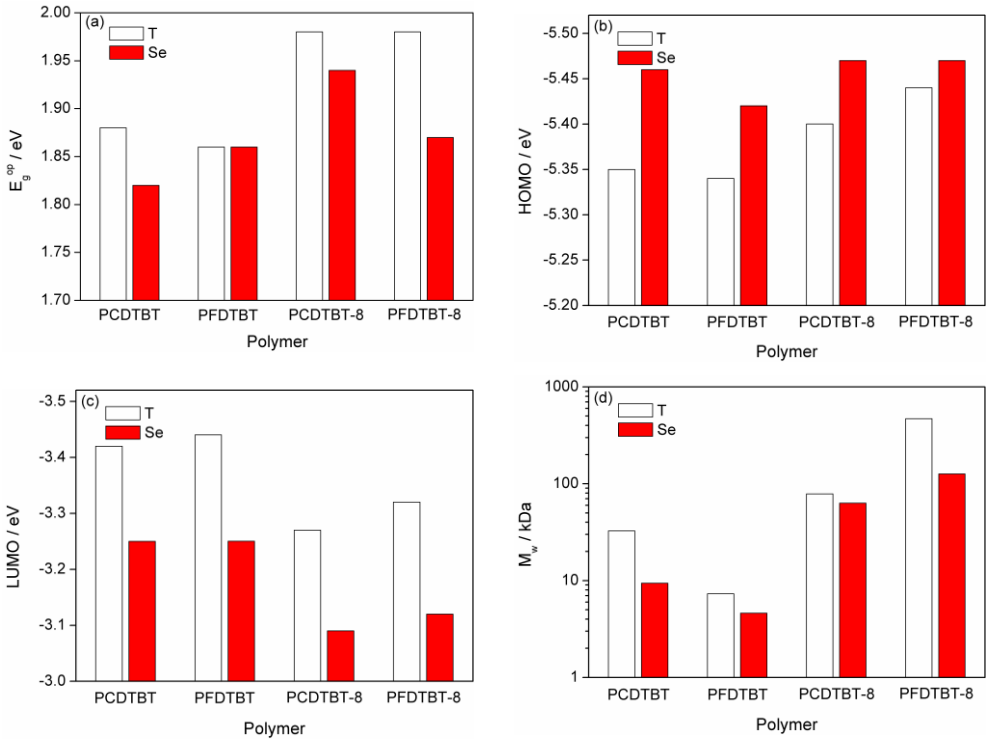

Figure 6.3 Graphical comparison of thiophene and selenophene polymers. Part (a) shows the optical energy gap E_g^{op}. The HOMO and LUMO energy levels are shown in parts (b) and (c) respectively. Part (d) shows the molecular weight M_w. In every case the generic thiophene polymer name is indicated on the x-axis. Note that part (d) is in logarithmic scale.

The HOMO and LUMO energy levels of the polymers are also shown in Table 6.1 and Figure 6.3 part (b) and (c) respectively. It is apparent that the HOMO energy levels are slightly deeper for all selenophene polymers. This could be a result of the small difference in the electronegativity between sulphur and selenium as well as their differences in electron donating capabilities [31]. Interestingly, the observed LUMO energy levels (determined from CV) of the selenophene polymers are closer to the vacuum level, leading to a larger electrical energy gap, despite having a smaller optical energy gap. Note that the electrical energy gap, E_g^{elec}, (i.e. the difference between the HOMO and LUMO energy levels) differs from the optical energy gap as E_g^{elec} takes into consideration the binding energy of an exciton.

Upon the inclusion of octyloxy side-chains (for both thiophene and selenophene polymers), a similar pattern is seen as previously detailed in Section 5.3 for PCDTBT and PCDTBT-8; the HOMO energy level deepens while the LUMO approaches the vacuum level. Here, both effects are due to the reduced electron accepting capabilities upon functionalising octyloxy sidegroups on the BT unit. No similar trend is however apparent when comparing carbazole and fluorene based polymers.

6.3 – Molecular weight

Table 6.2 reports the number-average molecular weight (M_n), molecular weight (M_w) and synthesis yield for all polymers. Figure 6.3 part (d) compares the M_w for all polymers. Replacing the sulphur heteroatom with

selenium results in the lowering of the M_w, which could be due to lower polymer solubility. This is also observed from their synthesis yields with Se-based polymers having a reduced value. This is particularly evident in the case of PCDTBT and PCDSeBT (73 and 30% respectively). The inclusion of octyloxy substituents on the BT unit provides polymers with higher solubilities. This is identifiable from the enhanced M_w (values exceeding 60.0 kDa) as well as the synthesis yields with both Se-polymers PCDSeBT-8 and PFDSeBT-8 displaying yields of 60% or higher.

Polymer	M_n / kDa	M_w / kDa	Yield / %
PCDTBT	22.5	32.6	73 [(a),(b)]
PCDSeBT	3.9	9.4	30
PFDTBT	5.3	7.3	19
PFDSeBT	1.9	4.6	27.9
PCDTBT-8	32.8	78.6	95 [(b)]
PCDSeBT-8	26.0	62.9	60
PFDTBT-8	78.4	468.7	14 [(a)]
PFDSeBT-8	54.2	126.0	74

Table 6.2 GPC and synthesis yield for all polymers. Polymers were from a toluene Soxhlet fraction unless stated otherwise. [(a)] Chloroform fraction, [(b)] values taken from ref 32. Data provided by Hunan Yi, Abdulaziz Alghamdi and Solyman Al-Faifi from the Chemistry department.

It is worth noting that the fluorene-based polymers without octyloxy sidegroups exhibited a lower M_w than their carbazole equivalents. This is a consequence of the polymer solubility which is identifiable from the

differing yields, < 20% and 73% for PFDTBT and PCDTBT respectively. However, if BT is replaced with BT-8, it is found that the fluorene-based polymers have a molecular weight greater than 100.0 kDa and yields > 70% (note that the toluene fraction of PFDTBT-8 presented a synthesis yield of 77.7%). Clearly the introduction of octyloxy sidegroups enhance the solubility and allow a greater distance between polymer chains in solution and in thin films (as concluded in Section 5.4 and verified later in Section 6.4.2).

6.4 – Device optimisation

As shown in the previous chapters, device efficiency is greatly dependent on the choice of casting solvent, blend ratio and thermal annealing temperature. It is worth emphasising however that only a relatively limited device optimisation programme was possible due to only small quantities of each Se-based polymer being available. Because of this, a number of processes could not be examined, including the effect of solvent additive, thermal/solvent annealing and replacing the PEDOT:PSS anode buffer layer with a metal oxide. However, for all polymers, the effect of solvent and blend ratio was examined. All polymers were also subjected to a thermal annealing temperature of 80°C although most, as indicated in Table 6.3, did not benefit from such a process step. The device metrics for all polymers are compared in Figure 6.4.

Results from the optimisation process are displayed in Table 6.3 with the equivalent polymers containing thiophene and selenophene gathered together for sake of comparison. It can be seen that for most polymers (with the exception of PCDSeBT-8), selenophene-based devices are less efficient than those based on the equivalent sulphur containing polymers and have a PCE that is 30% lower on average. A noticeable trend is that the optimised Se-based devices necessitate the use of a thinner active layer thickness with the peak efficiencies being obtained from a thickness 10-20 nm thinner than their equivalent thiophene-counterparts. As we show later, this is a consequence of the lower hole mobility of selenophene polymers. This reduces device J_{sc}, with the other device metrics (FF and V_{oc}) showing only a small decrease when thiophene is substituted with selenophene, although these lower values continue to affect the overall efficiencies. These effects are evident in J-V characteristics as shown in Figure 6.5 where part (a) is for the BT-based polymers and (b) for those based on BT-8.

Polymer	Solvent	Blend Ratio	Thickness / nm	J_{sc} / $mAcm^{-2}$	V_{oc} / V	FF / %	PCE / %
PCDTBT	CB	1:4	70	-9.91	0.89	62.64	5.53 [(a),(b)]
PCDSeBT	$CHCl_3$	1:3	60	-6.62	0.85	59.20	3.34
PFDTBT	$CHCl_3$	1:4	70	-9.66	1.03	54.74	5.41
PFDSeBT	$CHCl_3$	1:3	50	-8.08	0.97	51.48	4.03
PCDTBT-8	CB	1:4	72	-9.39	0.96	48.90	4.41 [(a),(c)]
PCDSeBT-8	CB	1:4	60	-10.28	0.92	46.01	4.35
PFDTBT-8	CB	1:4	70	-10.22	1.02	47.57	4.94 [(b)]
PFDSeBT-8	DCB	1:4	50	-8.23	0.99	42.22	3.45

Table 6.3 Optimised device metrics for all polymers with thiophene-selenophene pairs grouped together. All polymers were blended with $PC_{70}BM$ and a PEDOT:PSS anode buffer was utilised except [(a)] which used thermally evaporated MoO_x. [(b)] These devices were thermally annealed at 80ºC, [(c)] annealed at 120 ºC, for 15-30 mins.

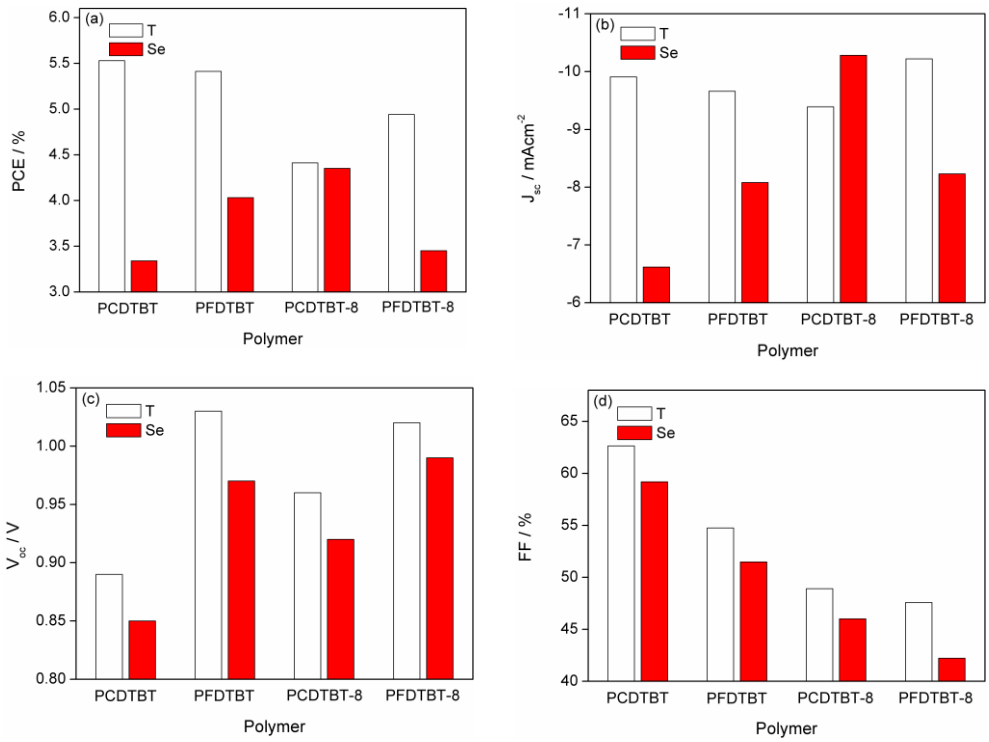

Figure 6.4 Optimised device metrics for thiophene and selenophene polymers, whose values are shown in Table 6.3. Part (a) shows the PCE, (b) the Jsc, (c) the Voc, and (d) the FF. In each case the generic thiophene polymer name is detailed on the x-axis.

Despite small differences in their HOMO energy levels, the fluorene polymers displayed higher V_{oc} values (with an increase of up to 0.14 V) compared to their carbazole analogues. These fluorene device PCEs were however limited by their lower FF values. Nevertheless, fluorene-based devices were capable of producing similar or higher efficiencies than those achieved from carbazole devices. The only exception is the polymer PFDSeBT-8 which had one of the lowest recorded PCE values, due to its low J_{sc} and FF. This is due to PFDSeBT-8 having a lower molar absorptivity than the other polymers, see Table 6.4.

As seen in Section 5.5, the inclusion of octyloxy substituents leads to improved V_{oc} values in optimised devices. This result is also observed here possibly due to deeper HOMO energy levels, with the largest increases obtained from the carbazole-based polymers. It is apparent however that BT-8 based devices have reduced FF values.

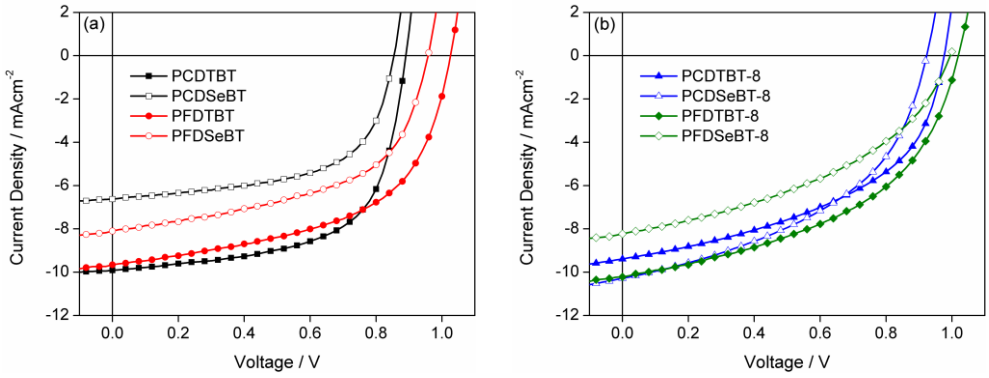

Figure 6.5 J-V characteristics of the optimised devices for (a) BT and (b) BT-8 based polymers. Device metrics provided in Table 6.3.

6.4.1 Photoluminescence quantum yield and molar absorption coefficient

The photoluminescence quantum yield (PLQY, see Section 3.5) of pristine selenophene polymer thin films (spun from their optimised device casting solvent) was lower compared to their thiophene analogues, and is summarised in Table 6.4 and Figure 6.6 part (a). The results clearly demonstrate that the Se-polymers have a significantly lower PLQY. This suggests that the singlet-exciton population available for dissociation has been reduced, potentially influencing the performance of devices. This reduced efficiency may possibly be due to increased intersystem crossings

to lower lying triplet states; a consequence anticipated as a result of the heavy atom effect of selenium [29].

Polymer	PLQY / %	ε / $Lmol^{-1}cm^{-1}$	μ / $cm^{-2}V^{-1}s^{-1}$	d-spacing / Å
PCDTBT	7.30	39,330	6.11×10^{-4}	4.00 ± 0.02
PCDSeBT	0.55	36,000	5.08×10^{-5}	4.19 ± 0.03
PFDTBT	7.30	38,080	1.82×10^{-3}	4.03 ± 0.02
PFDSeBT	0.96	33,230	6.05×10^{-4}	4.16 ± 0.02
PCDTBT-8	11.60	42,310	4.43×10^{-4}	4.22 ± 0.03
PCDSeBT-8	1.50	49,666	3.36×10^{-4}	4.16 ± 0.02
PFDTBT-8	7.20	35,740	4.63×10^{-4}	4.13 ± 0.02
PFDSeBT-8	2.70	23,200	1.04×10^{-4}	4.22 ± 0.03

Table 6.4 Photoluminescence quantum yield, molar absorption coefficient (ε), OFET hole mobility (μ) and d-spacing for all polymers. Each polymer was spun from their optimised device solvent with no thermal annealing. Molar absorption coefficient data was provided by Mohammed Almeataq from the Chemistry department.

The solution molar absorption coefficient (ε) is also displayed in Table 6.4 (and compared in Figure 6.6 part (b)) and was measured to quantify the intrinsic absorption properties of the polymers. It can be seen that the selenophene polymers generally have a lower molar absorption coefficient which, when also combined with a thinner optimised active layer thickness, leads to a reduced charge generation efficiency despite their lower optical energy gaps. Interestingly, the only exception is PCDSeBT-8 which has the

highest molar absorptivity of all polymers studied; a result that may explain the large J_{sc} observed in devices despite the use of a thin active layer thickness of ~ 60 nm.

In general however, if we compare the carbazole and fluorene polymers, it can be seen that ε is larger in thiophene polymers, and is also more pronounced in the BT-8 substituted polymers. In particular, polymers PFDSeBT and PFDSeBT-8 exhibit the two lowest ε values which correlates with their poor J_{sc} values. We believe that the poor light harvesting properties of these polymers contributes in a significant way to their poor efficiency when made into an OPV device.

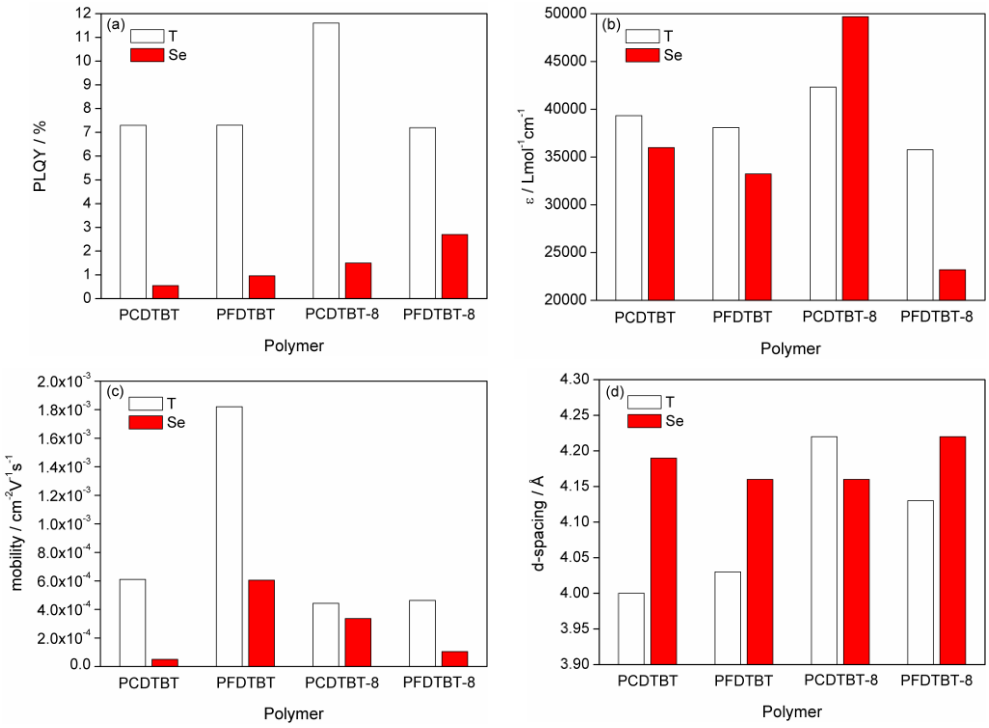

Figure 6.6 Comparison of (a) PLQY, (b) the molar absorption coefficient ε, (c) hole mobility μ, and (d) the d-spacing for the thiophene and selenophene polymers. In all cases, the generic thiophene name of the polymer is shown on the x-axis.

6.4.2 OFET mobility and GIWAXS

Hole mobilities (μ), as determined from OFET measurements, are presented in Table 6.4 and Figure 6.6 part (c). It is evident that all the thiophene polymers exhibit higher values than their selenophene equivalents. Polymer PCDSeBT-8 displayed a hole mobility similar to its thiophene counterpart. Notably, devices utilising this polymer obtained a PCE similar to those based on PCDTBT-8.

It can be seen that the mobility of PCDSeBT presented here is much lower (~ 1 order of magnitude) than that reported in ref. 10 (5.08 x 10^{-5} *vs*. 5.10 x 10^{-4} $cm^{-2}V^{-1}s^{-1}$ for as-cast films). The processing conditions were different through the choice of casting solvent (independently optimised), most certainly leading to differing morphologies that consequently influence the resulting mobility. The large difference in M_w of the polymers (9.4 *vs.* 208.3 kDa) is also likely to have a significant affect. To investigate this, measurements were taken from two fractions of PCDTBT-8 (in which the M_w differed by ~ 2.5 times). Here, we found that the larger M_w polymer had a mobility of 4.50 x 10^{-4} $cm^2V^{-1}s^{-1}$ compared to the lower M_w version that had a mobility of 3.41 x 10^{-5}. This suggests that the higher molecular weight fraction is able to facilitate intramolecular transport over longer distances.

These lower hole mobility values correlate with the reduced efficiencies obtained from most of the selenophene-based polymers. To further explore this effect, grazing incident wide-angle x-ray scattering (GIWAXS) was used to compare the molecular packing of the polymers. All thin films were prepared under identical conditions using a solvent determined by OPV device optimisation.

The d-spacing for each polymer, as reported in Table 6.4 and compared in Figure 6.6 part (d), reveals that the selenophene moieties generally increase the π-π stacking distances, perhaps due to the larger radius of the selenium atom. As was determined for polymers containing BT-8 (see Section 5.4), these materials have larger π-π distances.

6.4.3 – Thin film photostability

To determine any differences in photostability, pristine polymer thin films were spin-cast from their respective optimised casting solvent and absorption spectra were measured before the films were exposed to light from a solar simulator for ~ 30 mins in air. Absorption spectra of the thin films were then taken under the same conditions as the initial measurements.

The UV-Vis absorption spectra recorded before and after light exposure are shown in Figure 6.7, with each part detailing common materials that were either based on thiophene or selenophene. Note that the spectra are normalised to the absorption peak recorded before light exposure. It is evident that there is a larger reduction in the peak absorption of the selenophene materials compared to those based on thiophene. Notably, PFDTBT displayed only minimal changes possibly thanks to the thermal and chemical stability of fluorene. In general, we find that the selenophene absorption reduced by 15-96% as a result of light exposure, whereas the thiophene polymer absorption was reduced by 1-13%. The most noticeable reduction was seen from PFDSeBT-8, in which its absorption band almost completely disappeared after light exposure. Indeed, the light exposed PFDSeBT-8 thin film could not be seen by eye. Interestingly, the peak reduction is also more pronounced in polymers containing octyloxy substituents (both thiophene and selenophene).

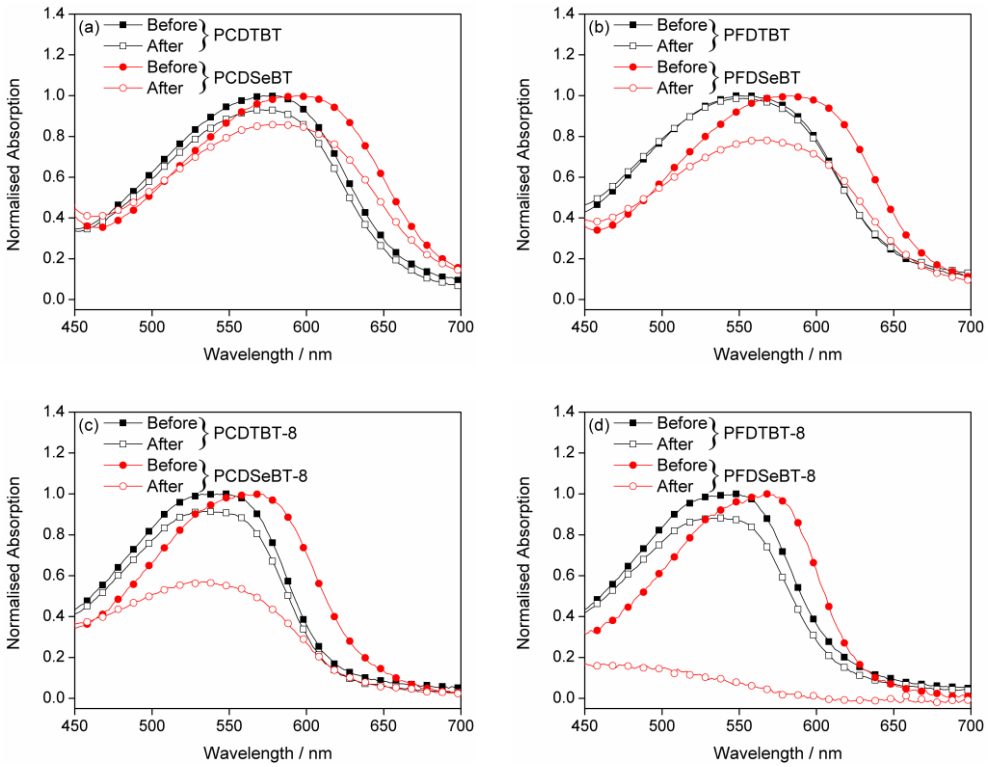

Figure 6.7 Normalised UV-Vis of before and after photo-degradation of (a) PCDTBT and PCDSeBT, (b) PFDTBT and PFDSeBT, (c) PCDTBT-8 and PCDSeBT-8, and (d) PFDTBT-8 and PFDSeBT-8.

Another noticeable consequence is that the absorption peak blue-shifts after photobleaching (excluding PFDSeBT-8 where no peak could be seen). This is most likely a result of a decrease in electronic delocalisation caused by chemical degradation. This effect is more pronounced in the selenophene based polymers. The cause for such reduced photostability in the Se-based polymers could be due to the presence of triplet states (as predicted earlier from the PLQY results) since such states have a longer lifetime than singlet states. Photo-degradation could therefore be more significant in polymers having such long living excited states. Although the photostability of these Se-polymers appears to be worse than their thiophene counterparts, the

opposite finding has been made in a comparison of P3HT *vs.* P3HS [9]. It is likely therefore that the photostability of selenium-based polymers is highly dependent on the overall polymer structure.

6.5 – Conclusion

In this chapter, derivatives of PCDTBT were presented which incorporated selenium instead of sulphur heteroatoms along the polymer backbone. The absorption spectra of these new polymers are red-shifted due to selenium having a smaller ionisation potential causing the optical energy gap to be smaller. The HOMO energy level was also observed to increase; a result due to the difference in electronegativity of the two heteroatoms as well as their differing electron donating capabilities.

The selenophene-based polymers were less efficient when fabricated in bulk heterojunction solar cells with the only exception being PCDSeBT-8. Such reductions were primarily due to lower J_{sc} values which we attribute to a lower molar absorption coefficient, as well as their reduced hole mobilities which therefore necessitated the use of a thinner active layer to maximise charge extraction efficiency. Fluorene based polymers were also relatively more efficient as a result of an enhanced V_{oc}. Functionalisation of the BT moiety was also explored, however OPV device efficiency was limited by relatively low FF.

The results from PLQY measurements suggest the potential existence of triplet states in Se-based polymers which deplete the singlet-exciton population and therefore limit charge generation efficiency in BHJ devices. Photostability also appears to be a more significant concern for the selenium polymers. The possible presence of triplet states (having longer lifetimes) may also increase the rate of photo-degradation in Se-based thin films. A greater reduction is also observed from octyloxy containing polymers.

The most promising Se-based polymer studied was PCDSeBT-8. This had a good hole mobility and a high molar absorption coefficient which allowed a high optimised power conversion efficiency of ~ 4.4% to be obtained with a J_{sc} value greater than its thiophene equivalent.

It is also clear that the fluorene-based polymers studied have enhanced V_{oc} and lower optical energy gaps making them promising materials for OPV devices. In the following chapter, we explore a new fluorene based polymer (PFDT2BT-8) and obtain significant improvements in OPV efficiency.

References

1. W. Ma, C. Yang, X. Gong, K. Lee, A.J. Heeger, Thermally stable, efficient polymer solar cells with nanoscale control of the interpenetrating network morphology, *Adv. Funct. Mater.*, **2005**, *15*, 1617-1622

2. A. Dhanabalan, J.K.J. van Duren, P.A. van Hal, J.L.J. van Dongen, R.A.J. Janssen, Synthesis and characterization of a low bandgap conjugated polymer for bulk heterojunction photovoltaic cells, *Adv. Funct. Mater.*, **2001**, *11*, 255-262
3. Q. Hou, Y. Xu, W. Yang, M. Yuan, J. Peng, Y. Cao, Novel red-emitting fluorene-based copolymers, *J. Mater. Chem.*, **2002**, *12*, 2887-2892
4. S. Admassiea, O. Inganäs, W. Mammo, E. Perzon, M.R. Andersson, Electrochemical and optical studies of the band gaps of alternating polyfluorene copolymers, *Synthetic Met.*, **2006**, *156*, 614-623
5. N. Blouin, A. Michaud, M. Leclerc, A low-bandgap poly(2,7-carbazole) derivative for use in high-performance solar cells, *Adv. Mater.*, **2007**, *19*, 2295-2300
6. E. Wang, L. Wang, L. Lan, C. Luo, W. Zhuang, J. Peng, Y. Cao, High-performance polymer heterojunction solar cells of a polysilafluorene derivative, *Appl. Phys. Lett.*, **2008**, *92*, 033307
7. E. Zhou, M. Nakamura, T. Nishizawa, Y. Zhang, Q. Wei, K. Tajima, C. Yang, K. Hashimoto, Synthesis and photovoltaic properties of a novel low band gap polymer based on N-substituted dithieno[3,2-b:2',3'-d]pyrrole, *Macromolecules*, **2008**, *41*, 8302-8305
8. H.-J. Song, D.-H. Kim, E.-J. Lee, S.-W. Heo, J.-Y. Lee, D.-K. Moon, Conjugated polymer consisting of quinacridone and benzothiadiazole as donor materials for organic photovoltaics: coplanar property of polymer backbone, *Macromolecules*, **2012**, *45*, 7815-7822
9. M. Heeney, W. Zhang, D.J. Crouch, M.L. Chabinyc, S. Gordeyev, R. Hamilton, S.J. Higgins, I. McCulloch, P.J. Skabara, D. Sparrowe, S.

Tierney, Regioregular poly(3-hexyl)selenophene: a low band gap organic hole transporting polymer, *Chem. Commun.*, **2007**, 5061-5063

10. B. Kim, H.R. Yeom, M.H. Yun, J.Y. Kim, C. Yang, A selenophene analogue of PCDTBT: selective fine-tuning of LUMO to lower of the bandgap for efficient polymer solar cells, *Macromolecules*, **2012**, *45*, 8658-8664
11. M. Shahid, R.S. Ashraf, Z. Huang, A.J. Kronemeijer, T. McCarthy-Ward, I. McCulloch, J.R. Durrant, H. Sirringhaus, M. Heeney, Photovoltaic and field effect transistor performance of selenophene and thiophene diketopyrrolopyrrole co-polymers with dithienothiophene, *J. Mater. Chem.*, **2012**, *22*, 12817-12823
12. A.J. Kronemeijer, E. Gili, M. Shahid, J. Rivnay, A. Salleo, M. Heeney, H. Sirringhaus, A selenophene-based low-bandgap donor-acceptor polymer leading to fast ambipolar logic, *Adv. Mater.*, **2012**, *24*, 1558-1565
13. H.-Y. Chen, S.-C. Yeh, C.-T. Chen, C.-T. Chen, Comparison of thiophene- and selenophene-bridged donor-acceptor low band-gap copolymers used in bulk-heterojunction organic photovoltaics, *J. Mater. Chem.*, **2012**, *22*, 21549-21559
14. W.-H. Lee, S.K. Son, K. Kim, S.K. Lee, W.S. Shin, S.-J. Moon, I.-N. Kang, Synthesis and characterization of new selenophene-based donor-acceptor low-bandgap polymers for organic photovoltaic cells, *Macromolecules*, **2012**, *45*, 1303-1312

15. L. Dou, W.-H. Chang, J. Gao, C.-C. Chen, J. You, Y. Yang, A selenium-substituted low-bandgap polymer with versatile photovoltaic applications, *Adv. Mater.*, **2013**, *25*, 825-831
16. S.S. Zade, N. Zamoshchik, M. Bendikov, Oligo- and polyselenophenes: a theoretical study, *Chem. Eur. J.*, **2009**, *15*, 8613-8624
17. A. Patra, M. Bendikov, Polyselenophenes, *J. Mater. Chem.*, **2010**, *20*, 422-433
18. H.A. Saadeh, L. Lu, F. He, J.E. Bullock, W. Wang, B. Carsten, L. Yu, Polyselenopheno[3,4-b]selenophene for highly efficient bulk heterojunction solar cells, *ACS Macro. Lett.*, **2012**, *1*, 361-365
19. Q. Pei, Y. Yang, Efficient photoluminescence and electroluminescence from a soluble polyfluorene, *J. Am. Chem. Soc.*, **1996**, *118*, 7416
20. G. Klärner, J.-I. Lee, M.H. Davey, R.D. Miller, Exciton migration and trapping in copolymers based on dialkylfluorenes, *Adv. Mater.*, **1999**, *11*, 115-119
21. M. Bernius, M. Inbasekaran, J. O'Brien, W. Wu, Progress with light-emitting polymers, *Adv. Mater.*, **2000**, *12*, 1737-1750
22. S. Setayesh, A.C. Grimsdale, T. Weil, V. Enkelmann, K. Müllen, F. Meghdadi, E.J.W. List, G. Leising, Polyfluorenes with polyphenylene dendron side chains: toward non-aggregating, light-emitting polymers, *J. Am. Chem. Soc.*, **2001**, *123*, 946-953
23. M. Bernius, M. Inbasekaran, E. Woo, W.S. Wu, L. Wujokwski, Fluorene-based polymers-preparation and applications, *J. Mater. Sci: Mater. Electron.*, **2002**, *11*, 111-116

24. W.-Y. Wong, Metallated molecular materials of fluorene derivatives and their analogues, *Coordin. Chem. Rev.*, **2005**, *9-10*, 971-997

25. H. Wang, J. Gao, W. Tong, Q. Qian, K. Lin, F. Liu, Copolymerization of 3,3'''-didodecylquaterthiophene with fluorene and silole units: improving photovoltaic performance by tuning energy levels, *Polym. Chem.*, **2012**, *3*, 2794-2800

26. M.-H. Chen, J. Hou, Z. Hong, G. Yang, S. Sista, L.-M. Chen, Y. Yang, Efficient polymer solar cells with thin active layers based on alternating polyfluorene copolymer/fullerene bulk heterojunctions, *Adv. Mater.*, **2009**, *21*, 4238–4242

27. D.H. Wang, K.H. Park, J.H. Seo, J. Seifter, J.H. Jeon, J.K. Kim, J.H. Park, O.O. Park, A.J. Heeger, Enhanced power conversion efficiency in PCDTBT/$PC_{70}BM$ bulk heterojunction photovoltaic devices with embedded silver nanoparticle clusters, *Adv. Energy Mater.*, **2011**, *1*, 766–770

28. Y. Sun, C.J. Takacs, S.R. Cowan, J.H. Seo, X. Gong, A. Roy, A.J. Heeger, Efficient, air-stable bulk heterojunction polymer solar cells using MoO_x as the anode interfacial layer, *Adv. Mater.*, **2011**, *23*, 2226-2230

29. R. Yang, R. Tian, J. Yan, Y. Zhang, J. Yang, Q. Hou, W. Yang, C. Zhang, Y. Cao, Deep-red electroluminescent polymers: synthesis and characterization of new low-band-gap conjugated copolymers for light-emitting diodes and photovoltaic devices, *Macromolecules*, **2005**, *38*, 244-253

30. W. Li, R. Qin, Y. Zhou, M. Andersson, F. Li, C. Zhang, B. Li, Z. Liu, Z. Bo, F. Zhang, Tailoring side chains of low band gap polymers for high efficiency polymer solar cells, *Polymer*, **2010**, *51*, 3031-3038
31. Z.-G. Zhang, J. Wang, Structures and properties of conjugated donor-acceptor copolymers for solar cell applications, *J. Mater. Chem.*, **2012**, *22*, 4178-4187
32. H. Yi, S. Al-Faifi, A. Iraqi, D.C. Watters, J. Kingsley, D.G. Lidzey, Carbazole and thienyl benzo[1,2,5]thiadiazole based polymers with improved open circuit voltages and processability for application in solar cells, *J. Mater. Chem.*, **2011**, *21*, 13649-13656

Chapter 7

A high performing fluorene-based polymer for OPV applications

In the previous two chapters it was shown that the basic building blocks of the polymer PCDTBT can be modified to optimise certain device properties, including solubility, absorption and charge-carrier mobility. In Chapter 5 we detailed the influence of the addition of solubilising sidegroups on the BT unit and how polymeric solubility can be greatly enhanced while maintaining high device performance. The inclusion of additional thiophene moieties along the polymer backbone was then shown to reduce the optical energy gap, consequently red-shifting the absorption, as well as increasing the hole mobility due to a greater degree of polymer planarity. Although the previous chapter primarily focused on the substitution of thiophene with selenophene (similarly found to reduce the optical energy gap), the carbazole based polymers were also compared with those containing a fluorene unit. It was generally found that the latter displayed superior performance due to an increase by up to 0.17 V in the open-circuit voltages of optimised devices. Polymers containing soluble sidegroups on the benzothiadiazole unit (BT-8) also displayed increased solubilities leading to higher molecular weights. Through the combination of such alterations, this chapter presents a novel fluorene-based polymer which contains a BT-8 unit as well as additional thiophenes (i.e. PFDT2BT-8) for photovoltaic applications.

7.1 – Introduction

As briefly discussed in Section 6.1, fluorene-based polymers display numerous attractive properties including good solubility and chemical and thermal stability [1-8]. When used in bulk heterojunction devices, V_{oc}

values exceeding 1 V can be realised [9-20]. However, despite these advantages, studies regarding such polymers have seen power conversion efficiencies restricted to ~ 4.5% [21]. In this case, the authors associated the low charge carrier mobility as the parameter needing further optimisation to improve device FF, which in previous studies was low despite a thin active layer thickness of 47 nm.

There have been several studies on the use of PFDTBT type polymers as a structure around which to create lower energy gap polymers. For example, the APFO family [22] modifies/replaces the BT unit and has resulted in a polymer with a reduced energy gap and a photoresponse up to 1,000 nm [23-24]. Performance, however, for APFO-Green1 was restricted by low device metrics, consequently preventing efficiencies greater than 1% being demonstrated. Other approaches used the inclusion of additional thiophenes along the polymer backbone for fluorene and benzothiadiazole containing polymers to reduce the optical energy gap [25-27]. Solubility issues arising from the lengthened backbone were addressed through the introduction of alkyl chains on the thiophene units rather than on the BT unit [25-26]. Efficiencies were however restricted to a maximum of 2.63% due to low FF values. The positioning of such side chains on the thiophene units was found to be important, not only to improve solubility, but also to control the molecular weight and the electronic properties of the resultant polymer [25,28].

In this chapter, a fluorene based polymer termed PFDT2BT-8 is characterised, having soluble side chains on the BT unit (chemical structure displayed in Figure 7.1a). This material is compared with its analogous carbazole cousin PCDT2BT-8 (as presented in Chapter 5, Figure 7.1b). Comparisons will also be made throughout with refs 25-27 that detail similar polymers having soluble side chains positioned on the thiophene units (Figure 7.1c) as well as PFDTBT-8 (from Chapter 6, without the additional thiophenes).

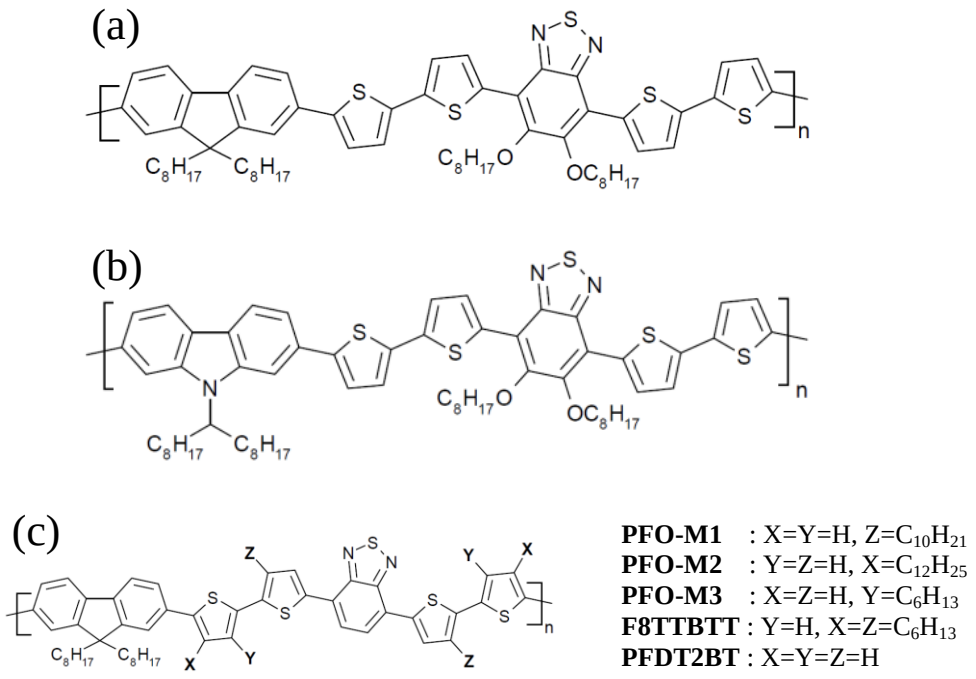

Figure 7.1 Chemical structure of polymers compared in this chapter. Part (a) displays the novel polymer PFDT2BT-8 explored here, while (b) shows its carbazole equivalent PCDT2BT-8. The polymers presented in refs 25-27 are displayed in part (c), note the absence of sidegroups on the BT unit.

7.2 – UV-Vis spectroscopy and energy level determination

Figure 7.2 displays the normalised absorption spectra of PFDT2BT-8 in a $CHCl_3$ solution as well as a thin film spun from $CHCl_3$ (pristine and blended with $PC_{70}BM$ at a blend ratio of 1:4). Although both systems display very similar peak values (summarised in Table 7.1), positioned at 420 and 540-550 nm, the thin film spectrum exhibits a greater degree of absorption beyond 550 nm. This could be due to a number of effects including an increased backbone planarity, enhanced intermolecular interactions, as well as additional inhomogeneous broadening; an effect that results from molecules adopting a non-equilibrium conformation.

Although the thin film maximum absorption peaks occur at approximately the same wavelength as PFDTBT-8 (~ 550 nm), the peak extends further resulting in an enhanced absorption above 550 nm. This broadening results in an absorption onset at 655 nm, resulting in an optical energy gap of ~ 1.89 eV (see Table 7.1). This indicates therefore that the inclusion of additional thiophene moieties has reduced the optical energy gap by ~ 0.09 eV (c.f. ~ 1.98 eV for PFDTBT-8, Table 7.1), which can be attributed to a combination of steric and electronic effects. The low wavelength peak also occurs at a longer wavelength upon thiophene inclusion (similarly seen in Section 5.2).

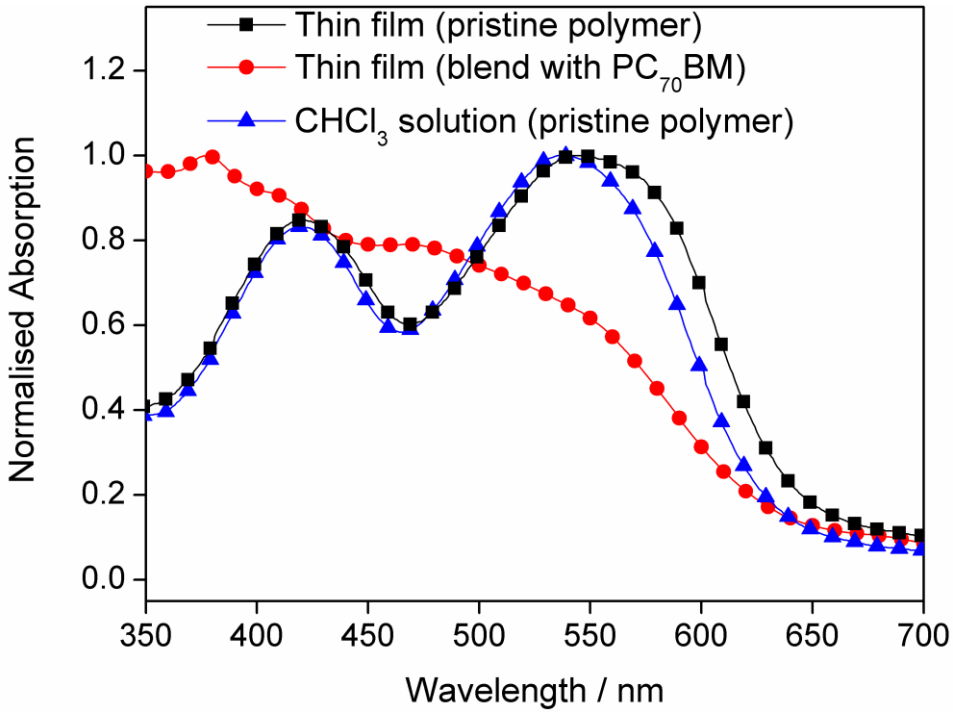

Figure 7.2 Absorption spectra of the polymer in a $CHCl_3$ solution and as a thin film (pristine polymer and blended with $PC_{70}BM$ at 1:4) spun from a $CHCl_3$ solution.

A comparison with polymers in which the soluble side chain exists on the thiophene units (as well as PFDT2BT which has no side groups) suggests that placing the side chains on the BT unit results in a larger optical energy gap. This result is consistent with the findings from the previous chapters. Note that the polymer F8TTBTT (where all four thiophenes have side chains at the 4'-position) displayed an even larger E_g^{op}. Clearly the positioning of soluble side chains has an affect on the optical properties as well as the polymeric solubility.

Polymer	λ_{max} / nm Thin film ($CHCl_3$ Solution)	E_g^{op} / eV	M_w / kDa	HOMO / eV	LUMO / eV
PFDT2BT-8	420 (420) / 550 (540)	1.89	91.6	-5.33	-3.34
PFDTBT-8	392 (388) / 544 (518)	1.98	468.7	-5.44	-3.32
PCDT2BT-8	421 (420) / 548 (542)	1.93	57.2	-5.20	-3.29
PFO-M1[a)]	402 / 571	1.79	171.2	-5.40	-3.13
PFO-M2[a)]	417 / 565	1.81	13.5	-5.37	-3.17
PFO-M3[a)]	428 / 589	1.77	142.6	-5.34	-3.22
F8TTBTT[b)]	405 (390) / 560 (550)	2.07	63.7	-5.45	-3.38
PFDT2BT[c)]	422 (412) / 547 (518)	1.83	36.0	-5.43	-3.60

Table 7.1 UV-Vis, GPC and energy levels of PFDT2BT-8 compared with its carbazole equivalent and PFDTBT-8 (without the additional thiophenes). Data provided by Hunan Yi from the Chemistry department. [a)] taken from ref 25 (no solution absorption provided), [b)] from ref 26 (values are approximate), [c)] from ref 27.

The measured M_w of PFDT2BT-8 (also displayed in Table 7.1) is relatively high at 91.6 kDa, suggesting good solubility. A similarly high M_w value was also seen from PFDTBT-8 in Chapter 6, implying that the introduction of octyloxy substituents leads to an enhanced solubility for fluorene based polymers (M_w was restricted to < 10.0 kDa without such side groups). Interestingly, PFDT2BT (which has additional thiophene moieties but no soluble side chains) displayed a M_w value of 36.0 kDa [27]. Although this polymer did not include any sidegroups (apart from those on the fluorene unit), its M_w was larger than their presented PFDTBT which, similar to the version discussed in Chapter 6, was restricted to 7.0-8.0 kDa. This suggests

that extending the polymer backbone with additional thiophene moieties appears to enhance the polymer solubility (as well as increase the molecular weight) even without the presence of soluble side chains. This result is surprising and is in contrast to the results presented for the carbazole equivalent discussed in Section 5.4, in which we concluded the lack of sidegroups would result in a polymer with poor solubility. Sidegroups located on the thiophene units led to polymers (PFO polymers) having very high molecular weights (M_w > 100 kDa), although the positioning of side-chains was found to be crucial [25]. For example, placing the side chain on the 4'-position of the thiophene adjacent to the fluorene unit (PFO-M2) prevented such a large improvement (~ 13.0 kDa) due to steric hindrance effects.

The HOMO and LUMO energy levels (as determined from CV measurements) are shown in Table 7.1. Similar to the results presented in Chapter 5, the HOMO energy level for the polymer with additional thiophene moieties (-5.33 eV) is slightly smaller (closer to vacuum level); an observation attributed to the fact that the thiophene units enhance the electron accepting capabilities of the polymer. It is however worth noting that this value remains below the air oxidation threshold at approx. -5.27 eV [29], implying high stability of the fluorene unit, whereas the carbazole equivalent exhibited a HOMO energy level at -5.20 eV. The LUMO energy level is consistent with PFDTBT-8 (~ 0.02 eV difference); a result similarly observed in the carbazole polymers in Chapter 5.

7.3 – Device optimisation

Optimisation protocols were initially based on that used for PCDT2BT-8 (see Section 5.5) since their structure and energy levels are similar. However, with the presence of fluorene and its higher solubility it was thought that the polymer could be successfully processed from DCB and CB solutions (results shown in Table 7.2, J-V characteristic from devices with max PCE displayed in Figure 7.3). The PCEs of such devices tend to be around 5%, with DCB processed devices having superior FFs, although such values were still quite low (this appears to be a trend for fluorene based polymers, see Table 6.3). The use of a solvent additive (diiodooctane – DIO) has been shown to improve the efficiency of devices based on the materials PBDTTT-C-T [30-31], PTB7 [32-34] and PDTG-TPD [35-36], primarily through the J_{sc} and FF. It is believed that DIO solubilises $PC_{70}BM$ [37] as well as increasing the thin film drying time (due to its higher boiling point temperature). DIO was thus used in a CB solution (at 1 and 3% vol) to improve device performance. As evident from Table 7.2 and Figure 7.3, the FF was indeed improved as a result of the use of DIO, however, the J_{sc} was dramatically reduced resulting in maximum efficiencies of ~ 3%. We speculate that this was due to non-ideal phase separation leading to reduced exciton dissociation. However, we were not able to test this due to DIO remaining within the thin film. This caused the film to have a "wet" surface, meaning it was not possible to use AFM to image the film.

Solvent	Blend Ratio	Thickness / nm	J_{sc} / $mAcm^{-2}$	V_{oc} / V	FF / %	PCE / %
DCB	1:4	75	-10.48	0.90	54.10	5.12*
CB	1:4	75	-10.55	0.89	50.17	4.72*
CB+1%DIO	1:4	60	-4.70	0.95	69.12	3.10*
CB+3%DIO	1:4	60	-4.74	0.97	68.18	3.12*
$CHCl_3$	1:2	90	-9.17	0.91	52.19	4.35
	1:3	75	-9.95	0.90	56.89	5.08
	1:4	60	-10.44	0.92	64.50	6.20^{+}
[a]	1:4	90	-9.82	0.91	65.12	5.84^{+}
[a],[b]	1:4	80	-9.21	0.93	55.97	4.79
	1:5	60	-9.82	0.91	59.69	5.36

Table 7.2 Optimised device metrics from various casting solvents and blend ratios. Device architecture was ITO/PEDOT:PSS/PFDT2BT-8:$PC_{70}BM$/ Ca/Al. [a] Thermally evaporated MoO_x anode buffer layer replaced PEDOT:PSS. [b] Thermally annealed post-cathode deposition at 80°C. J-V characteristics of devices marked with * are shown in Figure 7.3, and with $^{+}$ shown in Figure 7.4.

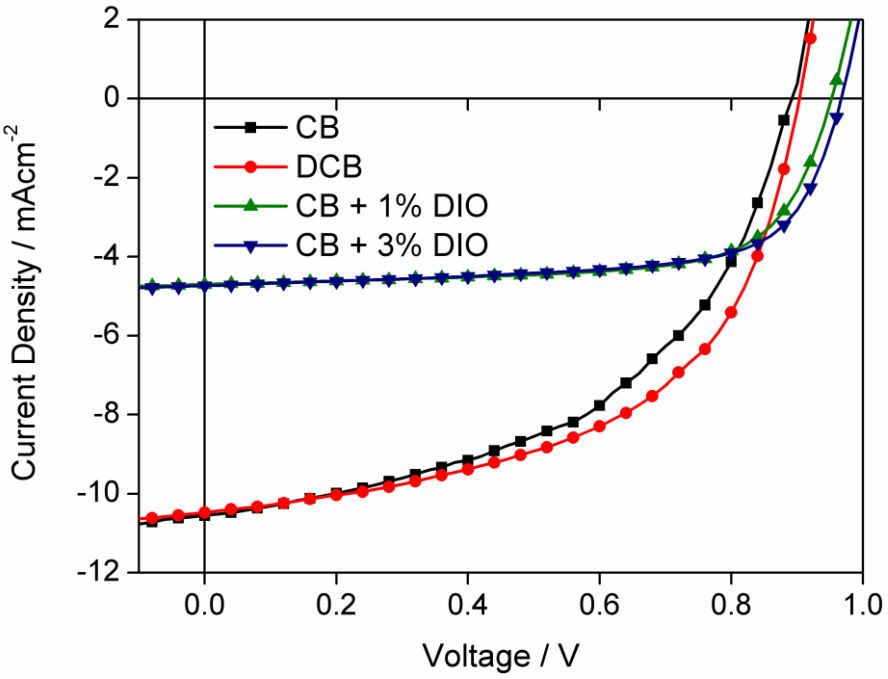

Figure 7.3 J-V characteristics of devices cast from CB, DCB and CB with a DIO solvent additive (1 and 3% volume). PEDOT:PSS anode buffer layer and a Ca/Al cathode was used for all. Device metrics provided in Table 7.2.

Decreasing the thin film drying time by using a low boiling point solvent ($CHCl_3$) resulted in enhanced device efficiencies. Although the J_{sc} remained similar to those achieved using both CB and DCB casting solvents, the V_{oc} and FF values increased. A maximum PCE of 6.2% was realised upon optimisation of the blend ratio and active layer thickness (the J-V characteristic is displayed in Figure 7.4). Significantly, this high performance was achieved with no need for any post-deposition treatment (solvent or thermal annealing) or a solvent additive which have been a necessity for other polymers with similar energy gaps. This result is promising for potential large-scale production due to the ease of solution and film preparation. It is also the highest performing fluorene based polymer for OPV applications.

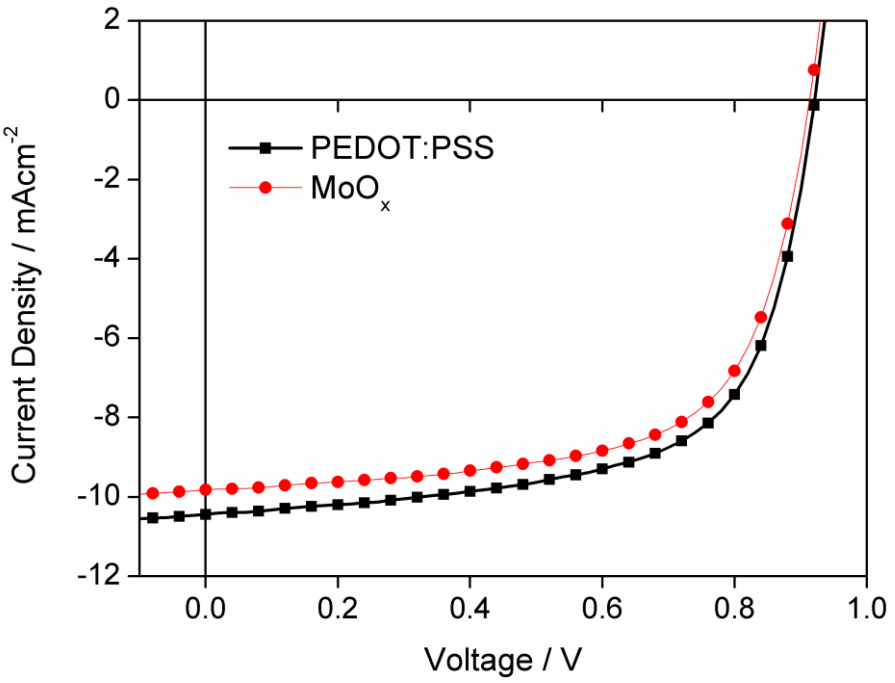

Figure 7.4 J-V characteristics of optimised devices spincast from $CHCl_3$ utilising either a PEDOT:PSS or MoO_x anode buffer layer.

With the HOMO energy level having a value comparable with PCDTBT (-5.33 eV and -5.35 eV respectively), replacing the PEDOT:PSS with MoO_x was expected to result in an enhanced ohmic contact leading to improved V_{oc} and FF values (as seen in Section 4.2). However, despite a marginal increase in the FF, a small reduction in the J_{sc} resulted in a maximum PCE of 5.8% (see Figure 7.4 and Table 7.2). This reduction in J_{sc} is thought to be due to a reduced electric field distribution within the device, as confirmed from the transfer matrix model. Here, the active layer thickness was varied while the cathode composition was kept constant (a bi-layer consisting of a 5 nm Ca layer backed by 200 nm Al) for a 10 nm thick MoO_x and a 20 nm PEDOT:PSS layer. Upon comparing the modelled photocurrent for devices based on PEDOT:PSS and MoO_x (Figure 7.5), the J_{max} is predicted to be -10.66 and -10.37 $mAcm^{-2}$ respectively for the thin film peak (< 100 nm). It

can be seen that the modelled J_{max} for a MoO_x anode buffer layer is higher than that of PEDOT:PSS based devices at large (> 95 nm) active layer thicknesses. This was actually observed from the optimised device active layers presented in Table 7.2. Here, a max PCE was determined at an active layer thickness of 90 nm using a MoO_x buffer layer, whereas optimal efficiency using PEDOT:PSS occurred at a lower active layer thickness of 60 nm.

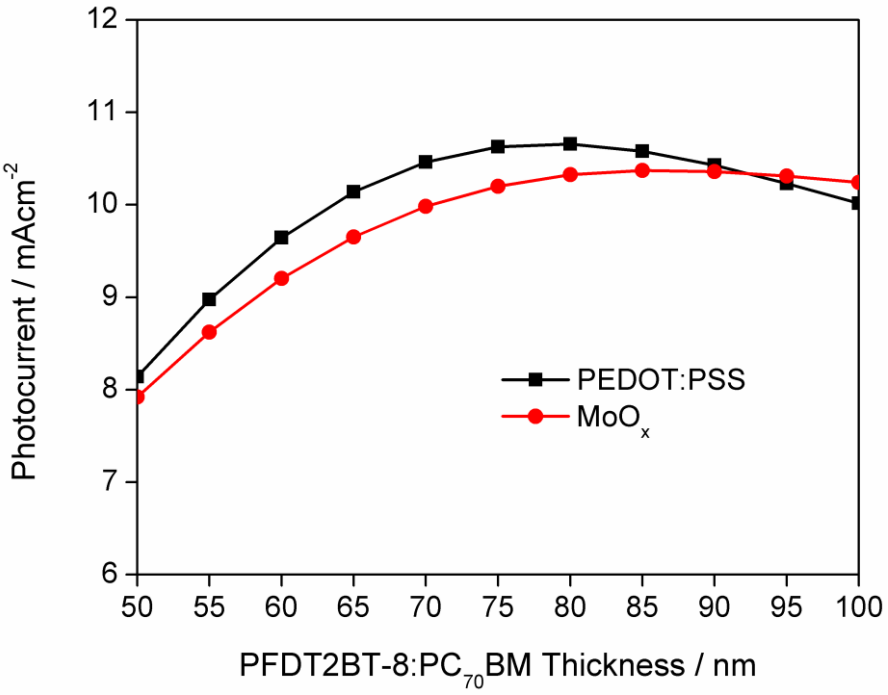

Figure 7.5 Modelled photocurrent at the thin film interference peak for PEDOT:PSS and MoO_x anode buffer layers.

To explore the nature of phase separation in devices spun from $CHCl_3$, topological and phase images were recorded using an AFM (see Section 3.6) and are displayed in Figure 7.6. Both of these images indicate good evidence for a thin film which may perform well in devices; it can be seen

that the thin film is smooth having a root-mean square (RMS) roughness of ~ 1 nm. The phase image also shows a phase-separation below the resolution of the microscope, indicating that the fullerene and PFDT2BT-8 are very finely mixed.

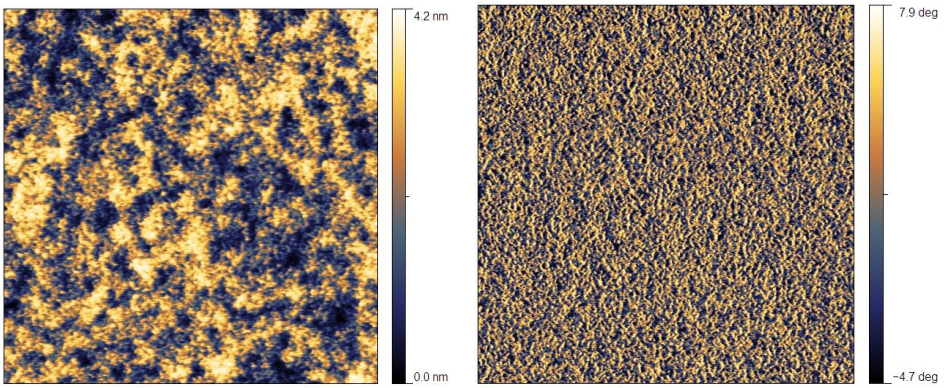

Figure 7.6 Topological and phase image (1 μm x 1 μm) of PFDT2BT-8:$PC_{70}BM$ at 1:4 spun onto a glass substrate from a $CHCl_3$ solution.

7.4 – OFET mobility

Using an OFET device architecture, the hole mobility of PFDT2BT-8 is shown in Table 7.3 and Figure 7.7. Note that the values for PFDTBT-8 (taken from Table 6.4) and PCDT2BT-8 (from Section 5.5.1) as well as F8TTBTT (sidegroups on all thiophenes) and PFDT2BT (additional thiophenes without any side chains) are also presented for the sake of comparison. It can be seen that the additional thiophenes again lead to an enhanced hole mobility for the fluorene unit (~ 5 x 10^{-3} $cm^2V^{-1}s^{-1}$) which may be due to improved planarization of the polymer backbone and/or stronger intermolecular interactions. The improved fill factors observed in

devices are likely to be directly related to such improvements in hole mobility.

Polymer	μ / $cm^2V^{-1}s^{-1}$
PFDT2BT-8	5.06×10^{-3}
PFDTBT-8	4.63×10^{-4}
PCDT2BT-8	2.68×10^{-3}
F8TTBTT	2.5×10^{-2}
PFDT2BT	2.7×10^{-6}

Table 7.3 OFET hole mobilities for the polymer PFDT2BT-8 along with its carbazole equivalent PCDT2BT-8 and PFDTBT-8 (without the additional thiophenes) as well as F8TTBTT and PFDT2BT (taken from refs 26 and 27 respectively).

Note that mobility measurements taken for PFDT2BT indicated low values of 2.7×10^{-6} $cm^2V^{-1}s^{-1}$ [27]. The inclusion of sidegroups on all thiophenes (i.e. F8TTBTT) provided high charge mobility values of 2.5×10^{-2} $cm^2V^{-1}s^{-1}$. Coupled with the differences observed from device efficiency, the introduction of sidegroups (as well as their positioning) can have an important impact on polymer solubility, mobility and bulk heterojunction functionality.

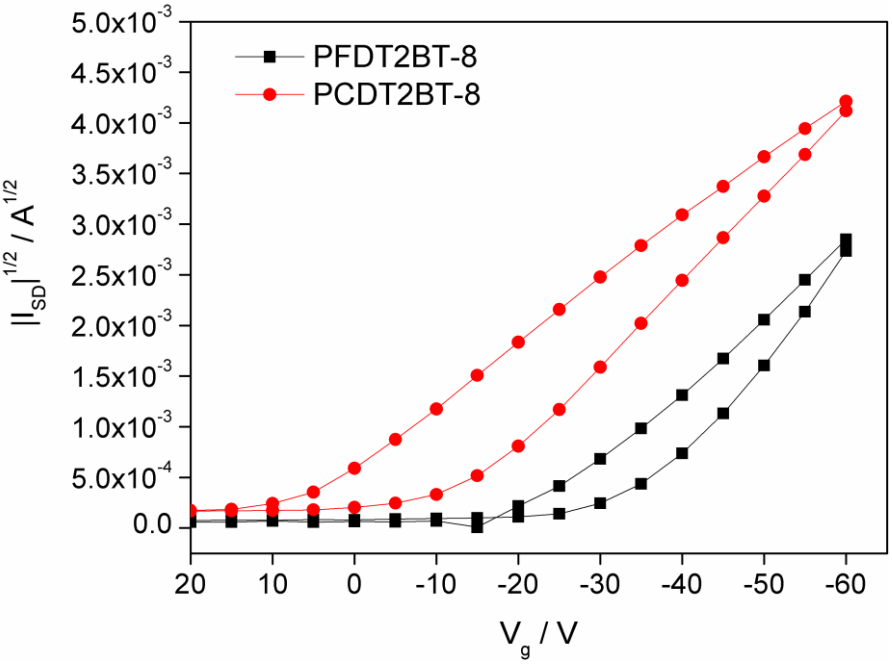

Figure 7.7 Saturated transfer characteristics of PFDT2BT-8 and PCDT2BT-8. Hole mobility measurements taken from the average of the up and down sweeps.

7.5 – Conclusion

A novel fluorene based polymer has been presented and characterised in organic photovoltaic devices and organic field effect transistors. It was shown that inclusion of additional thiophene moieties act to reduce the optical energy gap as well as increasing hole mobility. Device studies demonstrated that optimal efficiency was realised using a fast drying solvent (e.g. $CHCl_3$) without the requirement of any solvent additives or any thermal/solvent annealing treatments. Results obtained from AFM imaging showed polymer:fullerene blends were characterised by a smooth film with little or no phase separation visible, suggesting a very finely structured active layer leading to efficient photocurrent generation. The observed high PCEs and simple production procedure (fast drying casting solvent and no

post-deposition treatment) highlight the potential use of this polymer for practical device application.

References

1. Q. Pei, Y. Yang, Efficient photoluminescence and electroluminescence from a soluble polyfluorene, *J. Am. Chem. Soc.*, **1996**, *118*, 7416
2. G. Klärner, J.-I. Lee, M.H. Davey, R.D. Miller, Exciton migration and trapping in copolymers based on dialkylfluorenes, *Adv. Mater.*, **1999**, *11*, 115-119
3. M. Bernius, M. Inbasekaran, J. O'Brien, W. Wu, Progress with light-emitting polymers, *Adv. Mater.*, **2000**, *12*, 1737-1750
4. S. Setayesh, A.C. Grimsdale, T. Weil, V. Enkelmann, K. Müllen, F. Meghdadi, E.J.W. List, G. Leising, Polyfluorenes with polyphenylene dendron side chains: toward non-aggregating, light-emitting polymers, *J. Am. Chem. Soc.*, **2001**, *123*, 946-953
5. Q. Hou, Y. Xu, W. Yang, M. Yuan, J. Peng, Y. Cao, Novel red-emitting fluorene-based copolymers, *J. Mater. Chem.*, **2002**, *12*, 2887-2892
6. M. Bernius, M. Inbasekaran, E. Woo, W.S. Wu, L. Wujokwski, Fluorene-based polymers-preparation and applications, *J. Mater. Sci: Mater. Electron.*, **2002**, *11*, 111-116
7. W.-Y. Wong, Metallated molecular materials of fluorene derivatives and their analogues, *Coordin. Chem. Rev.*, **2005**, *9-10*, 971-997
8. H. Wang, J. Gao, W. Tong, Q. Qian, K. Lin, F. Liu, Copolymerization of 3,3'''-didodecylquaterthiophene with fluorene and silole units:

improving photovoltaic performance by tuning energy levels, *Polym. Chem.*, **2012**, *3*, 2794-2800

9. M. Svensson, F. Zhang, S.C. Veenstra, W.J.H. Verhees, J.C. Hummelen, J.M. Kroon, O. Inganäs, M.R. Andersson, High-performance polymer solar cells of an alternating polyfluorene copolymer and a fullerene derivative, *Adv. Mater.*, **2003**, *15*, 988-991
10. T. Yohannes, F. Zhang, M. Svensson, J.C. Hummelen, M.R. Andersson, O. Inganäs, Polyfluorene copolymer based bulk heterojunction solar cells, *Thin Solid Films*, **2004**, *449*, 152-157
11. O. Inganäs, M. Svensson, F. Zhang, A. Gadisa, N.K. Persson, X. Wang, M.R. Andersson, Low bandgap alternating polyfluorene copolymers in plastic photodiodes and solar cells, *Appl. Phys. A*, **2004**, *79*, 31-35
12. R. Yang, R. Tian, J. Yan, Y. Zhang, J. Yang, Q. Hou, W. Yang, C. Zhang, Y. Cao, Deep-red electroluminescent polymers: synthesis and characterization of new low-band-gap conjugated copolymers for light-emitting diodes and photovoltaic devices, *Macromolecules*, **2005**, *38*, 244-253
13. F. Zhang, K.G. Jespersen, C. Björström, M. Svensson, M.R. Andersson, V. Sundström, K. Magnusson, E. Moons, A. Yartsev, O. Inganäs, Influence of solvent mixing on the morphology and performance of solar cells based on polyfluorene copolymer/fullerene blends, *Adv. Funct. Mater.*, **2006**, *16*, 667-674
14. L.H. Slooff, S.C. Veenstra, J.M. Kroon, D.J.D. Moet, J. Sweelssen, M.M. Koetse, Determining the internal quantum efficiency of highly

efficient polymer solar cells through optical modeling, *Appl. Phys. Lett.*, **2007**, *90*, 143506

15. G.L. Schulz, X. Chen, S. Holdcroft, High band gap poly(9,9-dihexylfluorene-alt-bithiophene) blended with [6,6]-phenyl C_{61} butyric acid methyl ester for use in efficient photovoltaic devices, *Appl. Phys. Lett.*, **2009**, *94*, 023302-023304
16. K. Vandewal, K. Tvingstedt, A. Gadisa, O. Inganäs, J.V. Manca, On the origin of the open-circuit voltage of polymer–fullerene solar cells, *Nat. Mater.*, **2009**, *8*, 904-909
17. X. Chen, G.L. Schulz, X. Han, Z. Zhou, S. Holdcroft, Polymer solar cells based on alternating and statistical 4,7-bis(4-octylphenyl-2-thienyl)-2,1,3-benzothiadiazole copolymers, *J. Phys. Chem. C*, **2009**, *113*, 8505-8512
18. W. Li, R. Qin, Y. Zhou, M. Andersson, F. Li, C. Zhang, B. Li, Z. Liu, Z. Bo, F. Zhang, Tailoring side chains of low band gap polymers for high efficiency polymer solar cells, *Polymer*, **2010**, *51*, 3031-3038
19. D. Di Nuzzo, G.-J.A.H. Wetzelaer, R.K.M. Bouwer, V.S. Gevaerts, S.C.J. Meskers, J.C. Hummelen, P.W.M. Blom, R.A.J. Janssen, Simultaneous open-circuit voltage enhancement and short-circuit current loss in polymer:fullerene solar cells correlated by reduced quantum efficiency for photoinduced electron transfer, *Adv. Energy Mater.*, **2013**, *3*, 85-94
20. A.A.B. Alghamdi, D.C. Watters, H. Yi, S. Al-Faifi, M.S. Almeataq, D. Coles, J. Kingsley, D.G. Lidzey, A. Iraqi, Selenophene *vs.* thiophene in

benzothiadiazole-based low energy gap donor acceptor polymers for photovoltaic applications, *J. Mater Chem. A*, **2013**, *1*, 5165-5171

21. M.-H. Chen, J. Hou, Z. Hong, G. Yang, S. Sista, L.-M. Chen, Y. Yang, Efficient polymer solar cells with thin active layers based on alternating polyfluorene copolymer/fullerene bulk heterojunctions, *Adv. Mater.*, **2009**, *21*, 4238-4242
22. S. Admassiea, O. Inganäs, W. Mammo, E. Perzon, M.R. Andersson, Electrochemical and optical studies of the band gaps of alternating polyfluorene copolymers, *Synthetic Met.*, **2006**, *156*, 614-623
23. X. Wang, E. Perzon, J.L. Delgado, P. de la Cruz, F. Zhang, F. Langa, M. Andersson, O. Inganäs, Infrared photocurrent spectral response from plastic solar cell with low-band-gap polyfluorene and fullerene derivative, *Appl. Phys. Lett.*, **2004**, *85*, 5081-5083
24. X. Wang, E. Perzon, F. Oswald, F. Langa, S. Admassie, M.R. Andersson, O. Inganäs, Enhanced photocurrent spectral response in low-bandgap polyfluorene and C_{70}-derivative-based solar cells, *Adv. Funct. Mater.*, **2005**, *15*, 1665-1670
25. E. Wang, M. Wang, L. Wang, C. Duan, J. Zhang, W. Cai, C. He, H. Wu, Y. Cao, Donor polymers containing benzothiadiazole and four thiophene rings in their repeating units with improved photovoltaic performance, *Macromolecules*, **2009**, *42*, 4410-4415
26. Z. Chen, Junfeng Fang, F. Gao, T.J.K. Brenner, K.K. Banger, X. Wang, W.T.S. Huck, H. Sirringhaus, Enhanced charge transport by incorporating additional thiophene units in the poly(fluorene-thienyl-benzothiadiazole) polymer, *Org. Electron.*, **2011**, *12*, 461-471

27. J.-H. Kim, H.U. Kim, D. Mi, S.-H. Jin, W.S. Shin, S.C. Yoon, I.-N. Kang, D.-H. Hwang, Introduction of perylene units for enhanced interchain interaction in conjugated polymers for organic photovoltaic devices, *Macromolecules*, **2012**, *45*, 2367-2376
28. L. Biniek, S. Fall, C.L. Chochos, D.V. Anokhin, D.A. Ivanov, N. Leclerc, P. Lévêque, T. Heiser, Impact of the alkyl side chains on the optoelectronic properties of a series of photovoltaic low-band-gap copolymers, *Macromolecules*, **2010**, *43*, 9779-9786
29. D.M. de Leeuw, M.M.J. Simenon, A.R. Brown, R.E.F. Einerhand, Stability of n-type doped conducting polymers and consequences for polymeric microelectronic devices, *Synthetic Met.*, **1997**, *87*, 53-59
30. L. Huo, S. Zhang, X. Guo, F. Xu, Y. Li, J. Hou, Replacing alkoxy groups with alkylthienyl groups: a feasible approach to improve the properties of photovoltaic polymers, *Angew. Chem. Int. Ed.*, **2011**, *50*, 9697-9702
31. X. Li, W.C.H. Choy, L. Hou, F. Xie, W.E.I. Sha, B. Ding, X. Guo, Y. Li, J. Hou, J. You, Y. Yang, Dual plasmonic nanostructures for high performance inverted organic solar cells, *Adv. Mater.*, **2012**, *24*, 3046-3052
32. Y. Liang, Z. Xu, J. Xia, S.-T. Tsai, Y. Wu, G. Li, C. Ray, L. Yu, For the bright future – bulk heterojunction polymer solar cells with power conversion efficiency of 7.4%, *Adv. Energy Mater.*, **2010**, *22*, E135-E138
33. Z. He, C. Zhong, X. Huang, W.-Y. Wong, H. Wu, L. Chen, S. Su, Y. Cao, Simultaneous enhancement of open-circuit voltage, short-circuit

current density, and fill factor in polymer solar cells, *Adv. Mater.*, **2011**, *23*, 4636-4643

34. Z. He, C. Zhong, S. Su, M. Xu, H. Wu, Y. Cao, Enhanced power-conversion efficiency in polymer solar cells using an inverted device structure, *Nature Photon.*, **2012**, *6*, 591-595
35. C.M. Amb, S. Chen, K.R. Graham, J. Subbiah, C.E. Small, F. So, J.R. Reynolds, Dithienogermole as a fused electron donor in bulk heterojunction solar cells, *J. Am. Chem. Soc.*, **2011**, *133*, 10062-10065
36. S. Chen, C.E. Small, C.M. Amb, J. Subbiah, T.-H. Lai, S.-W. Tsang, J.R. Manders, J.R. Reynolds, F. So, Inverted polymer solar cells with reduced interface recombination, *Adv. Energy Mater.*, **2012**, *2*, 1333-1337
37. S.J. Lou, J.M. Szarko, T. Xu, L. Yu, T.J. Marks, L.X. Chen, Effects of additives on the morphology of solution phase aggregates formed by active layer components of high-efficiency organic solar cells, *J. Am. Chem. Soc.*, **2011**, *133*, 20661-20663

Chapter 8

Conclusions

I have described the characterisation of a number of polymer derivatives of the copolymer PCDTBT and their application as the active medium in organic solar cells. This has involved a detailed device optimisation programme, with techniques used including varying the casting solvent, blend ratio (with the fullerene $PC_{70}BM$), and altering the active layer thickness.

In Chapter 4, the effects of different anode buffer layers and cathode structures on the maximum device performance for a PCDTBT:$PC_{70}BM$ OPV was explored. The use of the metal oxides MoO_x and V_2O_5 as the anode buffer layer demonstrated enhanced device efficiency compared with those utilising PEDOT:PSS and were used to create devices having promising storage stability over a 2 month period. By using a transfer matrix reflectivity model, the maximum photocurrent that could be generated from an optimised OPV was modelled for a variety of cathode materials, including composite structures in which a thin film of calcium was backed with an optically thick layer of aluminium or silver. It was found that device photocurrent was dependent on the reflectivity of the cathode with a calcium cathode resulting in a relatively low photocurrent due to increased optical losses. Composite structures were thus explored that combined high reflectivity with efficient charge extraction. It was found that OPV devices utilising a Ca/Al composite cathode resulted in high power conversion efficiencies through efficient optical harvesting and charge extraction as well as marginally improved open circuit voltages. This efficient cathode structure was consequently adopted for the remainder of the research.

Chapter 5 presented two polymers based on PCDTBT with soluble octyloxy substituents on the benzothiadiazole BT unit. The octyloxy sidegroups caused the optical energy gap to increase and therefore reduce the electronic delocalisation. This is due to the sidegroups reducing the electron accepting capabilities of the BT unit. The inclusion of additional spacer moieties along the polymer backbone caused a red-shift in the absorption, i.e. reducing the optical energy gap. It was also observed that the octyloxy sidegroups increased polymer solubility and suppressed aggregation. Bulk heterojunction devices based on the two soluble carbazole copolymers were found to have high performance in photovoltaic devices. Device optimisation studies indicated that a limited thermal annealing treatment was required to maximise power conversion efficiency, with the annealing temperature coinciding with the measured glass transition temperatures of pristine polymer thin films. Hole mobilities determined from organic field effect transistors (OFET) were maximised in a polymer containing additional thiophene moieties; an affect ascribed to a greater degree of backbone rigidity. The use of octyloxy sidegroups was further explored in the later chapters.

To improve the polymer spectral overlap, a study was performed on the use of selenium atoms (rather than sulphur) along the polymer backbone. This was described in Chapter 6, where derivatives of PCDTBT were again used with a comparison between carbazole and fluorene units, thiophene and selenophene moieties, as well as those with and without soluble octyloxy substituents. The absorption characteristics of the selenophene based

polymers were observed to be red-shifted relative to their thiophene analogues leading to a smaller optical energy gap. The HOMO energy level of the selenophene polymers also relatively increased; a result likely to be due to their differing electronegativity and electron donating capabilities. Bulk heterojunction solar cells fabricated with selenophene based polymers were however less efficient than those of the thiophene analogues. This was primarily due to decreased short circuit current J_{sc} values attributed to lower molar absorption coefficients. Lower hole mobilities, as determined from OFET devices, necessitated the use of thinner active layers for selenophene polymers to maximise charge extraction efficiency, consequently restricting their light harvesting capabilities. Furthermore, results from photoluminescence quantum yield measurements suggested the potential presence of triplet states in selenophene based polymers which it was speculated could deplete the singlet-exciton population. The potential existence of a triplet population was also inferred from a photostability study in which selenophene based polymers underwent more rapid degradation. Despite these poor qualities, one selenophene polymer was shown capable of producing highly efficient devices comparable with its thiophene analogue. It was also demonstrated that efficient devices were could be created from fluorene based polymers due to enhanced V_{oc} values, however polymers containing octyloxy substituents had lower FF values; a result in agreement with work presented in Chapter 5. The combination of an efficient fluorene unit, additional thiophene moieties for efficient charge mobility and soluble octyloxy substituents are used in the following chapter.

Chapter 7 presented a characterisation and OPV optimisation study of a novel fluorene based polymer. This polymer included additional thiophene moieties along the backbone which again served to red-shift its absorption characteristics. It was observed that the polymer also had a high hole mobility that was again ascribed to its greater molecular backbone rigidity. Device optimisation indicated that a fast drying solvent was necessary to achieve optimal photovoltaic efficiency. A key observation was that these high efficiencies were achieved without the use of a solvent additive or any thermal/solvent annealing treatments, thus highlighting the potential use of this polymer for practical device applications.

8.1 – Suggestions for further work

It is hoped that the work presented in this thesis has provided insight into a series of new donor polymers for OPV applications. However, additional work is required to fully understand some of the basic mechanisms that contribute to operational efficiency. In Chapter 6, the presence of triplet states was inferred from photoluminescence quantum yield measurements and photostability studies. Performing photoinduced absorption on the selenophene and thiophene based polymers should provide a greater insight into such underlying mechanisms. A comprehensive photostability study on selenophene based polymers, both for pristine and polymer:fullerene devices, should also be performed to provide an understanding of mechanisms that contribute to device stability in such polymer systems. Furthermore, a more detailed optimisation procedure could be devised for these selenophene based polymers to investigate the effects of thermal

annealing as well as solvent additives. The fluorene polymer presented in Chapter 7 achieved high device performance without the need for any annealing treatment or the addition of a solvent additive. Examination of device stability together with processing this polymer in air will also further test whether this polymer system is potentially suitable for commercial application. Finally, a number of different device architectures could also be explored using the polymers explored here (namely inverted and tandem devices) to see whether further increases in efficiency and stability can be gained.

Appendix

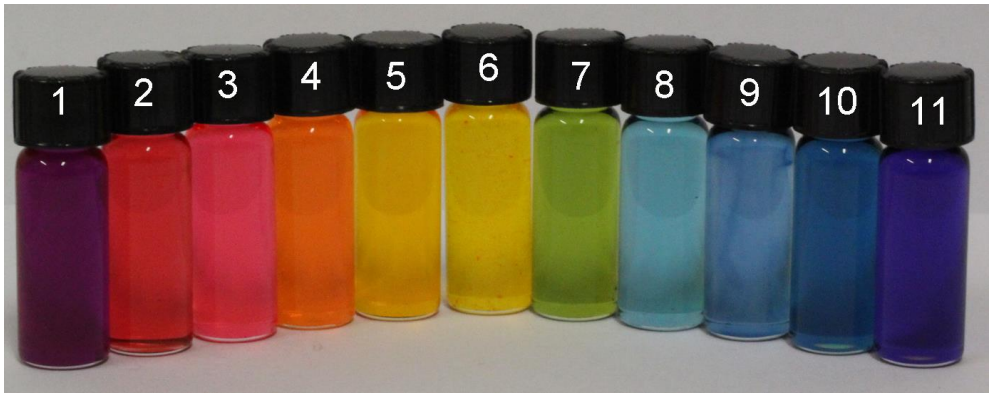

Figure A1 Optical image of different polymer solutions having differing absorption characteristics. Chemical structure and name of each polymer is presented below.

Solution 1: PCDTBT

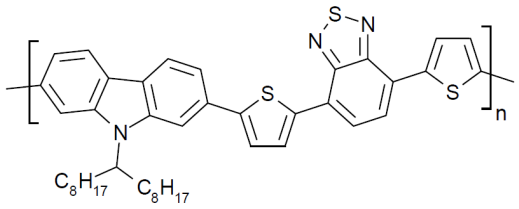

Solution 2: PCDT2BT-8

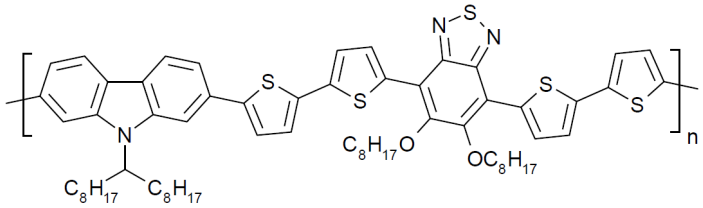

Solution 3: PCDTBT-8

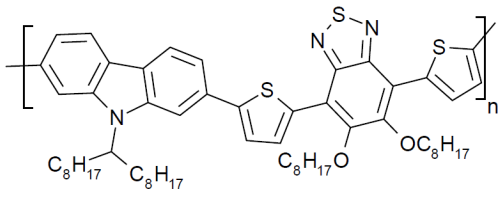

Solution 4: MEH-PPV (from Sigma Aldrich)

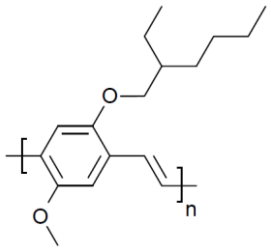

Solution 5: P3HT (from Ossila Ltd.)

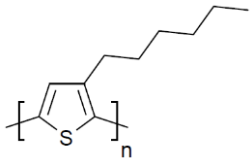

Solution 6: PCFDT

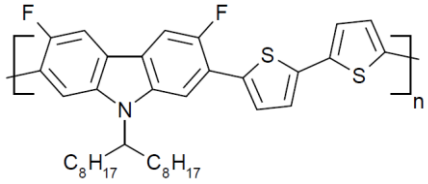

Solution 7: PCFDT-PCFDTTPZ (random)

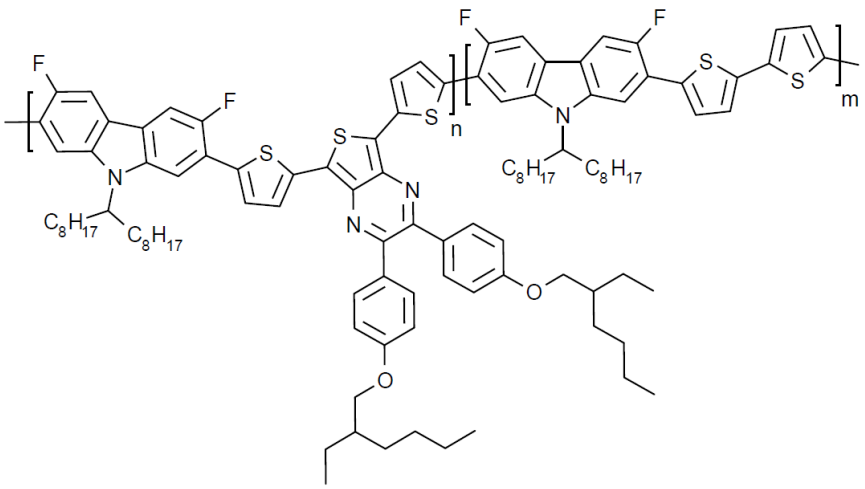

Solution 8: PCPDTBT (from 1-Material)

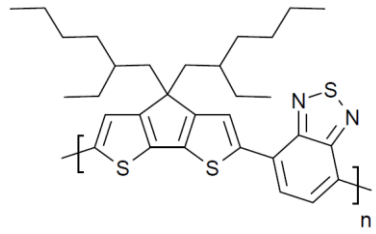

Solution 9: PTB7 (from 1-Material)

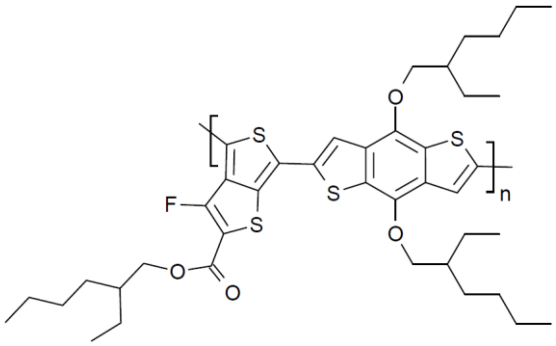

Solution 10: P(NDI2OD-T2) (from Polyera)

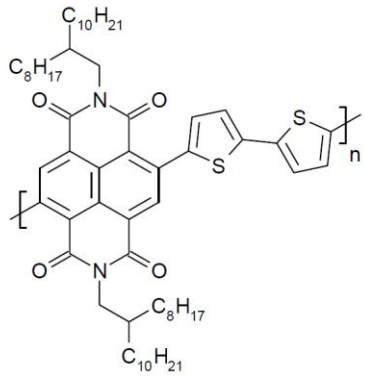

Solution 11: PDTBTBT-8